

國立交通大學

物理研究所

博士論文

高能微中子偵測與味物理學

High Energy Neutrino Detection and Neutrino Flavor  
Physics

研究生：劉宗哲

指導教授：林貴林 教授

黃明輝 教授

中華民國九十九年七月

# 高能微中子偵測與味物理學

## High Energy Neutrino Detection and Neutrino Flavor Physics

研 究 生：劉宗哲

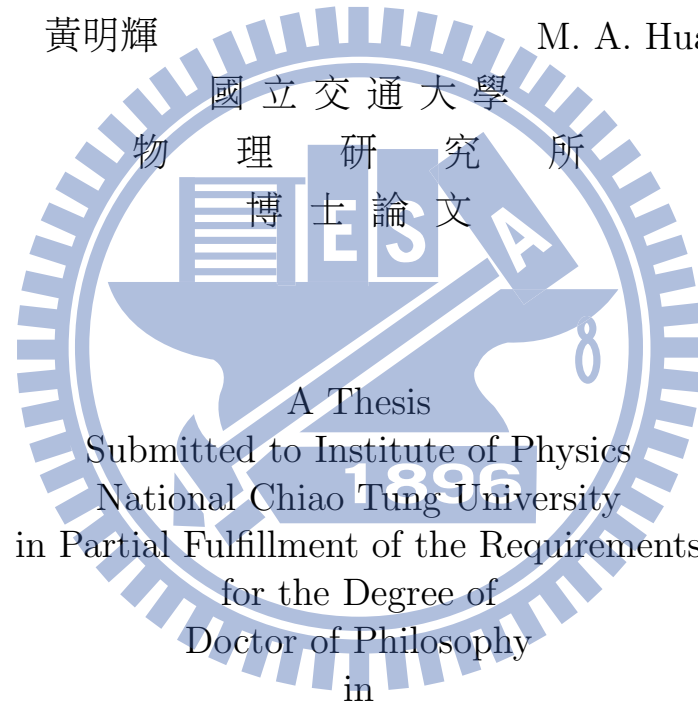
Student: Tsung-Che Liu

指 導 教 授：林貴林

Advisors: Guey-Lin Lin

黃明輝

M. A. Huang



A Thesis  
Submitted to Institute of Physics  
National Chiao Tung University  
in Partial Fulfillment of the Requirements  
for the Degree of  
Doctor of Philosophy  
in

Physics

July, 2010

Hsinchu, Taiwan

中華民國九十九年七月

# 高能微中子偵測與味物理學

學生：劉宗哲

指導教授：林貴林  
黃明輝

國立交通大學物理研究所

## 摘 要

本篇論文討論微中子由微中子源傳播至地球間的各種現象。在本文的第一部份,我們利用對微中子震盪角度的了解,重建微中子在不同量測條件下時於源頭的比例。我們發現區分不同的微中子源需要大量的觀測數據。另外本文也考慮當微中子衰變與震盪同時作用時,地球上的微中子比率的對應影響。由此我們給定了在99.7%信心水準下,不同衰變機制作用下,微中子比率在地球上的允許與禁制範圍。在本文的第二部份,我們介紹如何運用蒙地卡羅方法模擬微中子與地球各種交互作用。依照模擬我們可得到在偵測區域(DSR)內的輕子流量。由於濤輕子(Tau lepton)簇射後會產生大量正負電子對並受地磁偏轉而產生同步輻射。藉此我們計算不同能量下濤輕子簇射所對應的同步輻射訊號強度與行為。

# High Energy Neutrino Detection and Neutrino Flavor Physics

Student: Tsung-Che Liu

Advisors: Guey-Lin Lin

M. A. Huang

Institute of Physics  
National Chiao Tung University

## ABSTRACT

This thesis discusses the neutrino flavor physics from the source to the Earth. In first part, we analyze the measured flavor ratios on the Earth to reconstruct the flavor ratio at the source. We also estimate the critical event numbers for distinguishing two most common astrophysical sources. We not only introduce the standard oscillation mechanism but also neutrino decay mechanisms into the propagations of neutrinos. Applying the currently understood of neutrino mixing angle ranges, we obtain the corresponding flavor ratios on the Earth for different propagation mechanisms. In the second part, we discuss the neutrino detections. We simulate neutrinos interacting with the Earth and record the lepton fluxes inside the detector sensitive region. The leptons generate the electromagnetic and hadronic showers. We use CORSIKA simulate these showers and estimate the resulting synchrotron radiations.

# 致 謝

僅以本書獻給感謝我的指導教授，林貴林與黃明輝兩位老師。與協力完成本論文的每個人。

在物理所七年，聽到稱讚林老師的話多不勝數，但我完全沒有聽過有人抱怨過林老師一句。林老師的為人已達到“背後無人語”的境界。因此每個畢業的同學在他們的致謝中，都會稱讚老師高尚的品格和外圓內方的研究態度。這些好話用在很多人身上只會讓人覺得溢美與虛假，但用在林老師身上則是完全的貼和。林老師不只是我在學問上的恩師，也是我為人處事的典範。而黃明輝老師則是在我的博士生涯樹立了另外一盞明燈，在學術上，老師常常以機敏百出的思維來處理物理問題，使我每每都只能在心裡暗地驚嘆與佩服，難以望其項背。而在生活及其他方面，黃老師待我視同己出，常常原諒我過度的怠惰與偏執，並妥善的指出我應當行的路。在此我只能說：“選擇兩位恩師當我的指導教授是一生我的榮幸，是我進交大後最正確也是最重要的決定。”

這篇論文的內容，並不是由我一人獨立完成。交大高能團隊的每個人都在不同的部份有所參與與貢獻：首先感謝王正祥老師在每個章節都給予我不同的意見，讓我可以學術上適度地修正研究方向。而在生活上，則是指正我過度奢靡的生活態度。讓我稍稍地控管自己的財政支出。最後我也必須感謝王老師在聯合大學給我的各項照顧，讓我減輕經濟上的負擔。而永順，振軒，光昶，志清四位是則除了老師們以外，讓本論文得以完成的最主要功臣。每當我在程式，在物理，甚至是硬體上遇到難關無法突破時，他們四位常常伸出援手，讓我得以繼續下去。他們是我在博士生涯的四位貴人。最後感謝鳳吟，瑜隆，峰旭，貝禎，禹廷，志榮，念潔與高

能團隊的各位的幫忙與指導.

以下是特別感謝名單:

FLASH-TW 實驗: (2003-2005). 感謝同步輻射許國棟組長與許森元先生幫忙建立整個實驗平台. 許組長以他豐富的經驗給與我許多寶貴的意見. 在他的身上我看到一個一流的實驗學家如何由零開始一步一步建立整個實驗. 另外許森元先生謹慎的設計.則是讓我們的實驗能被正確運作的最重要關鍵. 沒有他們兩位的關注,本實驗絕對無法進行下去.

Neutrino Interaction Simulation in IHEP (2007). 感謝曹臻,何會海與查敏三位老師給我在北京高能所學習的機會. 在北京我見識到微中子觀測實驗如何與電腦模擬相結合. 他們三位常常在會議中進行廢寢忘食的激烈論戰,有系統地呈現各方的意見,只為求得科學上的真相. 這樣的研究精神深深地讓我折服. 另外也要感謝劉加麗, 白云翔, 肖剛, 張丙開, 張壽山等好朋友在生活與研究上給我各種協助. 沒有他們, 別說是作研究了, 我大概連怎麼在北京生活都會成問題.

Geant4 Simulation (2008). 感謝王正祥老師與陳鎰鋒老師讓我有機會參加Geant4 團隊的研討會並實際了解KEK如何的運作. 在那次經驗, KEK的Sasaki教授讓我見識到國際一流團隊如何撰寫程式, 如何反覆推敲每一個環節以達到真實世界所需要的精度. 這使我在Geant4模擬的工作上有著長足的進步. 雖然在這篇論文內, 我沒有加入質子治療的各項模擬結果. 但我必須特別感謝以上團隊的協助.

Geosynchrotron Raiation Detector (2008-2009). 這裡必須感謝韓國梨花大學南智悟(Nam JiWoo)教授在我們團隊期間給予關於實驗的各種實務經驗. 有他的引領我們才漸漸的建立起如何地球同步輻射光與高能微中子的關聯.

交大物理成員(2003-2008). 感謝博士班內一同為資格考廝殺的92級兄弟們, 也感謝半夜一同吃宵夜的胖子團隊. 無論你們現在在哪裡, 感謝你們這麼多年來的陪伴.

# Contents

<b>1</b>	<b>Introduction</b>	<b>1</b>
1.1	The Discovery of Electron Neutrino . . . . .	1
1.2	Other Types of Neutrinos . . . . .	2
<b>I</b>	<b>Neutrino Flavor Physics</b>	<b>4</b>
<b>2</b>	<b>Neutrino Flavor Ratio at the Astrophysical Source</b>	<b>5</b>
2.1	Sources of Ultra-high Energetic Neutrinos . . . . .	5
2.1.1	AGN (Active Galactic Nucleus) Neutrinos . . . . .	5
2.1.2	GZK ( Greisen-Zetsepin-Kuzmin ) Neutrinos . . . . .	6
2.2	Pontecorvo-Maki-Nakagawa-Sakata Mixing Matrix and Flavor Transition Probability Matrix . . . . .	6
2.3	Observed Neutrino Events in Detector . . . . .	13
2.4	Reconstructing Source Flavor Ratios at Low Energies . . . . .	16
2.4.1	The Reconstruction of Initial Neutrino Flavor Ratio by Measuring $R^I$ Alone 18	
2.4.2	The Flavor Reconstruction with Measurements on Both $R$ and $S$ . . . . .	18
2.4.2.1	$(\sin^2 \theta_{13})_{\text{best fit}} = 0$ . . . . .	19
2.4.2.2	$(\sin^2 \theta_{13})_{\text{best fit}} > 0$ . . . . .	21
2.4.3	Critical Accuracies Needed for Distinguishing Astrophysical Sources. . .	21
2.5	Reconstructing Flavor Ratio of Source at High Energy. . . . .	23
2.5.1	The Reconstruction of Muon-damped Source . . . . .	25

2.5.2	The Reconstruction of Pion Source . . . . .	25
2.5.3	$R^{\text{II}}$ and Tri-bimaximal Limit . . . . .	26
2.6	Reconstructing Flavor Ratio of Source by Monte Carlo Method with N Events . . . . .	29
2.6.1	The Flavor Ratios on the Earth from Pion Source with 200 Events . . . . .	29
2.6.1.1	The Reconstructed Neutrino Flavor Ratios at Low Energy, $E_{\nu} \leq 33.3$ PeV . . . . .	29
2.6.1.2	The Reconstructed Neutrino Flavor Ratios at High Energy, $E_{\nu} \geq 33.3$ PeV . . . . .	32
2.6.2	The flavor ratios on the Earth from the Muon-damped source with 200 events . . . . .	33
2.6.2.1	The Reconstructed Neutrino Flavor Ratios at Low Energy, $E_{\nu} \leq 33.3$ PeV . . . . .	33
2.6.2.2	The Reconstructed Neutrino Flavor Ratios at High Energy, $E_{\nu} \geq 33.3$ PeV . . . . .	34
2.6.2.3	Summary of the Reconstructed Neutrino Flavor Ratios with 200 Events . . . . .	37
2.6.3	The Flavor Ratios on the Earth from Pion Source with 400 Events . . . . .	37
2.6.3.1	The Reconstructed Neutrino Flavor Ratios at Low Energy, $E_{\nu} \leq 33.3$ PeV . . . . .	38
2.6.3.2	The Reconstructed Neutrino Flavor Ratios at High Energy, $E_{\nu} \geq 33.3$ PeV . . . . .	40
2.6.4	The Flavor Ratios on the Earth from the Muon-damped Source with 400 Events . . . . .	41
2.6.4.1	The Reconstructed Neutrino Flavor Ratios at Low Energy, $E_{\nu} \leq 33.3$ PeV . . . . .	41
2.6.4.2	The Reconstructed Neutrino Flavor Ratios at High Energy, $E_{\nu} \geq 33.3$ PeV . . . . .	42
2.6.4.3	Summary of the Reconstructed Neutrino Flavor Ratios with 400 Events . . . . .	43

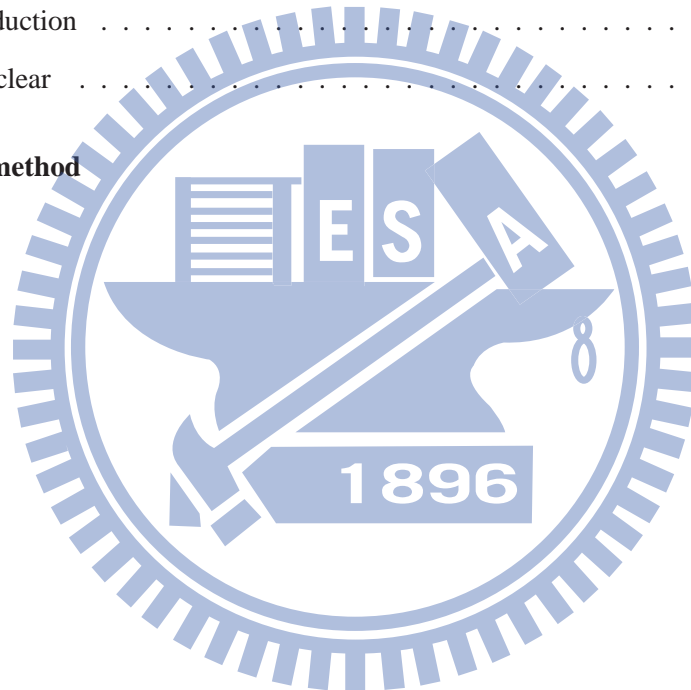
**3 Flavor Ratios on the Earth from Neutrino Decay 47**



3.1	$Q$ Matrix Representation . . . . .	47
3.1.1	$Q$ Matrix Representation for Oscillations of Astrophysical Neutrinos . . . . .	47
3.1.2	$Q$ Matrix Representation for General Flavor Transitions of Astrophysical Neutrinos . . . . .	50
3.2	Neutrino Decay Mechanisms . . . . .	51
3.3	The Range of Neutrino Flavor Ratios on the Earth . . . . .	52
3.3.1	The Heaviest and Middle Mass Eigenstates decay to the Lightest and Invisible States. . . . .	52
3.3.1.1	Normal Mass Hierarchy . . . . .	52
3.3.1.2	Inverted Mass Hierarchy . . . . .	53
3.3.2	The Heaviest Mass Eigenstate Decays to the Middle, Lightest and Invisible States . . . . .	54
3.3.2.1	Normal Mass Hierarchy . . . . .	54
3.3.2.2	Inverted Mass Hierarchy . . . . .	54
3.3.3	The Middle Mass Eigenstate Decays to the Lightest and Invisible States . . . . .	56
3.3.3.1	Normal Mass Hierarchy . . . . .	56
3.3.3.2	Inverted Mass Hierarchy . . . . .	56
3.3.4	The Lightest Mass Eigenstate decays to Invisible States Only . . . . .	58
3.3.4.1	Normal Mass Hierarchy . . . . .	58
3.3.4.2	Inverted Mass Hierarchy . . . . .	59
3.3.5	The Middle and Lightest Mass Eigenstates decay to Invisible States Only . . . . .	60
3.3.5.1	Normal Mass Hierarchy . . . . .	60
3.3.5.2	Inverted Mass Hierarchy . . . . .	60
3.3.6	The heaviest and lightest mass eigenstates decay to the middle mass eigenstate and invisible states only . . . . .	61
3.3.6.1	Normal Mass Hierarchy . . . . .	61
3.3.6.2	Inverted Mass Hierarchy . . . . .	62
3.4	The Most Probable Neutrino Flavor Ratios on the Earth Induced by Standard Neutrino Oscillation and Neutrino Decays . . . . .	63

<b>II</b>	<b>High Energy Neutrino Detection</b>	<b>65</b>
<b>4</b>	<b>Simulation of High Energy Neutrino Interacting with the Earth</b>	<b>66</b>
4.1	Introduction . . . . .	66
4.2	Interactions . . . . .	67
4.2.1	Energy Loss of Leptons . . . . .	67
4.2.1.1	Ionization . . . . .	68
4.2.1.2	Bremsstrahlung . . . . .	69
4.2.1.3	Pair production . . . . .	70
4.2.1.4	Photonuclear . . . . .	70
4.2.2	Lepton decay . . . . .	70
4.2.3	Neutrino Charged Current and Neutral Current Interaction . . . . .	71
4.3	Environments . . . . .	72
4.3.1	Earth's Density Model in SHINIE . . . . .	73
4.3.2	Detector Sensitive Region (DSR) . . . . .	74
4.4	Controls of Simulation . . . . .	77
4.5	Running Options . . . . .	77
<b>5</b>	<b>Geosynchrotron Raiation Detector</b>	<b>79</b>
5.1	Extensive Air Shower (EAS) . . . . .	80
5.1.1	Longitudinal Profile . . . . .	80
5.1.2	Lateral Distribution Function . . . . .	80
5.2	CORSIKA Simulation . . . . .	82
5.2.0.1	Electron Shower . . . . .	82
5.2.0.2	Pion Shower . . . . .	83
5.2.0.3	Kaon Shower . . . . .	83
5.3	Radiation Emission from Air Shower . . . . .	93
5.3.1	Radiation by a Moving Charge . . . . .	93
5.3.2	The Radiation form the Electron-positron Pairs . . . . .	94
5.3.3	Pulse Reconstruction . . . . .	95

<b>6 Shower Experiment with electron beam</b>	<b>99</b>
6.1 Instrument . . . . .	99
6.2 The Measurement of Shower Lateral Profile with Scintillator . . . . .	101
6.3 The Measurement of Cherenkov Radiations from Showers . . . . .	104
6.4 Geant4 Simulation . . . . .	105
<b>7 Conclusions</b>	<b>109</b>
<b>A Differential cross section of lepton energy loss</b>	<b>111</b>
A.1 Pair production . . . . .	111
A.2 Photonuclear . . . . .	112
<b>B Mont-Carlo method</b>	<b>113</b>



# List of Figures

2.1	The spectrum of AGN [1] and GZK [6] muon neutrino flux. The blue solid line shows the muon neutrino spectrum from AGN source. The red dashed line shows the muon neutrino spectrum from GZK source. . . . .	7
2.2	The ranges for the neutrino flavor ratios on the Earth resulting from standard neutrino oscillation. The numbers on each side of the triangle denote the flux fraction of a specific flavor of neutrino. The blue point marks the pion source $\phi_0(\nu_e) : \phi_0(\nu_\mu) : \phi_0(\nu_\tau) = 1/3 : 2/3 : 0$ and the red point marks the muon-damped source $\phi_0(\nu_e) : \phi_0(\nu_\mu) : \phi_0(\nu_\tau) = 0 : 1 : 0$ . In panel (a), the red and blue squares mark the corresponding neutrino flavor ratios observed on the Earth. In panel (b), we introduce uncertainties of neutrino mixing angles in the probability matrix. The red and dashed line denote neutrino flavor ratios observed on the Earth from muon-damped source in $1\sigma$ and $3\sigma$ ranges of neutrino mixing angles respectively. The blue and solid line denote neutrino flavor ratios observed on the Earth from pion source in $1\sigma$ and $3\sigma$ ranges of neutrino mixing angles respectively . . . . .	10
2.3	Different types of neutrino-induced events. Dashed lines and solid lines correspond to paths of neutrinos and leptons respectively. The ellipsoids are showers. The detectable energy range for each type of event is listed in Table 2.1. . . . .	16

2.4	The reconstructed ranges for the neutrino flavor ratios at the source with $\Delta R^I/R^I = 10\%$ only. The left and right panels are results with the muon-damped source and the pion source as the input true source respectively. The numbers on each side of the triangle denote the flux percentage of a specific flavor of neutrino. The red point marks the muon-damped source $\Phi_{0,\mu} = (0, 1, 0)$ and the blue point marks the pion source $\Phi_{0,\pi} = (1/3, 2/3, 0)$ . Gray and light gray areas respectively denote the $1\sigma$ and $3\sigma$ ranges for the reconstructed neutrino flavor ratios at the source. We choose parameter set 1 in Table 2.4 for this analysis. . . . .	19
2.5	The reconstructed ranges for the neutrino flavor ratios for an input muon-damped source with $\Delta R^I/R^I = 10\%$ and $\Delta S^I/S^I$ related to the former by the Poisson statistics, E.q. (2.17). Gray and light gray areas in the left (right) panel denote the reconstructed $1\sigma$ and $3\sigma$ ranges with the parameter set 1 (2) in Table 2.4. . . . .	20
2.6	The reconstructed ranges for the neutrino flavor ratios for an input pion source with $\Delta R^I/R^I = 10\%$ and $\Delta S^I/S^I$ related to the former by the Poisson statistics, E.q. (2.17). Gray and light gray areas in the left (right) panel denote the reconstructed $1\sigma$ and $3\sigma$ ranges with the parameter set 1 (2) in Table 2.4. . . . .	20
2.7	The reconstructed ranges for the neutrino flavor ratio at the source for an input muon-damped source with $\Delta R^I/R^I = 10\%$ and $\Delta S^I/S^I$ related to the former by the Poisson statistics, E.q. (2.17). The left panel is obtained with $\theta_{13}$ and $\theta_{23}$ taken from the parameter set 1 in Table 2.4 and the input CP phase taken to be $0, \pi/2$ and $\pi$ respectively. The right panel is obtained with the parameter sets 3a, 3b and 3c in Table 2.4. Light gray area, dashed blue and dashed red lines correspond to the $3\sigma$ ranges for the reconstructed neutrino flavor ratio at the source for $\cos \delta = 1, \cos \delta = 0$ and $\cos \delta = -1$ respectively. Gray area, blue and red lines correspond to the $1\sigma$ ranges for the reconstructed neutrino flavor ratio at the source for $\cos \delta = 1, \cos \delta = 0$ and $\cos \delta = -1$ respectively. The effect from the CP phase $\delta$ only appears in the right panel. . . . .	22

2.8	The reconstructed $1\sigma$ and $3\sigma$ ranges for the neutrino flavor ratio at the source for an input pion source with $\Delta R^l/R^l = 10\%$ and $\Delta S^l/S^l$ related to the former by the Poisson statistics. The choices of parameter sets are identical to those of Fig. 2.7. Once more, the effect from the CP phase $\delta$ only appears in the right panel. . . .	22
2.9	Critical accuracies needed to distinguish between the pion source and the muon-damped source. In the left panel where the muon-damped source is the true source, the reconstructed $3\sigma$ range for the neutrino flavor ratio just touches the pion source at $\Delta R^l/R^l = 11\%$ and $\Delta S^l/S^l$ related to the former by the Poisson statistics, E.q. (2.17). In the right panel where the pion source is the true source, the reconstructed $3\sigma$ range for the neutrino flavor ratio just touches the muon-damped source at $\Delta R^l/R^l = 4\%$ and $\Delta S^l/S^l$ related to the former by the Poisson statistics, E.q. 2.17.. We choose parameter set 1 in Table 2.4 for this analysis. . .	23
2.10	Reconstructed ranges for muon-damped source with $\Delta R^a/R^a = 10\%$ and $\Delta S^a/S^a = 12\%$ . The dark and light shaded areas denote the range of reconstructed neutrino flavor ratios under $1\sigma$ and $3\sigma$ limits. The left and right panels correspond to the condition I and II. The pion source can be ruled out at the $3\sigma$ level for both conditions. . . . .	25
2.11	Reconstructed ranges for muon-damped source with $\Delta R^a/R^a = 10\%$ only. The dark and light shaded areas denote the range of reconstructed neutrino flavor ratios under $1\sigma$ and $3\sigma$ limits. The left and right panels correspond to the condition I and II. The pion source can be ruled out at $3\sigma$ level for the condition II but not for the condition I even at $1\sigma$ level. . . . .	26
2.12	Reconstructed ranges for pion source with $\Delta R^a/R^a = 10\%$ and $\Delta S^a/S^a = 12\%$ . The dark and light shaded areas denote the range of reconstructed neutrino flavor ratios under $1\sigma$ and $3\sigma$ limits. The left and right panels correspond to the condition I and II. The muon-damped source can be ruled out at the $1\sigma$ level for both conditions. . . . .	27

2.13	Reconstructed ranges for pion source with $\Delta R^a/R^a = 10\%$ only. The dark and light shaded areas denote the range of reconstructed neutrino flavor ratios under $1\sigma$ and $3\sigma$ limits. The left and right panels correspond to the condition I and II. For condition I, $3\sigma$ limit covers all flavor ratio of source. But the muon-damped source can be ruled out at $1\sigma$ level for condition II. . . . .	27
2.14	Measured flux ratios for input source ratios, $\phi_0(\nu_e) : \phi_0(\nu_\mu) : \phi_0(\nu_\tau) = \alpha : 1 - \alpha : 0$ with $0 \leq \alpha \leq 1$ . The thick and long dashed lines correspond to $R^{\text{II}}$ and $S^{\text{II}}$ respectively. The thin and short-dashed lines denote $R^{\text{I}}$ and $S^{\text{I}}$ respectively. It is seen that $S^{\text{I}}$ and $R^{\text{II}}$ are more sensitive to $\alpha$ ; while $R^{\text{I}}$ and $S^{\text{II}}$ are less sensitive to this parameter. . . . .	28
2.15	The distribution of neutrino flavor ratio on the Earth from pion source for 200 events. Each flavor ratio on the ternary plot is generated by 200 events. There are 10 million flavor ratios generated on the ternary plot, which form the distribution of flavor ratios. The blue point denotes the original flavor ratio of pion source. In panel (a), the distribution of flavor ratios is cut off at 99.7%. In panel (b), the distribution of flavor ratios is cut off at 68.2%. . . . .	30
2.16	The reconstructed ranges for pion source with 200 events and neutrino energy below 33.3 PeV. The range for possibly measured flavor ratio is cut off at 99.7%. The dark and light shades area denote $1\sigma$ and $3\sigma$ reconstructed ranges. . . . .	31
2.17	The reconstructed ranges for pion source with 200 events and neutrino energy below 33.3 PeV. The range for possibly measured flavor ratio is cut off at 68.2%. The dark and light shades area denote $1\sigma$ and $3\sigma$ reconstructed ranges. . . . .	32
2.18	The reconstructed ranges for pion source with 200 events and neutrino energy above 33.3 PeV. The range for possibly measured flavor ratio is cut off at 99.7%. The dark and light shades area denote $1\sigma$ and $3\sigma$ reconstructed ranges. . . . .	33
2.19	The reconstructed ranges for pion source with 200 events and neutrino energy above 33.3 PeV. The range for possibly measured flavor ratio is cut off at 68.2%. The dark and light shades area denote $1\sigma$ and $3\sigma$ reconstructed ranges. . . . .	34

2.20	The distribution of neutrino flavor ratio on the Earth from muon-damped source for 200 events. Each flavor ratio on the ternary plot is generated by 200 events. There are 10 million flavor ratios generated on the ternary plot, which form the distribution of flavor ratios. The red point denotes the original flavor ratio of muon-damped source. In panel (a), the distribution of flavor ratios is cut off at 99.7%. In panel (b), the distribution of flavor ratios is cut off at 68.2%. . . . .	35
2.21	The reconstructed ranges for muon-damped source with 200 events and neutrino energy below 33.3 PeV. The range for possibly measured flavor ratio is cut off at 99.7%. The dark and light shades area denote $1\sigma$ and $3\sigma$ reconstructed ranges. .	36
2.22	The reconstructed ranges for muon-damped source with 200 events and neutrino energy below 33.3 PeV. The range for possibly measured flavor ratio is cut off at 68.2%. The dark and light shades area denote $1\sigma$ and $3\sigma$ reconstructed ranges. .	36
2.23	The reconstructed ranges for muon-damped source with 200 events and neutrino energy above 33.3 PeV. The range for possibly measured flavor ratio is cut off at 99.7%. The dark and light shades area denote $1\sigma$ and $3\sigma$ reconstructed ranges. .	37
2.24	The reconstructed ranges for muon-damped source with 200 events and neutrino energy above 33.3 PeV. The range for possibly measured flavor ratio is cut off at 68.2%. The dark and light shades area denote $1\sigma$ and $3\sigma$ reconstructed ranges. .	38
2.25	The distribution of neutrino flavor ratio on the Earth from pion source for 400 events. Each flavor ratio on the ternary plot is generated by 400 events. There are 10 million flavor ratios generated on the ternary plot, which form the distribution of flavor ratios. The blue point denotes the original flavor ratio of pion source. In panel (a), the distribution of flavor ratios is cut off at 99.7%. In panel (b), the distribution of flavor ratios is cut off at 68.2%. . . . .	39
2.26	The reconstructed ranges for pion source with 400 events below 33.3 PeV. The range for possibly measured flavor ratio is cut off at 99.7%. The dark and light shades area denote $1\sigma$ and $3\sigma$ reconstructed ranges. . . . .	40



2.27	The reconstructed ranges for pion source with 400 events below 33.3 PeV. The range for possibly measured flavor ratio is cut off at 68.2%. The dark and light shades area denote $1\sigma$ and $3\sigma$ reconstructed ranges. . . . .	41
2.28	The reconstructed ranges for pion source with 400 events and neutrino energy above 33.3 PeV. The range for possibly measured flavor ratio is cut off at 99.7%. The dark and light shades area denote $1\sigma$ and $3\sigma$ reconstructed ranges. . . . .	42
2.29	The reconstructed ranges for pion source with 400 events and neutrino energy above 33.3 PeV. The range for possibly measured flavor ratio is cut off at 68.2%. The dark and light shades area denote $1\sigma$ and $3\sigma$ reconstructed ranges. . . . .	43
2.30	The distribution of neutrino flavor ratio on the Earth from muon-damped source for 400 events. Each flavor ratio on the ternary plot is generated by 400 events. There are 10 million flavor ratios generated on the ternary plot, which form the distribution of flavor ratios. The red point denotes the original flavor ratio of muon-damped source. In panel (a), the distribution of flavor ratios is cut off at 99.7%. In panel (b), the distribution of flavor ratios is cut off at 68.2%. . . . .	44
2.31	The reconstructed ranges for muon-damped source with 400 events below 33.3 PeV. The range for possibly measured flavor ratio is cut off at 99.7%. The dark and light shades area denote $1\sigma$ and $3\sigma$ reconstructed ranges. . . . .	45
2.32	The reconstructed ranges for muon-damped source with 400 events below 33.3 PeV. The range for possibly measured flavor ratio is cut off at 68.2%. The dark and light shades area denote $1\sigma$ and $3\sigma$ reconstructed ranges. . . . .	45
2.33	The reconstructed ranges for muon-damped source with 400 events above 33.3 PeV. The range for possibly measured flavor ratio is cut off at 99.7%. The dark and light shades area denote $1\sigma$ and $3\sigma$ reconstructed ranges. . . . .	46
2.34	The reconstructed ranges for muon-damped source with 400 events above 33.3 PeV. The range for possibly measured flavor ratio is cut off at 68.2%. The dark and light shades area denote $1\sigma$ and $3\sigma$ reconstructed ranges. . . . .	46

3.1	<p>The ranges for the neutrino flavor ratios on the Earth resulting from standard neutrino oscillation. The left panel shows the range of neutrino flavor ratios from the source flavor ratios, <math>\phi_0(\nu_e) : \phi_0(\nu_\mu) : \phi_0(\nu_\tau) = \alpha : 1 - \alpha : 0</math>, with <math>0 \leq \alpha \leq 1</math>. The violet and orange colors correspond the <math>1\sigma</math> and <math>3\sigma</math> level of neutrino mixing angles respectively. The left panel shows the range of neutrino flavor ratios from the source flavor ratios, <math>\phi_0(\nu_e) : \phi_0(\nu_\mu) : \phi_0(\nu_\tau) = \alpha : \beta : 1 - \alpha - \beta</math>, with <math>\alpha &gt; 0</math>, <math>\beta &gt; 0</math> and <math>\alpha + \beta \leq 1</math>. The violet and orange colors correspond the <math>1\sigma</math> and <math>3\sigma</math> level of neutrino mixing angles respectively. The values of mixing angles are same as the set 1 in Table 2.5. . . . .</p>	48
3.2	<p>The range of flavor ratios on the Earth from the heaviest and middle mass eigenstates decay to the lightest mass eigenstate and invisible states. The final branching ratios of the heaviest and lightest mass eigenstates are <math>Br_{H \rightarrow L} + Br_{H \rightarrow \text{invisible}} = 1</math> and <math>Br_{M \rightarrow L} + Br_{M \rightarrow \text{invisible}} = 1</math>. Panel (a) shows the range of flavor ratios on the Earth in the normal mass hierarchy. Panel (b) shows the range of flavor ratios on the Earth in the inverted mass hierarchy. . . . .</p>	53
3.3	<p>The range of flavor ratios on the Earth from the heaviest mass eigenstate decays to the middle, lightest and invisible state in the normal mass hierarchy. Panel (a) shows the range of flavor ratios on the Earth from the heaviest eigenstate decays to invisible eigenstates only. Panel (b) shows the range of flavor ratios on the Earth from the heaviest eigenstate decays to the middle eigenstate only. Panel (c) shows the range of flavor ratios on the Earth from the heaviest eigenstate decays to the lightest eigenstate only. Panel (d) shows the all possible flavor ratios on the Earth which satisfy <math>Br_{H \rightarrow M} + Br_{H \rightarrow L} + Br_{H \rightarrow \text{invisible}} = 1</math>. . . . .</p>	55

3.4	<p>The range of flavor ratios on the Earth from the heaviest mass eigenstate decays to the middle, lightest and invisible state in the inverted mass hierarchy. Panel (a) shows the range of flavor ratios on the Earth from the heaviest eigenstate decays to invisible eigenstates only. Panel (b) shows the range of flavor ratios on the Earth from the heaviest eigenstate decays to the middle eigenstate only. Panel (c) shows the range of flavor ratios on the Earth from the heaviest eigenstate decays to the lightest eigenstate only. Panel (d) shows the all possible flavor ratios on the Earth which satisfy <math>Br_{H \rightarrow M} + Br_{H \rightarrow L} + Br_{H \rightarrow \text{invisible}} = 1</math>. . . . .</p>	57
3.5	<p>The range of flavor ratios on the Earth from the middle mass eigenstate decays to the lightest and invisible states. The branching ratio, <math>Br_{M \rightarrow L} + Br_{M \rightarrow \text{invisible}} = 1</math>, for both hierarchy. Panel (a) shows the flavor ratios on the Earth from the middle mass eigenstate decays to the lightest and invisible states in the normal mass hierarchy. In this case, the range of flavor ratios on the Earth from the heaviest mass eigenstate decay in the inverted mass hierarchy is same as the middle mass eigenstate decay in the normal mass hierarchy. Panel (b) shows the flavor ratios on the Earth from the middle mass eigenstate decays to the lightest and invisible states in the inverted mass hierarchy. . . . .</p>	58
3.6	<p>The range of flavor ratios on the Earth from the lightest mass eigenstate decays to invisible states only. The lightest neutrino mass eigenstate decays to invisible state only. The branching ratio, <math>Br_{L \rightarrow \text{invisible}} = 1</math>, for both hierarchy. Panel (a) shows the lightest eigenstate decays to invisible states in the normal mass hierarchy. The possible flavor ratios are same as the case of the middle mass eigenstate decay. Panel (b) shows the lightest eigenstate decays to invisible state only in the inverted mass hierarchy. The possible flavor ratios are same as the case of the heaviest mass eigenstate decay in the normal mass hierarchy. . . . .</p>	59

3.7	The range of flavor ratios on the Earth from the middle and the lightest mass eigenstates decay to invisible states. The middle mass eigenstate can decay to the lightest and invisible eigenstates, but the lightest neutrino mass eigenstate only can decay to invisible state. Hence the final branching ratios of the middle and lightest mass eigenstates are $Br_{M \rightarrow \text{invisible}} = 1$ and $Br_{L \rightarrow \text{invisible}} = 1$ for both hierarchy. Panel (a) shows the middle and lightest mass eigenstates decay to invisible states in the normal mass hierarchy. Panel (b) shows the middle and lightest mass eigenstates decay to invisible states only in the inverted mass hierarchy. . . . .	61
3.8	The range of flavor ratios on the Earth from the heaviest and lightest mass eigenstates decay to the middle mass eigenstate and invisible states. The heaviest mass eigenstate can decay to the middle mass eigenstate and invisible eigenstates, but the lightest neutrino mass eigenstate only can decay to invisible eigenstates. Hence the final branching ratios of the heaviest and lightest mass eigenstates are $Br_{H \rightarrow M} + Br_{H \rightarrow \text{invisible}} = 1$ and $Br_{L \rightarrow \text{invisible}} = 1$ for both hierarchy. Panel (a) shows the possible flavor ratios on the Earth in the normal mass hierarchy. Panel (b) shows the possible flavor ratios on the Earth in the inverted mass hierarchy. . . . .	62
3.9	The neutrino flavor ratios on the Earth induced by different flavor transition mechanisms. The left panel shows the range of flavor ratios on the Earth from decay and oscillation in $1\sigma$ level. The right panel shows the ranges at $3\sigma$ level. Both panels show the most probable flavor ratios on the Earth is around $\phi_0(\nu_e) : \phi_0(\nu_\mu) : \phi_0(\nu_\tau) = 1/3 : 1/3 : 1/3$ . . . . .	64
4.1	The range of tau leptons in materials. Blue, red and orange lines correspond to the range of tau leptons in water, standard rock, and iron respectively. The range of tau in iron is much lower than standard rock and water at $10^{20}$ eV. . . . .	68
4.2	Charged current (CC) and neutral current (NC) interaction cross section in SHINIE, according the the CTEQ6-DIS parton distributions. The red and blue curves are CC and NC interaction cross section, respectively, for $10^5 \leq E_\nu \leq 10^{11}$ GeV. . . . .	73
4.3	density model of earth . . . . .	74
4.4	The grid map data with altitudes. . . . .	75

4.5	Detector sensitive region (DSR). The size, material and position of DSR can be defined by user. SHINIE record all information of particles within this area. . . . .	76
4.6	Graphic interface system . . . . .	78
5.1	The relationship between slant depth and propagation distance in the air with constant density. Blue, red, yellow and green lines correspond to the transition rate for horizontal shower develop in sea level, 2 km, 4 km and 6 km altitudes. The densities of those altitudes are 1.23 kg/m <sup>3</sup> , 1.01 kg/m <sup>3</sup> , 0.82 kg/m <sup>3</sup> and 0.66 kg/m <sup>3</sup> . . . . .	81
5.2	Mean longitudinal profile of 30 electron showers at five input energies. . . . .	84
5.3	Lateral profile of electron showers at five input energies. . . . .	85
5.4	Lorentz factor distribution of electron showers at five input energies. . . . .	86
5.5	longitudinal profile of pion showers at five input energies. . . . .	87
5.6	longitudinal profile of pion showers at five input energies. . . . .	88
5.7	The longitudinal profile of pion showers at five input energies. . . . .	89
5.8	longitudinal profile of kaon showers at five input energies. . . . .	90
5.9	The lateral profile of kaon showers at five input energies. . . . .	91
5.10	The Lorentz factor distribution of kaon showers at five input energies. . . . .	92
5.11	Geometry of synchrotron radiation. Blue point denotes the particle moving with velocity $v$ . Red line is the trajectory of particle lies in $x-y$ plane with radius $\rho$ . $\hat{e}_{\parallel}$ is the unit vector corresponding to the polarization in the plane of orbit and $\hat{e}_{\perp}$ is the unit vector of the other polarization, which perpendicular to the $\hat{e}_{\parallel}$ and emission direction $n$ . . . . .	94
5.12	Off-set dependence of $ E(R, 2\pi\nu) $ of a $10^{17}$ eV shower at the observation distance of 10 km. Curves in blue, red and orange represent signals in observing frequencies of 50 MHz, 75 MHz and 100 MHz respectively. . . . .	95

5.13	Reconstructed pulses from emission of $10^{17}$ and $10^{17.5}$ eV electron shower at the observation distance of 10 km, using an idealized rectangular filter spanning 30 – 80 MHz. The strength of signal is proportional to the energy of shower. The curves in blue, red, orange and green denote pulses measured at center, at lateral distances of 500 m 1000 m and 1500 m, respectively. The pink and gray curves are measured at lateral distances of 2000 m and 2500 m and close to the $x$ axis, and the signals are too weak to be distinguished. . . . .	97
5.14	Reconstructed pulses from emission of a $10^{17.5}$ eV pion shower at the observation distance of 10 km, using an idealized rectangular filter spanning 30 – 80 MHz. The curves in blue, red, orange and green denote pulses measured at center, at lateral distances of 500 m 1000 m and 1500 m, respectively. The pink and gray curves are measured at lateral distances of 2000 m and 2500 m and close to the $x$ axis, and the signals are too weak to be distinguished. . . . .	98
5.15	Reconstructed pulses from emission of a $10^{17.5}$ eV kaon shower at the observation distance of 10 km, using an idealized rectangular filter spanning 30 – 80 MHz. The curves in blue, red, orange and green denote pulses measured at center, at lateral distances of 500 m 1000 m and 1500 m, respectively. The pink and gray curves are measured at lateral distances of 2000 m and 2500 m and close to the $x$ axis, and the signals are too weak to be distinguished. . . . .	98
6.1	Top view of the experimental platform. The 1.5 GeV electron beams enter the chambers from the left hand side. The secondary charge particles are generated while incident electrons are passing through the aluminum targets. The secondary charge particles hit the scintillation screen placed in the second chamber and generate scintillation light, which is recorded by the CCD camera. . . . .	100
6.2	Results from the decay-time measurement. This decay-time of the scintillation light from scintillator is measured by photo-diode and digital multi-meter. The first decay pattern has a short decay time about 3.4 ms, the second one has a longer decay time about 6.7 ms and the third one has a decay time longer than 15 minutes. . . . .	102

6.3	The fluorescence spectrum of AF995r scintillator ( $\text{Al}_2\text{O}_3:\text{Cr}^{3+}$ ). Two close peaks located at wavelengths 692.8 nm and 694.0 nm are clearly seen. . . . .	102
6.4	The shower image recorded by the CCD camera at 2.5 radiation length. The x and y axes labels the pixels number of CCD chip. The z axis is the count of photos record by CCD camera. . . . .	103
6.5	The shower longitudinal profile record by the CCD camera. The CCD camera integrates the fluorescence photons spread over the $X - Y$ plane for each radiation length and obtain the shower longitudinal profile. . . . .	103
6.6	The number of photons emitted from an electron with in the wavelength between 380 nm to 780 nm. The threshold energy is about 21 MeV with refractive index of air is 1.00029. The photons numbers saturate close to 35 photons per meter above 100 MeV. . . . .	105
6.7	The platform structure setting of Geant4 simulation. The blue lines indicate the track of electrons, pink lines are emitted photons by charge. The incident electron beam hit the 2 mm thick aluminium window first, then lose the energy within aluminium radiators. The electrons emit the Cherenkov photons while electron pass the air, but the CCD record the photons only after electrons pass the third aluminium window. . . . .	107
6.8	The longitudinal profiles of experimental data and Geant4 simulation result. The blue squares are experiment data, which record the Cherenkov photons by CCD. The red line is the result of Geant4 simulation. Both data and simulation result show the shower maximum are close to $2.3 r.l.$ . . . . .	108

# List of Tables

1.1	The properties of lepton generations. Since the neutrino flavor eigenstates are combinations of neutrino mass eigenstates, we do not list the neutrino mass in this table. The relations between those three neutrino flavor eigenstates and mass eigenstates are discussed in chapter 2. . . . .	3
2.1	Different types of neutrino induced events. . . . .	13
2.2	The definitions of $R$ and $S$ at different energy ranges. . . . .	15
2.3	Parameter sets chosen for our analysis . . . . .	18
2.4	True values of neutrino flavor ratios on the Earth . . . . .	18
2.5	Neutrino mixing parameters . . . . .	24
3.1	The neutrino decay and oscillation scenarios. The suffix “H”, “M”, and “L” label the heaviest, middle and lightest mass eigenstates. The number “1”, “2” and “3” label $\nu_1$ , $\nu_2$ and $\nu_3$ mass eigenstates. The red numbers and black numbers correspond to the unstable and stable eigenstates respectively. . . . .	52
4.1	The parameters in Bethe-Bloch formula . . . . .	69
4.2	The Density of Earth, $R_f$ is fraction of earth radius. The density of the Earth. The symbol “ $R$ ” is the distance from the center of the Earth to an observable location. . . . .	75
4.3	Status identifications as used in SHINIE. . . . .	76
4.4	Particle identifications as used in SHINIE. . . . .	77
4.5	Running command . . . . .	78



5.2 The major branching ratios of  $\tau$ . There are 31 basic decay mode of  $\tau$ . The total branching ratio of first 6 decay channels is more than 90%. . . . . 82

6.1 The setting of Geant4 operating environment and simulation parameters. . . . . 106

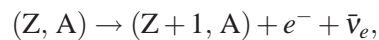


# Chapter 1

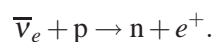
## Introduction

### 1.1 The Discovery of Electron Neutrino

The history of neutrino began from the  $\beta$ -decay experiment. In 1914, J. Chadwick discovered that energy spectrum of the  $\beta$ -decay electrons is a continuous distribution. This result cannot be explained by the nuclear model of  $\beta$ -decay at that time and implies that the  $\beta$ -decay may not be a two-body decay process. W. Pauli tried to interpret  $\beta$ -decay as a three-body decay process and introduced a new neutral particle carrying spin 1/2 to ensure the angular momentum conservation. In 1933 E. Fermi named that particle as neutrino,  $\nu$ , and extended Pauli's idea to his weak interaction theory. The reaction of  $\beta$ -decay is



where  $Z$  and  $A$  denote the atomic number and mass number respectively and the subscript “ $e$ ” indicates the flavor of neutrino. Based on Pauli's theory, H. Bethe and R. Peierls predicted the cross section of neutrinos interact with matter should be much smaller than the one of electrons. The first discovery of neutrinos is made by F. Reines and C. Cowen from inverse  $\beta$ -decay reaction,



They used the nuclear reactor as the source to generate a huge amount of antineutrinos. The neutrinos interact with aqueous solution of cadmium chloride and emit the neutron and positron.

F. Reines and C. Cowen detected the radiated  $\gamma$  from positron annihilation and neutron interacting with cadmium to establish the neutrino events.

## 1.2 Other Types of Neutrinos

Muon is a particle with a negative electric charge and carries spin 1/2. Most properties of muon are the same as those of the electron, but the rest mass of muon,  $105.7 \text{ MeV}/c^2$ , is 200 times heavier than the rest mass of the electron. The first discovery of muon was made by C. D. Anderson and S. Neddermeyer in 1936 from cosmic ray experiment. Those muons are generated by cosmic ray colliding with nuclei in the atmosphere. Since the muon is not the lightest lepton, it decays to electron. The lifetime of muon is  $2.2 \times 10^{-6} \text{ s}$  and the process of muon decay is

$$\mu^- \rightarrow e^- + \bar{\nu}_e + \nu_\mu.$$

This process conserves the muon lepton number,  $L_\mu$ , and charge. Table 1.1 lists properties of lepton generations. In order to conserve the lepton number, muon neutrino and anti-electron neutrino are generated in muon decay. The other lepton is tau, which was discovered in linear collider experiment in 1975. Tau is more massive than other leptons and its rest mass is  $1.777 \text{ MeV}/c^2$ . Since the tau is the heaviest lepton, it could decay to electron or muon. The lifetime of tau is about  $2.9 \times 10^{-13} \text{ s}$ . The tau has several decay channels. We list the major decay channels in Table 5.2. The purely leptonic decay channels are

$$\tau^- \rightarrow e^- + \bar{\nu}_e + \nu_\tau \quad (17.85 \pm 0.06\%)$$

and

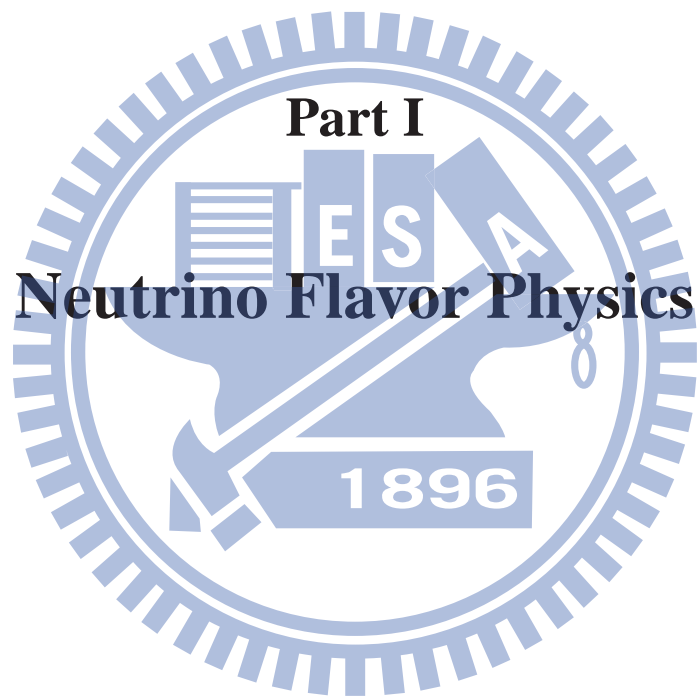
$$\tau^- \rightarrow \mu^- + \bar{\nu}_\mu + \nu_\tau \quad (17.36 \pm 0.05\%).$$

Unlike other particles, neutrinos interact with matter very weakly and may not decay to other particles. Hence they keep a lot of information about their origin. One can probe the astrophysical object by measuring neutrino. Based on the understanding of neutrino oscillation and mixing

Generations	Name	Electric charge	Lepton number	Mass
First	electron	-1	$L_e = 1, L_\mu = 0, L_\tau = 0$	0.511 MeV/c <sup>2</sup>
	electron neutrino	0	$L_e = 1, L_\mu = 0, L_\tau = 0$	
Second	muon	-1	$L_e = 0, L_\mu = 1, L_\tau = 0$	105.658 MeV/c <sup>2</sup>
	muon neutrino	0	$L_e = 0, L_\mu = 1, L_\tau = 0$	
Third	tau	-1	$L_e = 0, L_\mu = 0, L_\tau = 1$	1.777 GeV/c <sup>2</sup>
	tau neutrino	0	$L_e = 0, L_\mu = 0, L_\tau = 1$	

Table 1.1: The properties of lepton generations. Since the neutrino flavor eigenstates are combinations of neutrino mass eigenstates, we do not list the neutrino mass in this table. The relations between those three neutrino flavor eigenstates and mass eigenstates are discussed in chapter 2.

angles, we can establish the relation of neutrino flavor ratio at the source and that on the Earth. In chapter 2, we reconstruct the possible flavor ratio at the astrophysical source by measuring the flavor ratio on the Earth. If neutrino can decay, the neutrino flavor ratio on the Earth should be different from that predicted by neutrino oscillation. In chapter 3, we demonstrate the possibly observed flavor ratio if heavier neutrino mass eigenstates can decay to lighter one. Since the cross section of high energy neutrinos interacting with matter is very small, the detection of neutrinos are very difficult. Most of experiments use the Earth as the target for neutrino to interact with it. In chapter 4, we build a Monte-Carlo program to simulate the neutrino interacting with the Earth. The charged current interaction of a neutrino produces the lepton and hadrons. If the lepton is muon or tau and generated inside the Earth, it may penetrate the Earth and decay to showers. The experiment can observe those showers to estimate the energy of the original neutrino. In chapter 5, we use CORSIKA to simulate the tau shower with different energy and calculate the electric field of synchrotron radiation generated by this shower. We estimate the energy of original neutrino by measuring the signal of synchrotron radiations. In chapter 6, we design a experiment in laboratory to measure the development of shower and compare the data with GEANT4 simulation.



## Chapter 2

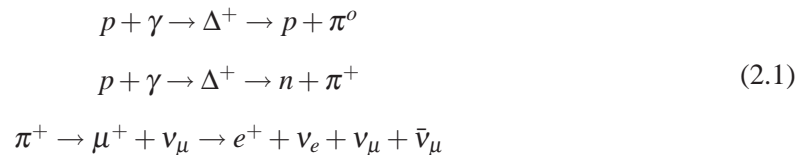
# Neutrino Flavor Ratio at the Astrophysical Source

Due to neutrino oscillations, the neutrino flavor ratio at the astrophysical source could be quite different from that observed on the Earth. This chapter discusses the reconstruction of neutrino flavor ratios at the astrophysical source.

### 2.1 Sources of Ultra-high Energetic Neutrinos

#### 2.1.1 AGN (Active Galactic Nucleus) Neutrinos

Active galactic nuclei (AGN) are the most luminous astrophysical objects in the sky [1]. AGN have two jets in opposite directions and perpendicular to the accretion disc of AGN. The jets accelerate the particles to extremely high energies by Fermi acceleration. The interacting chain between high energy protons and gamma rays for generating the pions via  $\Delta^+$  resonance is



If the muon decays without losing too much of its energy, the energies of neutrinos produced by the muon decay are close to the energy of neutrinos produced by from  $\pi^+$  decay . In this

chapter, we do not distinguish between neutrino and anti-neutrino. Hence this chain leads to the neutrino flavor ratio  $\phi_0(\nu_e) : \phi_0(\nu_\mu) : \phi_0(\nu_\tau) = 1 : 2 : 0$ , where  $\phi_0(\nu_\alpha)$  is the sum of  $\nu_\alpha$  and  $\bar{\nu}_\alpha$  fluxes. Since these neutrinos are produced by the decay of charged pion, such a source referred to as the pion source. In the case that the muon loses a huge part of its energy by interacting with the strong field [2] or matter [3], the energies of neutrinos produced by the muon decay are much lower than the energy of neutrino produced by pion decay. Hence this chain leads to the neutrino flavor ratio  $\phi_0(\nu_e) : \phi_0(\nu_\mu) : \phi_0(\nu_\tau) = 0 : 1 : 0$ , which is referred to as muon-damped source. Fig. 2.1.2 shows the neutrino spectrum from AGN.

### 2.1.2 GZK ( Greisen-Zetsepin-Kuzmin ) Neutrinos

The distribution of ultra high energy cosmic ray is isotropic and homogeneous. The major composition of cosmic ray are protons and nuclei. The ultra high energy proton,  $E_p > 10^{19}$  eV, has a possibility of interacting with the 2.7 K microwave background radiation during its propagation [4, 5]. In this interaction, proton and microwave background photon collide into the resonance state  $\Delta^+$ , which decays to neutron and pion. Finally, the pion decays to neutrinos. The chain of interactions and decays is the same as Eq. (2.1) in Sec.2.1.1. The GZK effect leads to a cutoff of the cosmic ray spectrum around  $10^{20}$  eV. The energy of neutrinos produced in this decay chain is around  $10^{17}$  to  $10^{18}$  eV. Fig. 2.1.2 shows the GZK tau neutrino spectrum [6].

## 2.2 Pontecorvo-Maki-Nakagawa-Sakata Mixing Matrix and Flavor Transition Probability Matrix

In neutrino oscillation theory, the relationship between neutrino mass eigenstates  $|\nu_i\rangle$  and neutrino flavor eigenstates  $|\nu_\alpha\rangle$  are described by Pontecorvo-Maki-Nakagawa-Sakata mixing matrix  $U$  (PMNS matrix)[7, 8]:

$$|\nu_\alpha\rangle = \sum_{i=1}^3 U_{\alpha i} |\nu_i\rangle, \quad (2.2)$$

where  $U$  is formed by three mixing angles  $\theta_{ij}$  and the  $CP$  violation phase  $\delta$ .  $U$  is written as

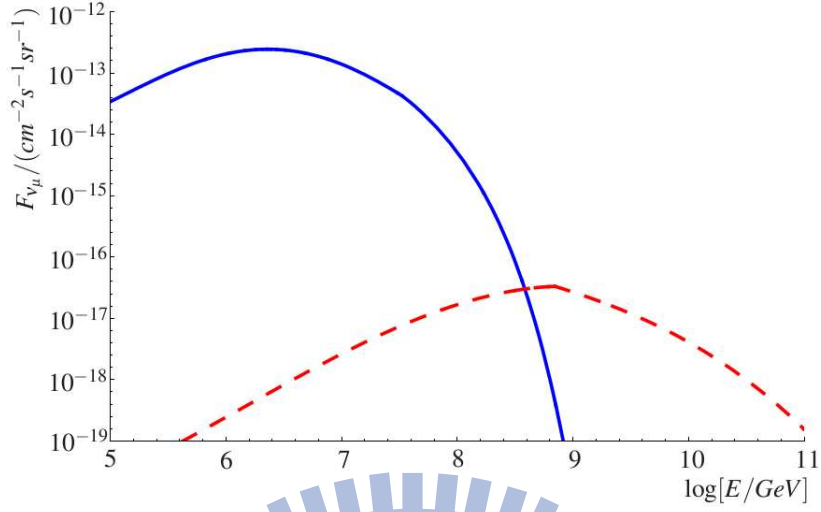


Figure 2.1: The spectrum of AGN [1] and GZK [6] muon neutrino flux. The blue solid line shows the muon neutrino spectrum from AGN source. The red dashed line shows the muon neutrino spectrum from GZK source.

$$\begin{aligned}
 U &= \begin{pmatrix} 1 & 0 & 0 \\ 0 & \cos \theta_{23} & \sin \theta_{23} \\ 0 & -\sin \theta_{23} & \cos \theta_{23} \end{pmatrix} \begin{pmatrix} \cos \theta_{13} & 0 & \sin \theta_{13} e^{-i\delta} \\ 0 & 1 & 0 \\ -\sin \theta_{13} e^{i\delta} & 0 & \cos \theta_{13} \end{pmatrix} \begin{pmatrix} \cos \theta_{12} & \sin \theta_{12} & 0 \\ -\sin \theta_{12} & \cos \theta_{12} & 0 \\ 0 & 0 & 1 \end{pmatrix} \\
 &= \begin{pmatrix} \cos \theta_{12} \cos \theta_{13} & \sin \theta_{12} \cos \theta_{13} & \sin \theta_{13} e^{-i\delta} \\ -\sin \theta_{12} \cos \theta_{23} - \cos \theta_{12} \sin \theta_{23} \sin \theta_{13} e^{i\delta} & \cos \theta_{12} \cos \theta_{23} - \sin \theta_{12} \sin \theta_{23} \sin \theta_{13} e^{i\delta} & \sin \theta_{23} \cos \theta_{13} \\ \sin \theta_{12} \cos \theta_{23} - \cos \theta_{12} \cos \theta_{23} \sin \theta_{13} e^{i\delta} & -\cos \theta_{12} \sin \theta_{23} - \sin \theta_{12} \cos \theta_{23} \sin \theta_{13} e^{i\delta} & \cos \theta_{23} \cos \theta_{13} \end{pmatrix}. \quad (2.3)
 \end{aligned}$$

The time-dependent mass eigenstates  $|v_i\rangle$  can be written as

$$|v_i(x, t)\rangle = e^{-iEt} |v_i(x, 0)\rangle = e^{-iEt} e^{ipx} |v_i\rangle.$$

The transition amplitude for flavor eigenstates  $|v_\alpha\rangle$  to flavor eigenstates  $|v_\beta\rangle$  is

$$\langle v_\beta | v_\alpha \rangle = \langle v_j | U_{\beta j}^* U_{\alpha i} e^{-iEt} e^{ipx} |v_i\rangle = \sum_i U_{\beta i}^* U_{\alpha i} e^{-iEt} e^{ipx} = \sum_i U_{\beta i}^* U_{\alpha i} e^{-i\frac{m_i L}{2E}},$$



where  $L$  is the propagation distance of neutrino,  $E$  and  $m_i$  correspond the energy and mass of as the neutrino. Then the time-dependent transition probabilities for flavor  $\beta$  to flavor  $\alpha$  can be written as

$$|\langle \nu_\alpha | \nu_\beta \rangle|^2 = \delta_{\alpha\beta} - 4 \sum \text{Re}(U_{\alpha i} U_{\beta j}^* U_{\alpha i}^* U_{\beta j}) \sin^2 \left( \frac{\Delta m_{ij}^2 L}{4E} \right) + 4 \sum \text{Im}(U_{\alpha i} U_{\beta j}^* U_{\alpha i}^* U_{\beta j}) \sin \left( \frac{\Delta m_{ij}^2 L}{4E} \right) \cos \left( \frac{\Delta m_{ij}^2 L}{4E} \right), \quad (2.4)$$

where  $\Delta m_{ij}^2 \equiv m_i^2 - m_j^2$ . In the limit of large neutrino propagation distance, the neutrino oscillation probability only depend on the mixing angles  $\theta_{ij}$  and  $CP$  phase. In this case, the transition probability for flavor  $\beta$  to flavor  $\alpha$  can be expressed in terms of unitary matrix  $U$  purely:

$$P_{\alpha\beta} = \sum_{i=1}^3 |U_{\alpha i}|^2 |U_{\beta i}|^2. \quad (2.5)$$

Hence the neutrino flux at the astrophysical site and that detected on the Earth is related by

$$\begin{pmatrix} \phi(\nu_e) \\ \phi(\nu_\mu) \\ \phi(\nu_\tau) \end{pmatrix} = \begin{pmatrix} P_{ee} & P_{e\mu} & P_{e\tau} \\ P_{\mu e} & P_{\mu\mu} & P_{\mu\tau} \\ P_{\tau e} & P_{\tau\mu} & P_{\tau\tau} \end{pmatrix} \begin{pmatrix} \phi_0(\nu_e) \\ \phi_0(\nu_\mu) \\ \phi_0(\nu_\tau) \end{pmatrix} \equiv P \begin{pmatrix} \phi_0(\nu_e) \\ \phi_0(\nu_\mu) \\ \phi_0(\nu_\tau) \end{pmatrix}, \quad (2.6)$$

where  $\phi(\nu_\alpha)$  is the neutrino flux measured on the Earth while  $\phi_0(\nu_\alpha)$  is the neutrino flux at the source, and the matrix element  $P_{\alpha\beta}$  is the probability for the oscillation  $\nu_\beta \rightarrow \nu_\alpha$ . The exact analytic form of the probability matrix  $P$  is given by

$$\begin{aligned}
P_{ee} &= \left(1 - \frac{1}{2}\omega\right) (1 - D^2)^2 + D^4, \\
P_{e\mu} &= \frac{1}{4}(1 - D^2) \left[ \omega(1 + \Delta) + (4 - \omega)(1 - \Delta)D^2 + 2\sqrt{\omega(1 - \omega)(1 - \Delta^2)}D \cos \delta \right], \\
P_{e\tau} &= \frac{1}{4}(1 - D^2) \left[ \omega(1 - \Delta) + (4 - \omega)(1 + \Delta)D^2 - 2\sqrt{\omega(1 - \omega)(1 - \Delta^2)}D \cos \delta \right], \\
P_{\mu\mu} &= \frac{1}{2} [(1 + \Delta^2) - (1 - \Delta)^2 D^2 (1 - D^2)] \\
&\quad - \frac{1}{8}\omega [(1 + \Delta)^2 + (1 - \Delta)^2 D^4 - (1 - \Delta^2)D^2 (2 + 4 \cos^2 \delta)] \\
&\quad - \frac{1}{2}\sqrt{\omega(1 - \omega)(1 - \Delta^2)} [(1 + \Delta) - (1 - \Delta)D^2] D \cos \delta, \\
P_{\mu\tau} &= \frac{1}{2}(1 - \Delta^2)(1 - D^2 + D^4) \\
&\quad - \frac{1}{8}\omega [(1 - \Delta^2)(1 + 4D^2 \cos^2 \delta + D^4) - 2(1 + \Delta^2)D^2] \\
&\quad + \frac{1}{2}\sqrt{\omega(1 - \omega)(1 - \Delta^2)}\Delta(1 + D^2)D \cos \delta, \\
P_{\tau\tau} &= \frac{1}{2} [(1 + \Delta^2) - (1 + \Delta)^2 D^2 (1 - D^2)] \\
&\quad - \frac{1}{8}\omega [(1 - \Delta)^2 + (1 + \Delta)^2 D^4 - (1 - \Delta^2)D^2 (2 + 4 \cos^2 \delta)] \\
&\quad + \frac{1}{2}\sqrt{\omega(1 - \omega)(1 - \Delta^2)} [(1 - \Delta) - (1 + \Delta)D^2] D \cos \delta, \tag{2.7}
\end{aligned}$$

with  $\omega \equiv \sin^2 2\theta_{12}$ ,  $\Delta \equiv \cos 2\theta_{23}$ ,  $D \equiv \sin \theta_{13}$ , and  $\delta$  the CP phase.

If we take the best-fit values of neutrino mixing angles from parameter set I in Tab. 2.3, the neutrino flavor ratios observed on the Earth from the pion source and muon-damped source after oscillation are shown in Fig. 2.2(a). Considering the uncertainties of mixing angle measurement, the flavors ratios observed on the Earth are shown in Fig. 2.2(b).

It is seen that  $P_{e\mu} = P_{e\tau}$  and  $P_{\mu\mu} = P_{\mu\tau} = P_{\tau\tau}$  in the limit  $\Delta = 0 = D$ , *i.e.*,  $\theta_{23} = \pi/4$  and  $\theta_{13} = 0$ . In this case, the probability matrix  $P$  is singular. In general, this singularity is only slightly broken since both  $\Delta$  and  $D$  are expected to be small. For  $\Delta = 0 = D$ , the eigenvectors of the matrix  $P$  are

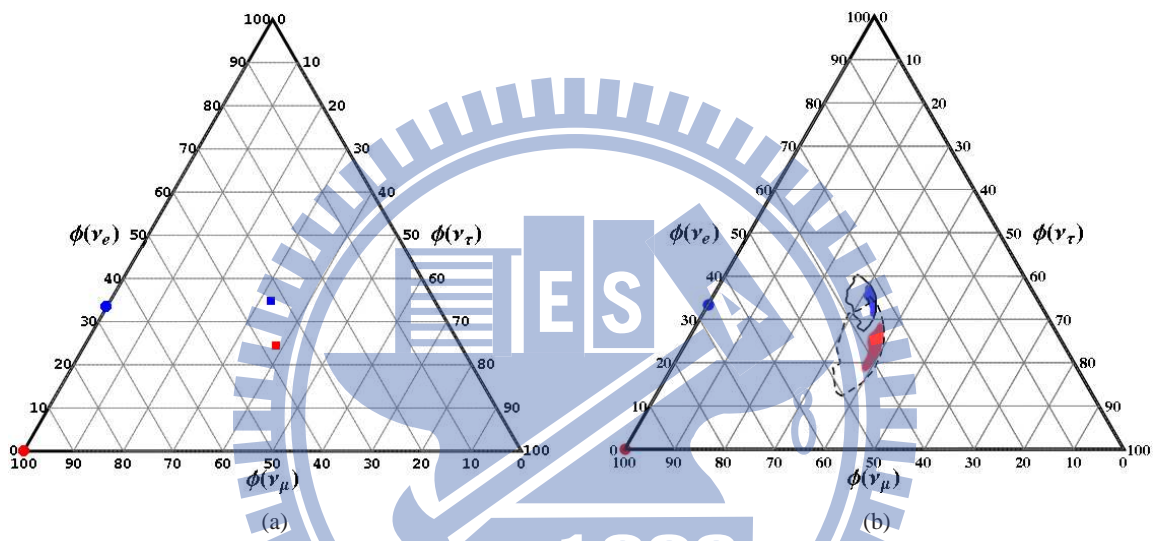


Figure 2.2: The ranges for the neutrino flavor ratios on the Earth resulting from standard neutrino oscillation. The numbers on each side of the triangle denote the flux fraction of a specific flavor of neutrino. The blue point marks the pion source  $\phi_0(\nu_e) : \phi_0(\nu_\mu) : \phi_0(\nu_\tau) = 1/3 : 2/3 : 0$  and the red point marks the muon-damped source  $\phi_0(\nu_e) : \phi_0(\nu_\mu) : \phi_0(\nu_\tau) = 0 : 1 : 0$ . In panel (a), the red and blue squares mark the corresponding neutrino flavor ratios observed on the Earth. In panel (b), we introduce uncertainties of neutrino mixing angles in the probability matrix. The red and dashed line denote neutrino flavor ratios observed on the Earth from muon-damped source in  $1\sigma$  and  $3\sigma$  ranges of neutrino mixing angles respectively. The blue and solid line denote neutrino flavor ratios observed on the Earth from pion source in  $1\sigma$  and  $3\sigma$  ranges of neutrino mixing angles respectively

$$V^a = \frac{1}{\sqrt{3}} \begin{pmatrix} 1 \\ 1 \\ 1 \end{pmatrix}, V^b = \frac{1}{\sqrt{2}} \begin{pmatrix} 0 \\ -1 \\ 1 \end{pmatrix}, V^c = \frac{1}{\sqrt{6}} \begin{pmatrix} -2 \\ 1 \\ 1 \end{pmatrix}, \quad (2.8)$$

with the corresponding eigenvalues

$$\lambda_a = 1, \lambda_b = 0, \lambda_c = \frac{1}{4}(4 - 3\omega), \quad (2.9)$$

where  $\omega = \sin^2 2\theta_{12}$ . Therefore, those initial flavor ratios that differ from one another by a multiple of  $V^b$  shall oscillate into the same flavor ratio on the Earth. To illustrate this explicitly, we write the initial flux  $\Phi_0$  at the astrophysical source as

$$\Phi_0 = \begin{pmatrix} 1 \\ 0 \\ 0 \end{pmatrix} - \frac{\sqrt{2}}{2} (\phi_0(\nu_\mu) - \phi_0(\nu_\tau)) V^b + \frac{\sqrt{6}}{2} (\phi_0(\nu_\mu) + \phi_0(\nu_\tau)) V^c, \quad (2.10)$$

where we have imposed the normalization condition  $\phi_0(\nu_e) + \phi_0(\nu_\mu) + \phi_0(\nu_\tau) = 1$ . This normalization convention will be adopted throughout this thesis. The first term on the right-hand side (RHS) of Eq. (2.10) can be expressed as  $(\sqrt{3}V^a - \sqrt{6}V^c)/3$ . Hence the neutrino flux measured by the terrestrial neutrino telescope is

$$\Phi = P\phi_0 = \frac{\sqrt{3}}{3} V^a - \frac{\sqrt{6}}{3} \left(1 - \frac{3}{4}\omega\right) V^c + \frac{\sqrt{6}\lambda_c}{2} (\phi_0(\nu_\mu) + \phi_0(\nu_\tau)) V^c. \quad (2.11)$$

It is seen that the vector  $V^b$ , with a coefficient proportional to  $\phi_0(\nu_\mu) - \phi_0(\nu_\tau)$ , does not appear in the terrestrially measured flux  $\Phi$ . Hence the terrestrial measurement can not constrain  $\phi_0(\nu_\mu) - \phi_0(\nu_\tau)$  in this case.

The above degeneracy is lifted by either a non-vanishing  $\theta_{13}$  ( $D \neq 0$ ) or a deviation of  $\theta_{23}$  from  $\pi/4$  ( $\Delta \neq 0$ ). To simplify our discussions, let us take  $D = 0$  and  $\Delta \neq 0$ . One can show that the flux combination  $(1 + 4\omega\Delta/(4 - 3\omega)) \phi_0(\nu_\mu) - (1 - 2\omega\Delta/(4 - 3\omega)) \phi_0(\nu_\tau)$  remains

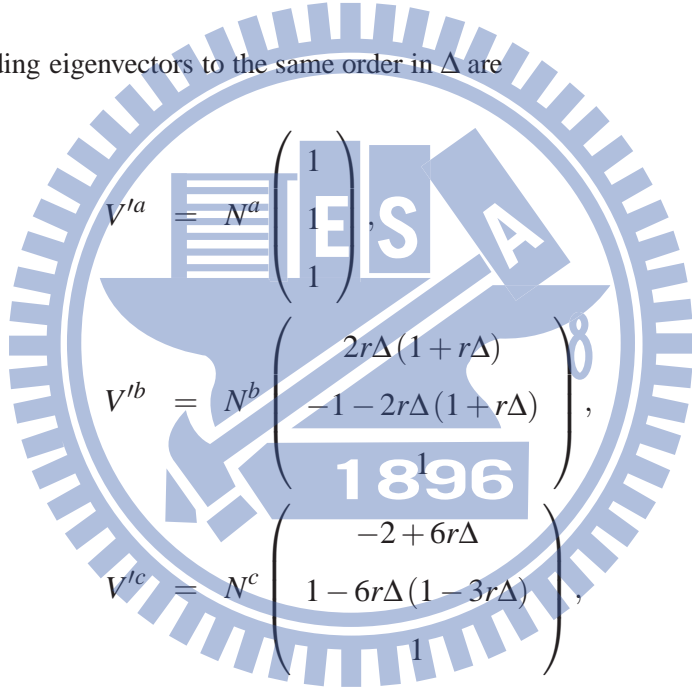
poorly constrained due to the suppression of  $\det P$ . To demonstrate this, we observe that

$$P = \frac{1}{8} \begin{pmatrix} 8 - 4\omega & 2(1 + \Delta)\omega & 2(1 - \Delta)\omega \\ 2(1 + \Delta)\omega & (4 - \omega)(1 + \Delta^2) - 2\Delta\omega & (4 - \omega)(1 - \Delta^2) \\ 2(1 - \Delta)\omega & (4 - \omega)(1 - \Delta^2) & (4 - \omega)(1 + \Delta^2) + 2\Delta\omega \end{pmatrix} \quad (2.12)$$

for  $D = 0$  and  $\Delta \neq 0$ . The eigenvalues of  $P$  expanded to the second order in  $\Delta$  are given by

$$\lambda'_a = 1, \lambda'_b = \left( \frac{4 - 4\omega}{4 - 3\omega} \right) \Delta^2, \lambda'_c = \frac{1}{4}(4 - 3\omega) + \frac{3\omega^2 \Delta^2}{4(4 - 3\omega)}, \quad (2.13)$$

and the corresponding eigenvectors to the same order in  $\Delta$  are



$$\begin{aligned} V^{la} &= N^a \begin{pmatrix} 1 \\ 1 \\ 1 \end{pmatrix}, \\ V^{lb} &= N^b \begin{pmatrix} 2r\Delta(1 + r\Delta) \\ -1 - 2r\Delta(1 + r\Delta) \\ 1 \end{pmatrix}, \\ V^{lc} &= N^c \begin{pmatrix} -2 + 6r\Delta \\ 1 - 6r\Delta(1 - 3r\Delta) \\ 1 \end{pmatrix}, \end{aligned} \quad (2.14)$$

with  $r = \omega/(4 - 3\omega)$  and  $N^{a,b,c}$  the appropriate normalization factors. It is interesting to note that the corrections to the eigenvectors of  $P$  begin at  $\mathcal{O}(\Delta)$  while the corrections to the corresponding eigenvalues begin at  $\mathcal{O}(\Delta^2)$ . With the above eigenvectors, we write the source neutrino flux as

$$\begin{aligned} \Phi_0 &= N^a V^{la} - [(1 + 4r\Delta)\phi_0(v_\mu) - (1 - 2r\Delta)\phi_0(v_\tau) - 2r\Delta] N^b V^{lb} \\ &+ 3 \left[ (1 - 4r\Delta)\phi_0(v_\mu) + (1 - 2r\Delta)\phi_0(v_\tau) - \frac{2}{3}(1 - 3r\Delta) \right] N^c V^{lc}. \end{aligned} \quad (2.15)$$

particle	major processes	signal type	symbol in Fig. 2.3
e	EM shower	shower	A
$\mu$	energy loss	track	B
$\tau(E_\nu < 3.3 \text{ PeV})$	CC int. and $\tau$ -decay	shower	C
$\tau(3.3 \text{ PeV} < E_\nu < 33 \text{ PeV})$	CC int. and $\tau$ -decay	2 separate showers	D (double-bang event)
$\tau(E_\nu > 3.3 \text{ PeV})$	energy loss and decay	track and shower	E (lollipop event)
$\tau(E_\nu > 3.3 \text{ PeV})$	CC int. and energy loss	shower and track	F (inverted lollipop event)
$\tau(E_\nu > 33 \text{ PeV})$	energy loss	track	G
X	hadron shower	shower	

Table 2.1: Different types of neutrino induced events.

It is easy to show that the measured flux  $P\Phi_0$  depends on  $V^{lb}$  through the combination  $-B\lambda'_b N^b V^{lb}$  with

$$B = [(1 + 4r\Delta)\phi_0(\nu_\mu) - (1 - 2r\Delta)\phi_0(\nu_\tau) - 2r\Delta]. \quad (2.16)$$

Clearly the flux combination  $(1 + 4r\Delta)\phi_0(\nu_\mu) - (1 - 2r\Delta)\phi_0(\nu_\tau)$  is poorly constrained due to the smallness of  $\lambda'_b$ , of the order  $\Delta^2$ .

### 2.3 Observed Neutrino Events in Detector

Neutrinos must interact with matters to produce observable signals. The major channel for such interactions is the charged-current (CC) interaction,  $\nu_l + N \longrightarrow l + X$ , where  $l$  is the lepton associated with  $\nu_l$  and  $X$  denotes the hadronic states. The sub-dominant channel is the neutral-current interaction (NC),  $\nu_l + N \longrightarrow \nu_l + X$ . The detail of CC and NC interaction mechanisms are discussed in section 4.2.3. In Fig. 2.3 and Table 2.1, we summarize different types of neutrino induced events and their detectable energy ranges.

Type-A event in Fig. 2.3 is an electron production through  $\nu_e$  CC interaction. The electron has a large interaction cross section with the medium and produces a shower within a short distance after its production. A similar shower signature can be produced by hadrons resulting from NC interactions of all neutrino flavors. Type-B event is a muon produced by  $\nu_\mu$  CC interaction. Contrary to the electron, a muon can travel a long distance in the medium before it loses all its energy or decay. The muon range in ice is more than 10 km for  $E_\nu = 1 \text{ PeV}$  ( $10^{15} \text{ eV}$ ). Hence,

at this energy or higher, there is hardly any decay of muon occurring within the fiducial volume of the detector, which is about a few  $\text{km}^3$ . A muon does, however, lose a small fraction of its energy and emits dim lights so that only those optical detectors which are near to the muon track can be triggered. As a result, a muon produces a track-like signal.

The  $\nu_\tau$ -induced events are listed as types C-G where the tau lepton produced by  $\nu_\tau$  CC interaction behaves differently at different energies for a fixed detector design. For a neutrino telescope such as IceCube [9], the distance between each string of optical detectors is 125 m, which corresponds to the decay length of a 2.5 PeV tau lepton. Such a tau lepton could be produced by the CC interaction of a  $\nu_\tau$  with  $E_\nu = 3.3$  PeV. Therefore, for a  $\nu_\tau$  with an energy significantly smaller than this, the separation between the first hadronic shower produced by CC interaction and the second shower produced by the tau-lepton decay is too small to be resolved. Such an event is classified as type C. For  $E_\nu > 3.3$  PeV, one can resolve the above double-bang event (classified as type D) until the separation of two showers exceeds the effective size of the detector. Such a size is estimated to be the sum of IceCube dimension ( $\approx 1$  km) and two extinction lengths of optical photons in ice ( $\approx 250$  m), which corresponds to the decay length of a tau lepton with  $E_\tau = 25$  PeV. The average energy of  $\nu_\tau$  capable of producing such a tau lepton is around 33.3 PeV. Hence the configuration of IceCube detector determines the observable energy range for the double bang event to be  $3.3 \text{ PeV} < E_\nu < 33.3 \text{ PeV}$  [10]. For an under-sea experiment, such as KM3NeT [11], the observable energy range for the double bang event is similar.

Type-E event is referred to as the lollipop event. In such an event, a high energy tau lepton enters the detector and decays within it, producing a track signal followed by a shower. The probability for observing a lollipop event increases with the neutrino energy, and it is about  $5 \times 10^{-4}$  for  $E_\nu = 1$  EeV [12]. Type-F event is the inverted lollipop which consists of a hadronic shower from  $\nu_\tau$  CC interaction and a subsequent tau-lepton track. Both muons and tau leptons produce inverted lollipop events and it is not easy to separate these two types of events. Finally, type-G event is a through-going tau-lepton track which is produced by  $\nu_\tau$  CC interaction with  $E_\nu > 33.3$  PeV.

*Flux ratio parameter for  $E_\nu < 3.3$  PeV.*— In this energy range, type-A and type-C events are not distinguishable since the two showers in the latter event can not be resolved. Hence one

Condition I : $E_\nu < 33$ PeV	Condition II : $E_\nu > 33$ PeV
$R^I = \phi(\nu_\mu)/(\phi(\nu_e) + \phi(\nu_\tau))$	$R^{II} = \phi(\nu_e)/(\phi(\nu_\mu) + \phi(\nu_\tau))$
$S^I = \phi(\nu_e)/\phi(\nu_\tau)$	$S^{II} = \phi(\nu_\mu)/\phi(\nu_\tau)$

Table 2.2: The definitions of  $R$  and  $S$  at different energy ranges.

can only measure the ratio  $N_{\text{track}}/N_{\text{shower}}$  where  $N_{\text{shower}}$  is the total event number for electron showers, tau-lepton showers and the hadronic showers from NC interactions. In IceCube, this ratio can be measured in a good precision, which is useful for deducing the flux ratio  $R^I = \phi(\nu_\mu)/(\phi(\nu_e) + \phi(\nu_\tau))$  [13].

*Flux ratio parameters for  $3.3$  PeV  $< E_\nu < 33.3$  PeV.*— In this energy range, one can detect the type-D and type-E  $\nu_\tau$  events (double bang and lollipop). Hence it is also possible to measure the flux ratio  $S^I \equiv \phi(\nu_e)/\phi(\nu_\tau)$  in addition to  $R^I$  [14]. However, the double bang and lollipop events are both rare so that the error associated with  $S^I$  is large. We demonstrated that a large number of events is necessary for lowering down the errors of  $R^I$  and  $S^I$  to the point that one can distinguish the pion source from the muon-damped source [15].

*Flux ratio parameter for  $E_\nu > 33.3$  PeV.*— In this high energy regime, the tau-lepton range becomes long enough so that a tau lepton could pass through the detector fiducial volume without decaying. In this case, the tau-lepton loses its energy just like a muon does and the signal appears like a track event [16]. Thus, from an experimental point of view, one should classify such a signature as a track event (type G). In this energy range, there are also type-E and type-F events where tau leptons also behave like tracks. We therefore define a new flavor ratio parameter  $R^{II} = \phi(\nu_e)/(\phi(\nu_\mu) + \phi(\nu_\tau))$  since the electron shower can be easily separated from the muon and tau-lepton tracks. It is however more challenging to distinguish the tau-lepton track from the muon track so that the second flux ratio parameter  $S^{II} = \phi(\nu_\mu)/\phi(\nu_\tau)$  can not be measured as accurately as  $R^{II}$ . Table 2.2 present the appropriate flux ratio parameters for high energy are low energy respectively.



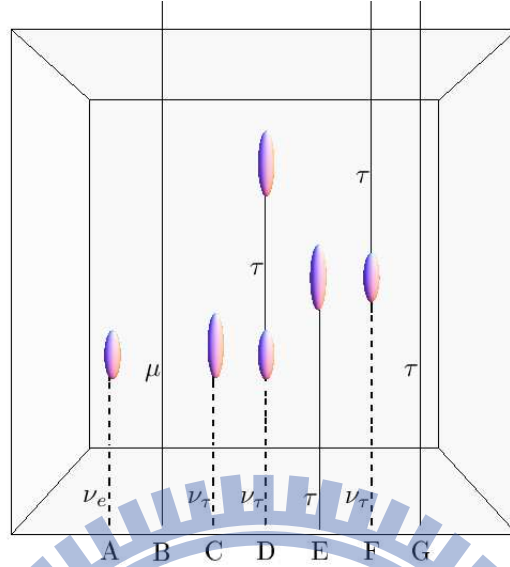


Figure 2.3: Different types of neutrino-induced events. Dashed lines and solid lines correspond to paths of neutrinos and leptons respectively. The ellipsoids are showers. The detectable energy range for each type of event is listed in Table 2.1.

## 2.4 Reconstructing Source Flavor Ratios at Low Energies

Most of previous studies concerning  $R^I$  and  $S^I$  assume a good knowledge of neutrino flavor ratio at the source and explore possible flavor ratios to be observed on the Earth [12, 13]. We take a reversed approach to identify source flavor ratio from the observed flavor ratio on the Earth.

Given a precision on measuring  $R^I$ ,  $\Delta R^I/R^I$ , we estimate  $\Delta S^I/S^I$  with two approaches. The first approach assumes that both  $\Delta R^I$  and  $\Delta S^I$  are dominated by the statistical errors. In this case, one has

$$\left(\frac{\Delta S^I}{S^I}\right) = \frac{1+S^I}{\sqrt{S^I}} \sqrt{\frac{R^I}{1+R^I}} \left(\frac{\Delta R^I}{R^I}\right), \quad (2.17)$$

Using values of  $R^I$  and  $S^I$  from Table 2.4, we obtain  $\Delta S^I/S^I = (1.1 - 1.2)(\Delta R^I/R^I)$  from the pion source and  $\Delta S^I/S^I = (1.1 - 1.4)(\Delta R^I/R^I)$  from the muon-damped source. The second approach takes into account the specific complications for identifying tau neutrinos. Since tau lepton decays before it loses a significant fraction of its energy, tau neutrino is identified by the so-called double-bang or lollipop events [10, 12, 19]. In IceCube or other detector with a comparable

size, double-bang events are observable only in a narrow energy range between 2 PeV and 20 PeV [10, 19] while the probability for observing a lollipop event, though increasing with the neutrino energy, is still less than  $10^{-3}$  for  $E_\nu = 1$  EeV [12]. In view of these, we do not correlate  $\Delta S^I/S^I$  with  $\Delta R^I/R^I$  in the second approach. Rather we fix  $\Delta S^I/S^I$  while vary  $\Delta R^I/R^I$  for achieving the goal of distinguishing astrophysical neutrino sources. The results of both approaches will be presented. Before presenting the details of our analysis, we point out that the decays  $\tau \rightarrow \nu_\tau \mu \bar{\nu}_\mu$  and  $\tau \rightarrow \nu_\tau \mu \bar{\nu}_\mu$ , each with a 18% branching ratio, produce extra muon events or secondary  $\nu_e$  and  $\nu_\mu$  [12, 20]. Cares are needed to separate these events from those of primary  $\nu_e$  and  $\nu_\mu$  or muons produced by the charged current interaction.

The fitting to the neutrino flavor ratios at the source is facilitated through

$$\chi^2 = \left( \frac{R_{\text{th}}^I - R_{\text{exp}}^I}{\sigma_{R_{\text{exp}}^I}} \right)^2 + \left( \frac{S_{\text{th}}^I - S_{\text{exp}}^I}{\sigma_{S_{\text{exp}}^I}} \right)^2 + \sum_{jk=12,23,13} \left( \frac{s_{jk}^2 - (s_{jk}^2)_{\text{best fit}}}{\sigma_{s_{jk}^2}} \right)^2, \quad (2.18)$$

with  $\sigma_{R_{\text{exp}}^I} = (\Delta R^I/R^I)R_{\text{exp}}^I$ ,  $\sigma_{S_{\text{exp}}^I} = (\Delta S^I/S^I)S_{\text{exp}}^I$ ,  $s_{jk}^2 \equiv \sin^2 \theta_{jk}$  and  $\sigma_{s_{jk}^2}$  the  $1\sigma$  range for  $s_{jk}^2$ . Here  $R_{\text{th}}^I$  and  $S_{\text{th}}^I$  are theoretical predicted values for  $R^I$  and  $S^I$  respectively while  $R_{\text{exp}}^I$  and  $S_{\text{exp}}^I$  are experimentally measured values. The values for  $R_{\text{exp}}^I$  and  $S_{\text{exp}}^I$  are listed in Table 2.4, which are generated from input true values of neutrino flavor ratios at the source and input true values of neutrino mixing parameters. In  $R_{\text{th}}^I$  and  $S_{\text{th}}^I$ , the variables  $s_{jk}^2$  can vary between 0 and 1 while  $\cos \delta$  can vary between  $-1$  and  $1$ . We note that similar  $\chi^2$  functions have been used for fitting the CP violation phase and the mixing angle  $\theta_{23}$  respectively [17, 21], assuming the source flavor ratio is known. In our analysis, we scan all possible neutrino flavor ratios at the source that give rise to a specific  $\chi^2$  value. Since we have taken  $R_{\text{exp}}^I$  and  $S_{\text{exp}}^I$  as those generated by input true values of initial neutrino flavor ratios and neutrino mixing parameters, we have  $(\chi^2)_{\text{min}}=0$  occurring at these input true values of parameters. Hence the boundaries for  $1\sigma$  and  $3\sigma$  ranges of initial neutrino flavor ratios are given by  $\Delta\chi^2 = 2.3$  and  $\Delta\chi^2 = 11.8$  respectively where  $\Delta\chi^2 \equiv \chi^2 - (\chi^2)_{\text{min}} = \chi^2$  in our analysis.

Parameter set	$\sin^2 \theta_{12}$	$\sin^2 \theta_{23}$	$\sin^2 \theta_{13}$	$\delta$
1	$0.32^{+0.02}_{-0.02}$	$0.45^{+0.09}_{-0.06}$	$< 0.019$	0
2	$0.32^{+0.02}_{-0.02}$	$0.55^{+0.09}_{-0.06}$	$< 0.019$	0
3a	$0.32^{+0.02}_{-0.02}$	$0.45^{+0.09}_{-0.06}$	$0.016 \pm 0.010$	0
3b	$0.32^{+0.02}_{-0.02}$	$0.45^{+0.09}_{-0.06}$	$0.016 \pm 0.010$	$\pi/2$
3c	$0.32^{+0.02}_{-0.02}$	$0.45^{+0.09}_{-0.06}$	$0.016 \pm 0.010$	$\pi$

Table 2.3: Parameter sets chosen for our analysis

Parameter set	$\Phi_\mu = P\Phi_{0,\mu}$	$R^I$	$S^I$	$\Phi_\pi = P\Phi_{0,\pi}$	$R^I$	$S^I$
1	(0.24, 0.37, 0.39)	0.62	0.60	(0.35, 0.33, 0.32)	0.49	1.08
2	(0.19, 0.42, 0.39)	0.71	0.51	(0.32, 0.34, 0.34)	0.52	0.94
3a	(0.27, 0.35, 0.38)	0.55	0.71	(0.36, 0.33, 0.31)	0.48	1.15
3b	(0.25, 0.37, 0.38)	0.59	0.64	(0.35, 0.33, 0.32)	0.49	1.07
3c	(0.23, 0.40, 0.37)	0.67	0.60	(0.33, 0.34, 0.33)	0.52	1.02

Table 2.4: True values of neutrino flavor ratios on the Earth

#### 2.4.1 The Reconstruction of Initial Neutrino Flavor Ratio by Measuring $R^I$ Alone

It is instructive to see how well one can determine the initial neutrino flavor ratio by measuring  $R^I$  alone. We perform such an analysis by neglecting the second term on the RHS of Eq. (2.18). The  $1\sigma$  and  $3\sigma$  ranges for the reconstructed flavor ratios at the source are shown in Fig. 2.4. For an input muon-damped source, it is seen that, with  $\Delta R^I/R^I = 10\%$ , the reconstructed  $3\sigma$  range of the neutrino flavor ratio almost covers the entire physical region. For an input pion source with  $\Delta R^I/R^I = 10\%$ . We again find that all possible initial neutrino flavor ratios are allowed at the  $3\sigma$  level. Clearly it is desirable to measure both  $R^I$  and  $S^I$ .

#### 2.4.2 The Flavor Reconstruction with Measurements on Both $R$ and $S$

In this subsection, we perform a statistical analysis with respect to simultaneous measurements of  $R^I$  and  $S^I$ . The accuracy for the measurement on  $R^I$  is  $\Delta R^I/R^I = 10\%$ . Here we adopt the first approach for estimating  $\Delta S^I/S^I$  while present the second approach in the next subsection. With the first approach, we have  $\Delta S^I/S^I = (11 - 12)\%$  for the pion source and  $\Delta S^I/S^I = (11 - 14)\%$  for the muon-damped source.

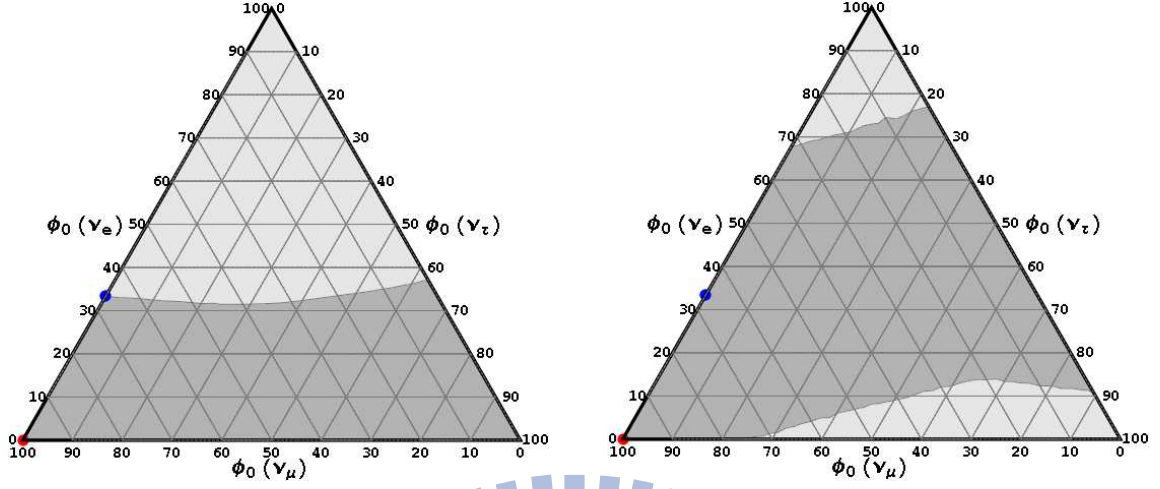


Figure 2.4: The reconstructed ranges for the neutrino flavor ratios at the source with  $\Delta R^I/R^I = 10\%$  only. The left and right panels are results with the muon-damped source and the pion source as the input true source respectively. The numbers on each side of the triangle denote the flux percentage of a specific flavor of neutrino. The red point marks the muon-damped source  $\Phi_{0,\mu} = (0, 1, 0)$  and the blue point marks the pion source  $\Phi_{0,\pi} = (1/3, 2/3, 0)$ . Gray and light gray areas respectively denote the  $1\sigma$  and  $3\sigma$  ranges for the reconstructed neutrino flavor ratios at the source. We choose parameter set 1 in Table 2.4 for this analysis.

#### 2.4.2.1 $(\sin^2 \theta_{13})_{\text{bestfit}} = 0$

We begin our analysis with the parameter set 1 and 2 where  $(\sin^2 \theta_{13})_{\text{bestfit}} = 0$  and  $(\sin^2 \theta_{23})_{\text{bestfit}} = 0.45$  and  $0.55$  respectively. Figs. 2.5 and 2.6 show the reconstructed neutrino flavor ratios for an input muon-damped source and an input pion source respectively. The reconstructed initial flavor ratios are seen to include the region with significant  $\nu_\tau$  fractions. It has been shown in Sec. 2.2 that the flux combination  $(1 + 4r\Delta)\phi_0(\nu_\mu) - (1 - 2r\Delta)\phi_0(\nu_\tau)$  is poorly constrained due to the smallness of eigenvalue  $\lambda_b^I$  associated with  $V^{Ib}$  (see Eq. (2.13) and (2.14)). This then leads to an extension in the reconstructed range of the initial neutrino flavor ratio along the  $V^{Ib}$  direction. In the limit  $\Delta \equiv \cos 2\theta_{23} = 0$ , *i.e.*,  $\sin^2 \theta_{23} = 0.5$ ,  $V^{Ib}$  reduces to  $V^b$  (see Eq. (2.8)) which is exactly parallel to the  $\nu_e$ -less side of the flavor-ratio triangle. The direction of  $V^{Ib}$  deviates slightly from that of  $V^b$  in opposite ways depending on the sign of  $\Delta$ . This is seen by comparing the left and right panels of both Fig. 2.5 and Fig. 2.6. Due to uncertainties of neutrino mixing parameters, we note that the boundaries for  $1\sigma$  and  $3\sigma$  regions are not straight lines. For an input muon-damped source, the pion source can be ruled out at the  $3\sigma$  level as shown in Fig. 2.5. However, the converse is not true as seen from Fig. 2.6.

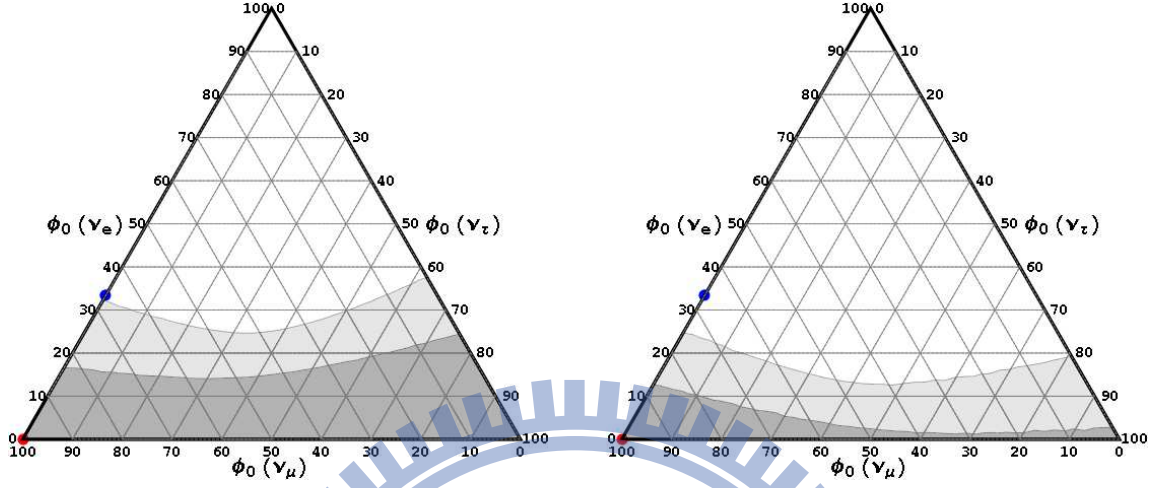


Figure 2.5: The reconstructed ranges for the neutrino flavor ratios for an input muon-damped source with  $\Delta R^I/R^I = 10\%$  and  $\Delta S^I/S^I$  related to the former by the Poisson statistics, E.q. (2.17). Gray and light gray areas in the left (right) panel denote the reconstructed  $1\sigma$  and  $3\sigma$  ranges with the parameter set 1 (2) in Table 2.4.

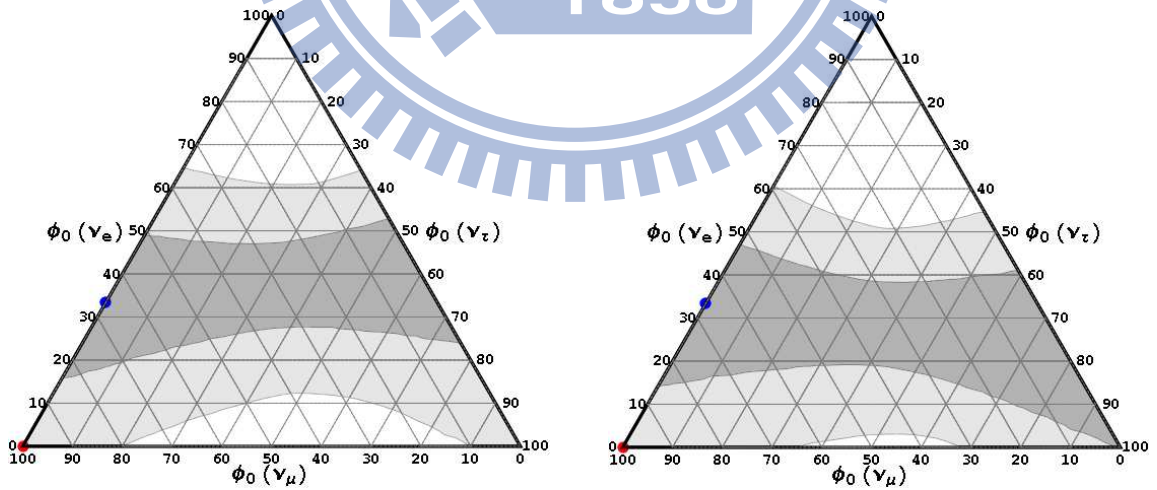


Figure 2.6: The reconstructed ranges for the neutrino flavor ratios for an input pion source with  $\Delta R^I/R^I = 10\%$  and  $\Delta S^I/S^I$  related to the former by the Poisson statistics, E.q. (2.17). Gray and light gray areas in the left (right) panel denote the reconstructed  $1\sigma$  and  $3\sigma$  ranges with the parameter set 1 (2) in Table 2.4.

#### 2.4.2.2 $(\sin^2 \theta_{13})_{\text{bestfit}} > 0$

A non-zero  $\theta_{13}$  introduces the CP phase contribution to every element of matrix  $P$ , except  $P_{ee}$ . We study the effect of CP phase  $\delta$  on the reconstruction of neutrino flavor ratio at the source. We choose parameter sets 3a, 3b and 3c for performing the statistical analysis. The results are shown in the right panels of Figs. 2.7 and 2.8. For comparisons, we also perform the analysis with  $\theta_{13}$  and  $\theta_{23}$  taken from the parameter set 1 and the input CP phase taken to be  $0$ ,  $\pi/2$  and  $\pi$  respectively. The results are shown in the left panels of Figs. 2.7 and 2.8.

Left panels of Figs. 2.7 and 2.8 indicate that the reconstructed ranges for initial neutrino flavor ratios are independent of the input CP phase for  $(\sin^2 \theta_{13})_{\text{bestfit}} = 0$ . The dependencies on the CP phase only appear in the right panels. For an input muon-damped source (see Fig. 2.7), the allowed  $1\sigma$  and  $3\sigma$  ranges for initial neutrino flavor ratios are the smallest (denoted by red curves) for  $\cos \delta = -1$ , *i.e.*,  $\delta = \pi$ . In this case, the pion source can be ruled out at the  $3\sigma$  level. The allowed ranges become the largest (denoted by gray areas) for  $\cos \delta = 1$ , *i.e.*,  $\delta = 0$ . For an input pion source with different CP phases, the allowed  $3\sigma$  ranges for the initial neutrino flavor ratio always cover the muon-damped source.

#### 2.4.3 Critical Accuracies Needed for Distinguishing Astrophysical Sources.

It is important to identify critical accuracies in measurement needed to distinguish between the pion source and the muon-damped source. Choosing the parameter set 1 for the analysis, we present the results in Fig. 2.9 where two different approaches for determining  $\Delta S^I/S^I$  are used.

In Fig. 2.9, we determine  $\Delta S^I/S^I$  by applying Poisson statistics. In the left panel of Fig. 2.9, which has the muon-damped source as the true source, the reconstructed  $3\sigma$  range for the neutrino flavor ratio just touches the pion source at  $\Delta R^I/R^I = 11\%$  and  $\Delta S^I/S^I = 13.8\%$ . In the right panel of this figure, which has the pion source as the true source, the reconstructed  $3\sigma$  range for the neutrino flavor ratio just touches the muon-damped source at  $\Delta R^I/R^I = 4\%$  and  $\Delta S^I/S^I = 4.6\%$ .

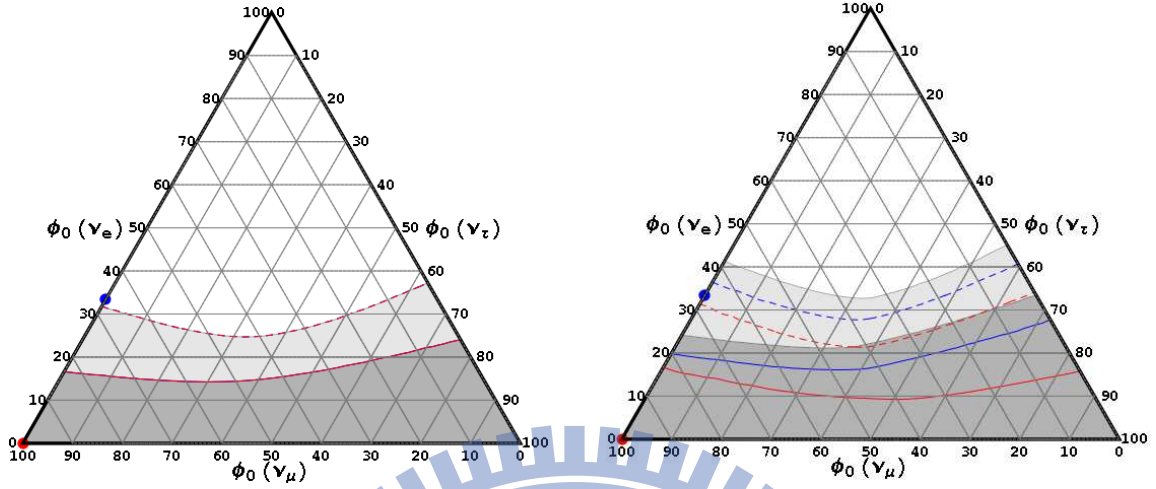


Figure 2.7: The reconstructed ranges for the neutrino flavor ratio at the source for an input muon-damped source with  $\Delta R^I/R^I = 10\%$  and  $\Delta S^I/S^I$  related to the former by the Poisson statistics, E.q. (2.17). The left panel is obtained with  $\theta_{13}$  and  $\theta_{23}$  taken from the parameter set 1 in Table 2.4 and the input CP phase taken to be  $0$ ,  $\pi/2$  and  $\pi$  respectively. The right panel is obtained with the parameter sets 3a, 3b and 3c in Table 2.4. Light gray area, dashed blue and dashed red lines correspond to the  $3\sigma$  ranges for the reconstructed neutrino flavor ratio at the source for  $\cos \delta = 1$ ,  $\cos \delta = 0$  and  $\cos \delta = -1$  respectively. Gray area, blue and red lines correspond to the  $1\sigma$  ranges for the reconstructed neutrino flavor ratio at the source for  $\cos \delta = 1$ ,  $\cos \delta = 0$  and  $\cos \delta = -1$  respectively. The effect from the CP phase  $\delta$  only appears in the right panel.

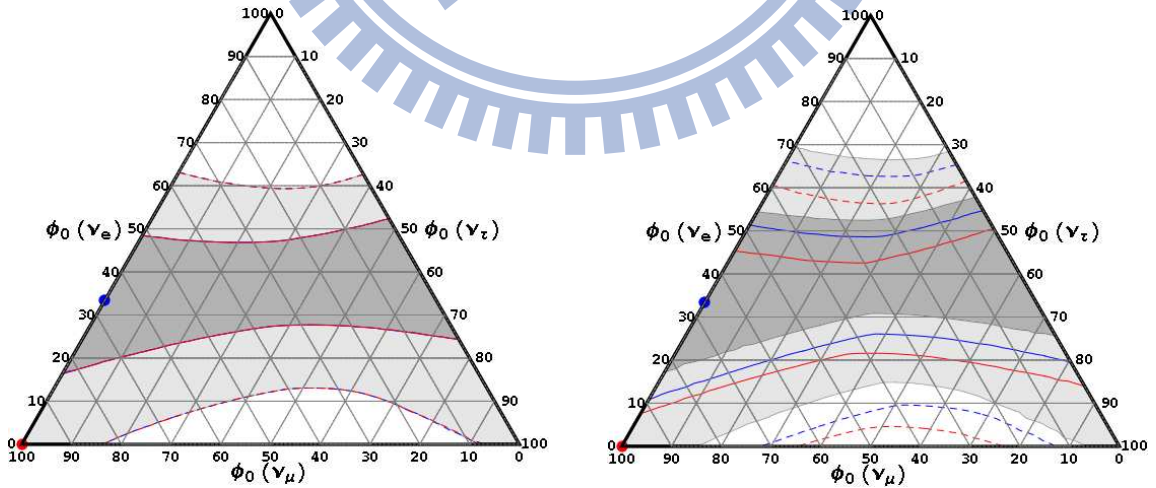


Figure 2.8: The reconstructed  $1\sigma$  and  $3\sigma$  ranges for the neutrino flavor ratio at the source for an input pion source with  $\Delta R^I/R^I = 10\%$  and  $\Delta S^I/S^I$  related to the former by the Poisson statistics. The choices of parameter sets are identical to those of Fig. 2.7. Once more, the effect from the CP phase  $\delta$  only appears in the right panel.

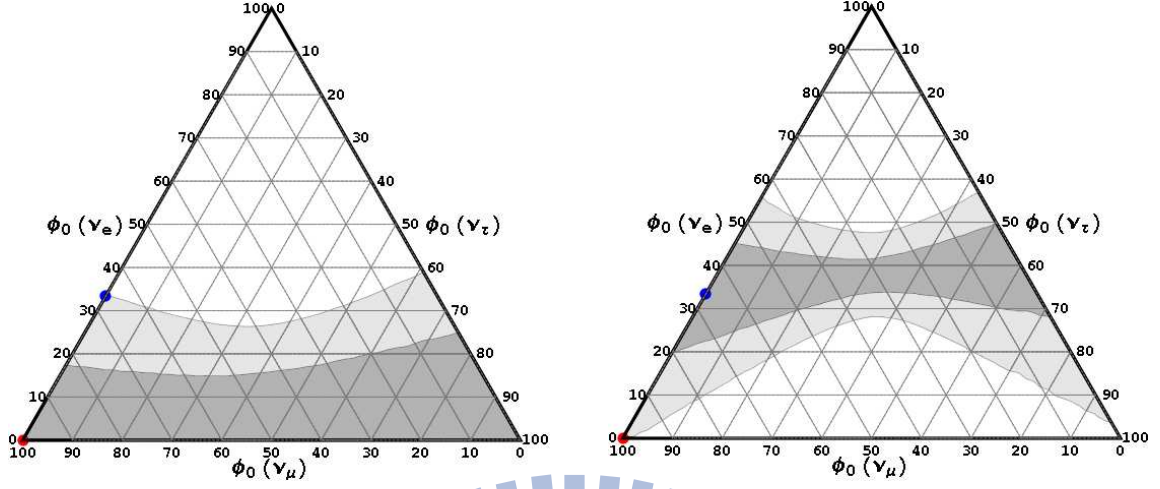


Figure 2.9: Critical accuracies needed to distinguish between the pion source and the muon-damped source. In the left panel where the muon-damped source is the true source, the reconstructed  $3\sigma$  range for the neutrino flavor ratio just touches the pion source at  $\Delta R^I/R^I = 11\%$  and  $\Delta S^I/S^I$  related to the former by the Poisson statistics, E.q. (2.17). In the right panel where the pion source is the true source, the reconstructed  $3\sigma$  range for the neutrino flavor ratio just touches the muon-damped source at  $\Delta R^I/R^I = 4\%$  and  $\Delta S^I/S^I$  related to the former by the Poisson statistics, E.q. 2.17.. We choose parameter set I in Table 2.4 for this analysis.

## 2.5 Reconstructing Flavor Ratio of Source at High Energy.

At higher energy,  $E\nu \geq 33.3$  PeV, the lifetime of the tau lepton produced by  $\nu_\tau$  charged current interaction becomes long enough so that the tau-lepton could pass through the detector fiducial volume without decaying. In this process, the tau-lepton loses its energy just like a muon does and the signal appears like a track event. Thus from an experimental point of view, one should classify the tau-lepton signature as a track event. We therefore redefine the primary flavor-ratio variable  $R^{II} = \phi(\nu_e)/(\phi(\nu_\mu) + \phi(\nu_\tau))$ , which is the ratio of shower-like events to track-like events. The secondary variable is the ratio of track-like signals  $S^{II} = \phi(\nu_\mu)/\phi(\nu_\tau)$ .

The threshold energy for the transition from variables  $R^I$  and  $S^I$  to  $R^{II}$  and  $S^{II}$  depends on the detector designs. In our discussions here, we adopt the variables  $R^I$  and  $S^I$  for  $E\nu < 33.3$  PeV and adopt the variables  $R^{II}$  and  $S^{II}$  for  $E\nu > 33.3$  PeV. Between 3.3 PeV and 33.3 PeV, tau leptons can be identified individually. Therefore neutrino flavor ratio can be precisely determined such that both sets of parameters can be adopted for the analysis.

The relations between the measurement errors  $\Delta R^a/R^a$  and  $\Delta S^a/S^a$  with  $a = I$  and  $II$  respec-



parameters	Best fit	$1\sigma^*$	$3\sigma$
$\sin^2 \theta_{12}$	0.29	0.266-0.318	0.23-0.38
$\sin^2 \theta_{13}$	0	<0.0122	<0.047
$\sin^2 \theta_{23}$	0.5	0.431-0.572	0.34-0.68

\*digitalized from graph.[23]

Table 2.5: Neutrino mixing parameters

tively are assumed to be dominated by statistical errors, which imply [17]

$$\frac{\Delta S^a}{S^a} = \frac{1 + S^a}{\sqrt{S^a}} \sqrt{\frac{R^a}{1 + R^a}} \frac{\Delta R^a}{R^a}. \quad (2.19)$$

This relation in fact underestimates  $\Delta S^a/S^a$  relative to  $\Delta R^a/R^a$ . Hence the flavor reconstruction result based on this relation should be viewed as an optimistic one. The statistical analysis is performed according to the following formula

$$\chi_a^2 = \left( \frac{R_{th}^a - R_{exp}^a}{\sigma_{R_{exp}^a}} \right)^2 + \left( \frac{S_{th}^a - S_{exp}^a}{\sigma_{S_{exp}^a}} \right)^2 + \sum_{l,m=12,13,23} \chi_{\theta_{lm}}^2, \quad (2.20)$$

with  $\sigma_{R_{exp}^a} = (\Delta R^a/R^a)R_{exp}^a$ ,  $\sigma_{S_{exp}^a} = (\Delta S^a/S^a)S_{exp}^a$ . Each individual  $\chi_{\theta_{lm}}^2$  is constructed from the fitting of Ref. [23]. We list best-fit values of mixing angles and the corresponding  $1\sigma$  and  $3\sigma$  ranges in Table 2.5. The suffix ‘‘th’’ indicates the theoretical predicted values which depend on the source neutrino flavor ratio and the neutrino mixing angles. The suffix ‘‘exp’’ indicates the experimentally measured values which are generated by the true neutrino flavor ratio and the best-fit values of neutrino mixing angles. This analysis considers all possible neutrino flavor ratios at the source to calculate the  $\chi_a^2$  values. Since we have taken  $R_{exp}^a$  and  $S_{exp}^a$  as those generated by input true values of initial neutrino flavor ratios and neutrino mixing parameters, we have  $(\chi_a^2)_{\min} = 0$  occurring at these input true values of parameters. The boundaries for  $1\sigma$  and  $3\sigma$  ranges of initial neutrino flavor ratios are given by  $\Delta\chi_a^2 = 2.3$  and  $\Delta\chi_a^2 = 11.8$  respectively, where  $\Delta\chi_a^2 \equiv \chi_a^2 - (\chi_a^2)_{\min} = \chi_a^2$  in this analysis.

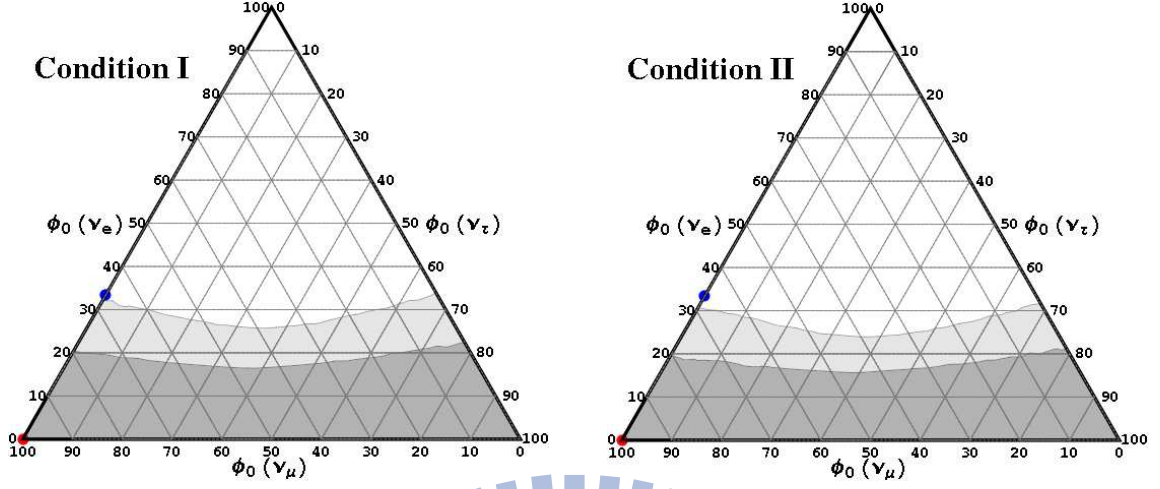


Figure 2.10: Reconstructed ranges for muon-damped source with  $\Delta R^a/R^a = 10\%$  and  $\Delta S^a/S^a = 12\%$ . The dark and light shaded areas denote the range of reconstructed neutrino flavor ratios under  $1\sigma$  and  $3\sigma$  limits. The left and right panels correspond to the condition I and II. The pion source can be ruled out at the  $3\sigma$  level for both conditions.

### 2.5.1 The Reconstruction of Muon-damped Source

Let us take the muon-damped source as the input true source and consider its reconstruction. The accuracy for measuring  $R^a$  is taken as  $\Delta R^a/R^a = 10\%$ , which implies  $\Delta S^I/S^I = 12.5\%$  and  $\Delta S^{II}/S^{II} = 9.78\%$  from Eq. (2.17). The reconstructed regions of neutrino flavor ratio are comparable for  $a = I$  and  $II$ . For an input muon-damped source, the pion source can be ruled out at the  $3\sigma$  level as shown in Fig. 2.10.

However, measuring  $R^a$  is easier than measuring  $S^a$  for neutrino telescopes. If the measurements on  $S^a$  are not available, the results for flavor-ratio reconstruction are quite different. Fig. 2.11 shows the reconstructed flavor ratios with  $\Delta R^a/R^a = 10\%$ . The reconstructed region of neutrino flavor for  $a = I$  is much larger than that for  $a = II$ . The pion source can only be ruled out at  $3\sigma$  level for the condition II and not for the condition I.

### 2.5.2 The Reconstruction of Pion Source

We first consider the case that both  $R^a$  and  $S^a$  are measured with the accuracies  $\Delta R^a/R^a = 10\%$  and  $\Delta S^I/S^I = 11.4\%$  ( $\Delta S^{II}/S^{II} = 11.7\%$ ). The reconstructed regions of neutrino flavor ratio are comparable for  $a = I$  and  $II$ . For an input pion source, the muon-damped source can be ruled out at the  $1\sigma$  level as shown in Fig. 2.12 for both energy conditions. If one only measures  $R^a$  with

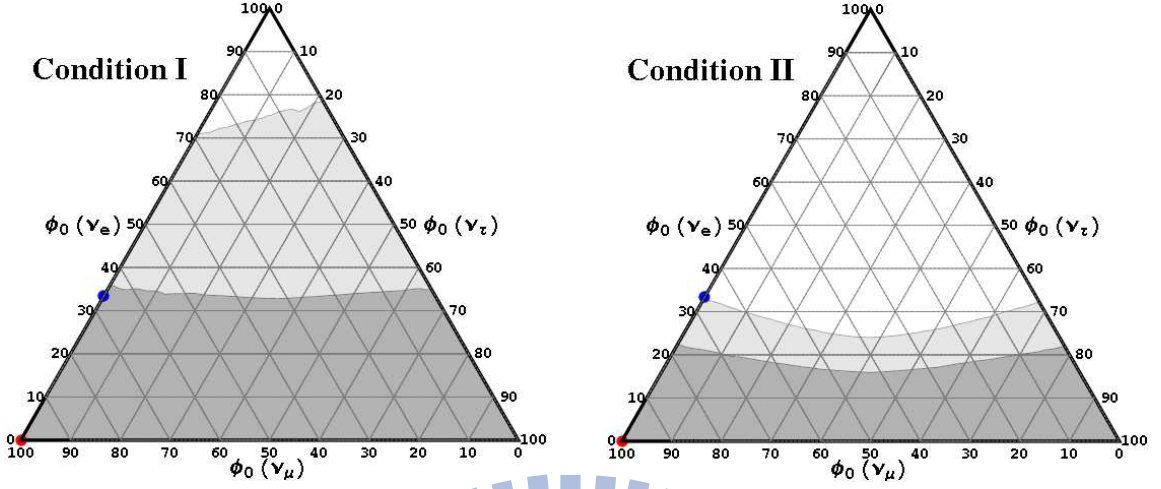


Figure 2.11: Reconstructed ranges for muon-damped source with  $\Delta R^a/R^a = 10\%$  only. The dark and light shaded areas denote the range of reconstructed neutrino flavor ratios under  $1\sigma$  and  $3\sigma$  limits. The left and right panels correspond to the condition I and II. The pion source can be ruled out at  $3\sigma$  level for the condition II but not for the condition I even at  $1\sigma$  level.

$\Delta R^a/R^a = 10\%$ , it is shown in Fig. 2.13 that the reconstructed region for  $a=I$  covers all physical parameter space; while the reconstructed region for  $a=II$  remains comparable to that in Fig. 2.12. Once again, the muon-damped source can be ruled out for condition II at  $1\sigma$  level, but not for condition I at the same confidence level.

From the reconstructions of pion source and muon-damped source, it is evident that this new parameter  $R^{II}$  is more efficient than  $R^I$  for reducing the source uncertainty if the measurements on  $S^a$  are not available.

### 2.5.3 $R^{II}$ and Tri-bimaximal Limit

Let us consider the tri-bimaximal limit of neutrino mixing parameters [24]:

$$\sin^2 \theta_{23} = 1/2, \quad \sin^2 \theta_{12} = 1/3, \quad \sin^2 \theta_{13} = 0. \quad (2.21)$$

In this limit, one can show that the  $R^I = S^I/2$  and  $S^{II} = 1$ . To further simplify our discussions, let us consider astrophysical sources with negligible  $\nu_\tau$  fractions such that  $\phi_0(\nu_e) : \phi_0(\nu_\mu) : \phi_0(\nu_\tau) = \alpha : 1 - \alpha : 0$  with  $0 \leq \alpha \leq 1$ . Fig. 2.14 shows the measured flux ratios as functions of the  $\nu_e$  fraction  $\alpha$ . It is seen that  $S^I$  and  $R^{II}$  are more sensitive to  $\alpha$  while  $R^I$  and  $S^{II}$  is either less

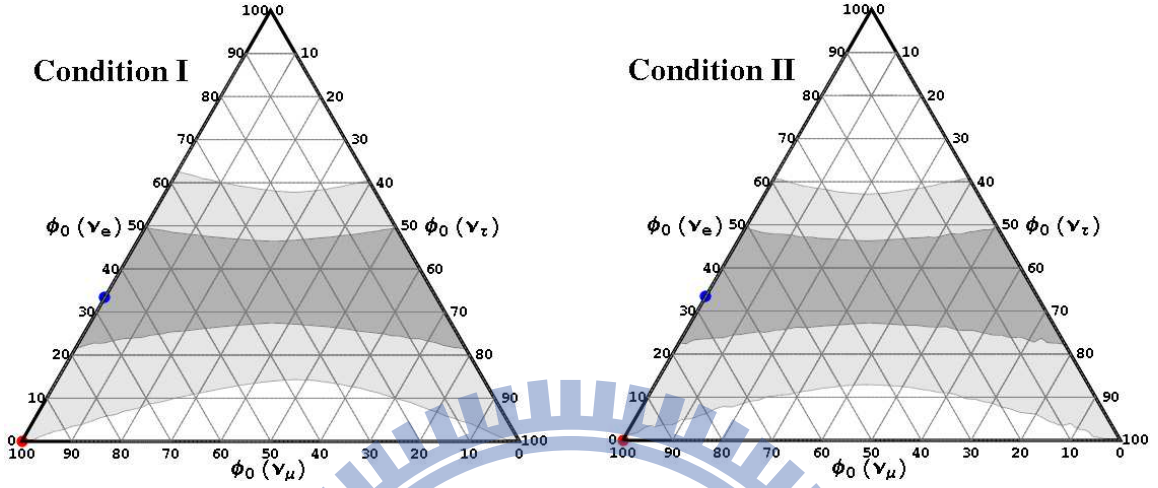


Figure 2.12: Reconstructed ranges for pion source with  $\Delta R^a/R^a = 10\%$  and  $\Delta S^a/S^a = 12\%$ . The dark and light shaded areas denote the range of reconstructed neutrino flavor ratios under  $1\sigma$  and  $3\sigma$  limits. The left and right panels correspond to the condition I and II. The muon-damped source can be ruled out at the  $1\sigma$  level for both conditions.

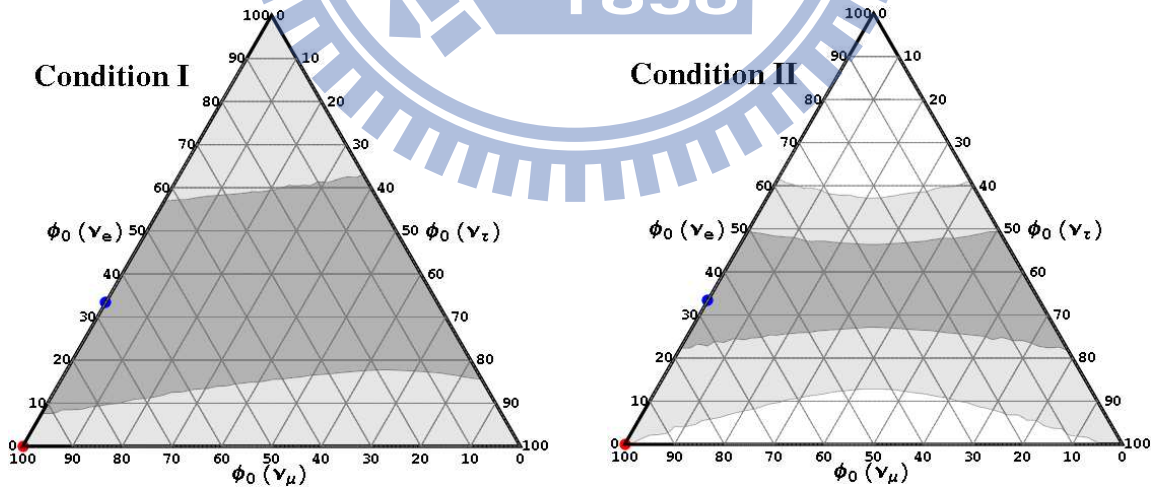


Figure 2.13: Reconstructed ranges for pion source with  $\Delta R^a/R^a = 10\%$  only. The dark and light shaded areas denote the range of reconstructed neutrino flavor ratios under  $1\sigma$  and  $3\sigma$  limits. The left and right panels correspond to the condition I and II. For condition I,  $3\sigma$  limit covers all flavor ratio of source. But the muon-damped source can be ruled out at  $1\sigma$  level for condition II.

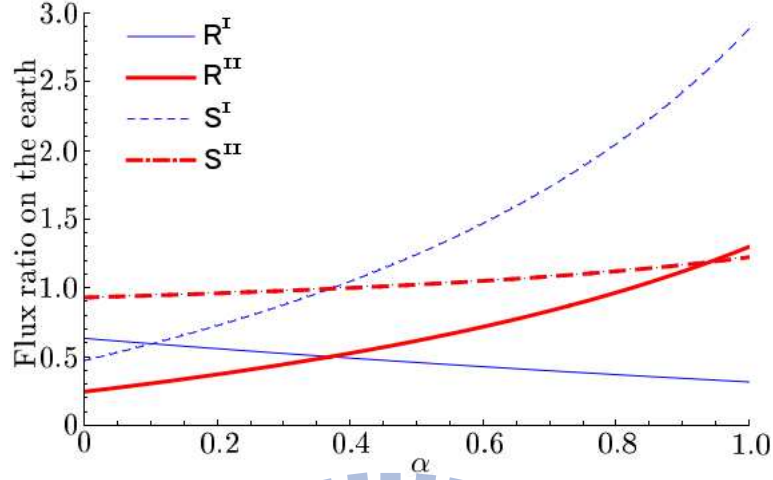


Figure 2.14: Measured flux ratios for input source ratios,  $\phi_0(\nu_e) : \phi_0(\nu_\mu) : \phi_0(\nu_\tau) = \alpha : 1 - \alpha : 0$  with  $0 \leq \alpha \leq 1$ . The thick and long dashed lines correspond to  $R^{\text{II}}$  and  $S^{\text{II}}$  respectively. The thin and short-dashed lines denote  $R^{\text{I}}$  and  $S^{\text{I}}$  respectively. It is seen that  $S^{\text{I}}$  and  $R^{\text{II}}$  are more sensitive to  $\alpha$ ; while  $R^{\text{I}}$  and  $S^{\text{II}}$  are less sensitive to this parameter.

sensitive to  $\alpha$  or completely independent of this parameter. Quantitatively, we have

$$f(\alpha) \equiv \frac{R^{\text{II}}}{R^{\text{I}}} = -\frac{1}{2} \left( \frac{11 + 3\alpha}{7 - 3\alpha} \right)^2, \quad (2.22)$$

where  $R^{\prime a} \equiv dR^a/d\alpha$ . We have  $f(0) = -1.25$  and  $f(1) = -6.13$ . Eq. (2.22) explains why  $R^{\text{II}}$  is more efficient than  $R^{\text{I}}$ . Furthermore, since  $S^{\text{II}}$  is rather insensitive to  $\alpha$  due to the approximate  $\nu_\mu - \nu_\tau$  symmetry, the additional measurement of  $S^{\text{II}}$  does not improve the reconstruction of neutrino flavor ratio at the source already provided by the measurement of  $R^{\text{II}}$ .

This result has implication for future neutrino telescopes. It is possible to study neutrino flavor physics with a larger separation between detector modules while keeping the total number of modules fixed. Such a large separation could enhance exposure at higher energies but sacrifice exposure at low energies. We can afford to do that if there are enough neutrino events at the valid energy range for  $R^{\text{II}}$ .

## 2.6 Reconstructing Flavor Ratio of Source by Monte Carlo Method with N Events

From experimental viewpoint, the flavor ratio on the earth must be constructed from measured events. In this section, we use 200 and 400 neutrino events to determine the flavor ratio by Monte-Carlo method. The probability for measuring a particular flavor in one event is determined by theoretical predicted result of neutrino oscillation. For example, the neutrino flavor ratio on the Earth from a pion source with best-fit value of mixing angles is  $\phi_\pi(\nu_e) : \phi_\pi(\nu_\mu) : \phi_\pi(\nu_\tau) = 0.35 : 0.33 : 0.32$ . Hence the probabilities for measuring a electron, muon and tau in one event correspond are 35%, 33% and 32% respectively. Repeating this process N times, the neutrino flavor ratio on the Earth with N events can be determined by Monte-Carlo method. However this is not enough to construct the possible range of neutrino flavors on the Earth. We reproduce those N events by M times to establish the distribution of neutrino flavor ratios. In order to trim the long tail of distribution, the boundary for most probable flavor ratios are set at 99.7% and 68.2%.

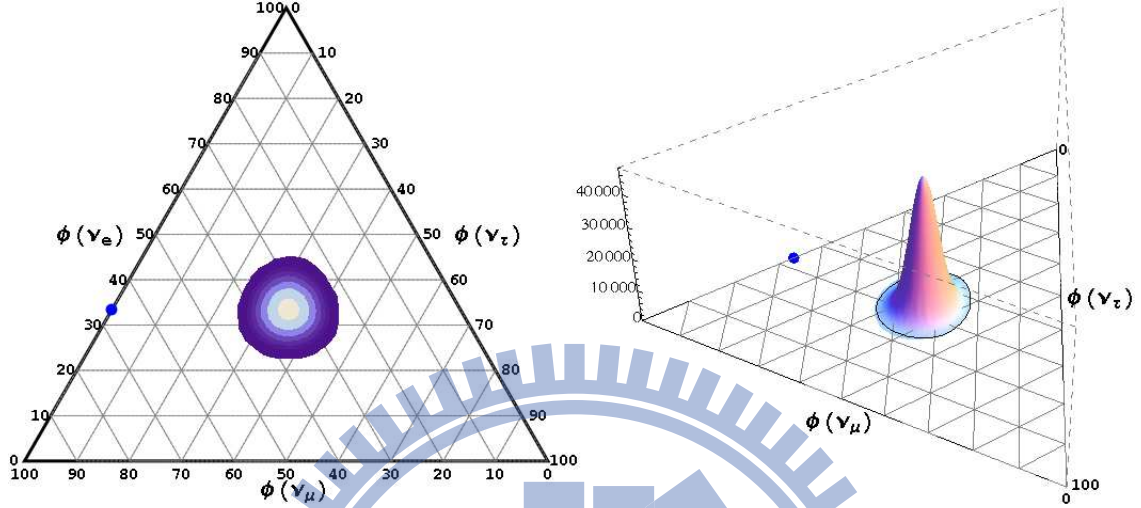
### 2.6.1 The Flavor Ratios on the Earth from Pion Source with 200 Events

The neutrino flavor ratio on the Earth from pion source is  $\phi_\pi(\nu_e) : \phi_\pi(\nu_\mu) : \phi_\pi(\nu_\tau) = 0.35 : 0.33 : 0.32$ . This result only considers the best-fit values of mixing angles, and this flavor ratio has been shown in Fig. 2.2(a). This flavor ratio also represents the probability for observing each neutrino flavor in a single event. In this subsection, each flavor ratio is determined by 200 events with Monte-Carlo method. Fig. 2.15 shows the distributions of flavor ratios on the Earth by Monte-Carlo method. The distribution of flavor ratios is formed by reproducing 10 million experiments and the long tail of distribution is cut off at 99.7% and 68.2%.

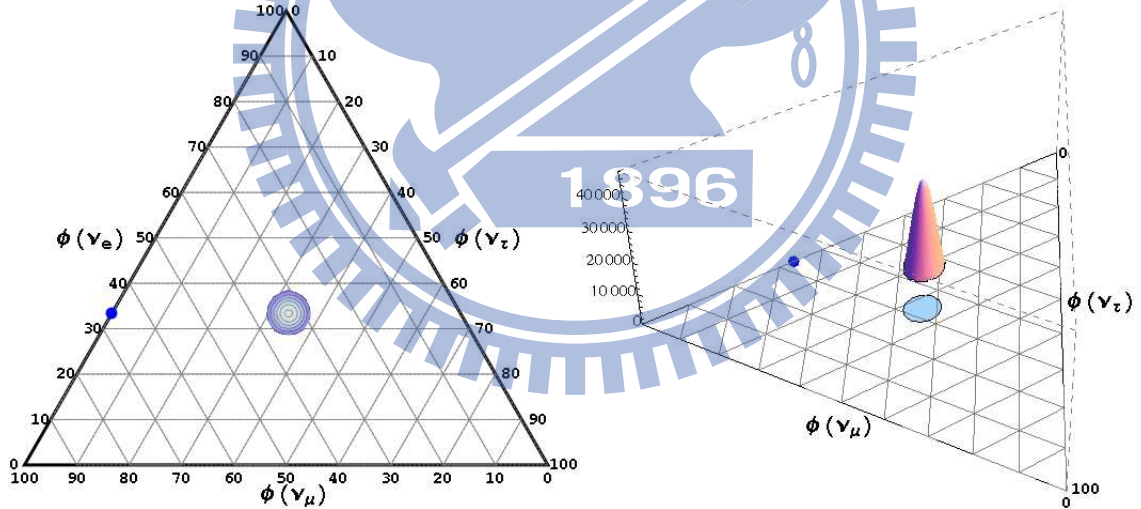
#### 2.6.1.1 The Reconstructed Neutrino Flavor Ratios at Low Energy, $E_\nu \leq 33.3$ PeV

At low energy,  $E_\nu \leq 33.3$  PeV, the values of  $\Delta R^I/R^I$  and  $\Delta S^I/S^I$  are determined by event numbers of different flavors. In this case, one has

$$\frac{\Delta R^I}{R^I} = \sqrt{\frac{1}{N_e + N_\tau} + \frac{1}{N_\mu}} \quad , \quad \frac{\Delta S^I}{S^I} = \sqrt{\frac{1}{N_e} + \frac{1}{N_\tau}} \quad (2.23)$$



(a) The contour at the left plot denotes the boundary of flavor ratios. The right plot shows the distribution of the flavor ratios. The distribution leads  $\Delta R^I/R^I = (14.23 - 17.07)\%$  and  $\Delta S^I/S^I = (16.01 - 19.00)\%$  with  $E_\nu < 33$  PeV. This distribution also leads  $\Delta R^{II}/R^{II} = (14.21 - 16.93)\%$  and  $\Delta S^{II}/S^{II} = (16.06 - 19.16)\%$  with  $E_\nu > 33$  PeV.



(b) The contour at the left plot denotes the boundary of flavor ratios. The right plot shows the distribution of the flavor ratios. The distribution leads  $\Delta R^I/R^I = (14.61 - 15.75)\%$  and  $\Delta S^I/S^I = (16.67 - 17.92)\%$  with  $E_\nu < 33$  PeV. This distribution also leads  $\Delta R^{II}/R^{II} = (14.53 - 15.66)\%$  and  $\Delta S^{II}/S^{II} = (16.73 - 18.04)\%$  with  $E_\nu > 33$  PeV.

Figure 2.15: The distribution of neutrino flavor ratio on the Earth from pion source for 200 events. Each flavor ratio on the ternary plot is generated by 200 events. There are 10 million flavor ratios generated on the ternary plot, which form the distribution of flavor ratios. The blue point denotes the original flavor ratio of pion source. In panel (a), the distribution of flavor ratios is cut off at 99.7%. In panel (b), the distribution of flavor ratios is cut off at 68.2%.

where  $N_e$ ,  $N_\mu$  and  $N_\tau$  are the event numbers of electron, muon and tau flavor, and  $N_e + N_\mu + N_\tau = 200$ .

In 99.7% cut-off case, the distribution leads to  $\Delta R^I/R^I = (14.23 - 17.07)\%$  and  $\Delta S^I/S^I = (16.01 - 19.00)\%$  with  $E_\nu \leq 33.3$  PeV. The values of mixing angles are same as Table 2.5. We repeat the statistical analysis according to Eq. (2.20) for each possibly measured flavor ratio shown in Fig. 2.15. The left panel in Fig. 2.16 shows the reconstructed neutrino flavor ratios for an input pion source by measuring  $R^I$  only. The muon-damped source cannot be ruled out even at  $1\sigma$  level. The right panel shows the reconstructed neutrino flavor ratios for an input pion source by measuring both  $R^I$  and  $S^I$ . The muon-damped source cannot be ruled out even at  $1\sigma$  level too.

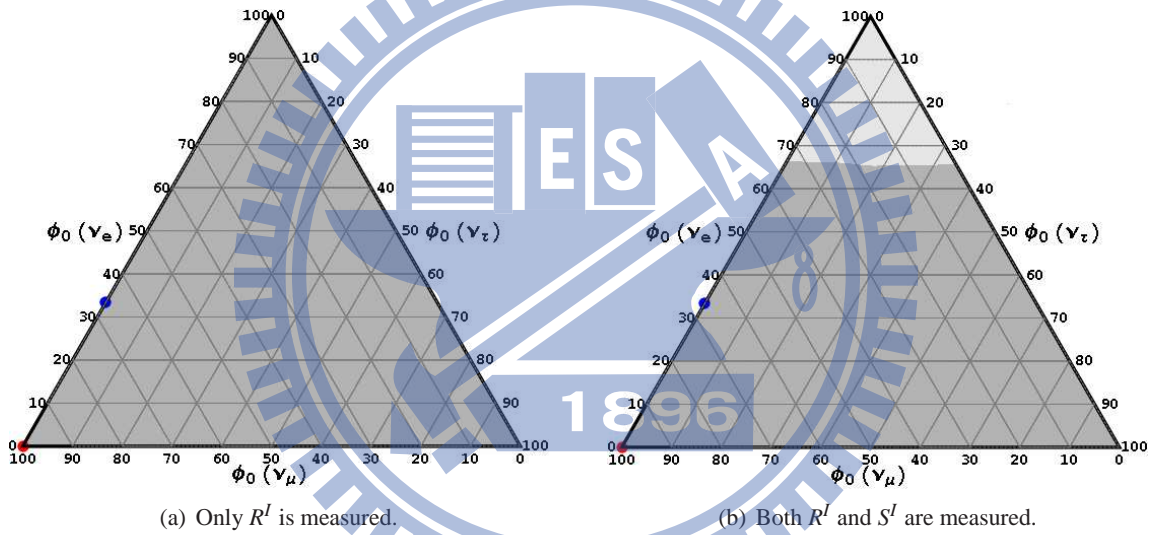


Figure 2.16: The reconstructed ranges for pion source with 200 events and neutrino energy below 33.3 PeV. The range for possibly measured flavor ratio is cut off at 99.7%. The dark and light shades area denote  $1\sigma$  and  $3\sigma$  reconstructed ranges.

In 68.2% cut-off case, the distribution leads to  $\Delta R^I/R^I = (14.23 - 17.07)\%$  and  $\Delta S^I/S^I = (14.53 - 15.66)\%$ . The values of mixing angles are same as Table 2.5. The left panel in Fig. 2.17 shows the reconstructed neutrino flavor ratios for an input pion source by measuring  $R^I$  only. The muon-damped source cannot be ruled out even at  $1\sigma$  level. The right panel shows the reconstructed neutrino flavor ratios for an input pion source by measuring both  $R^I$  and  $S^I$ . The muon-damped source cannot be ruled out even at  $1\sigma$  level too.



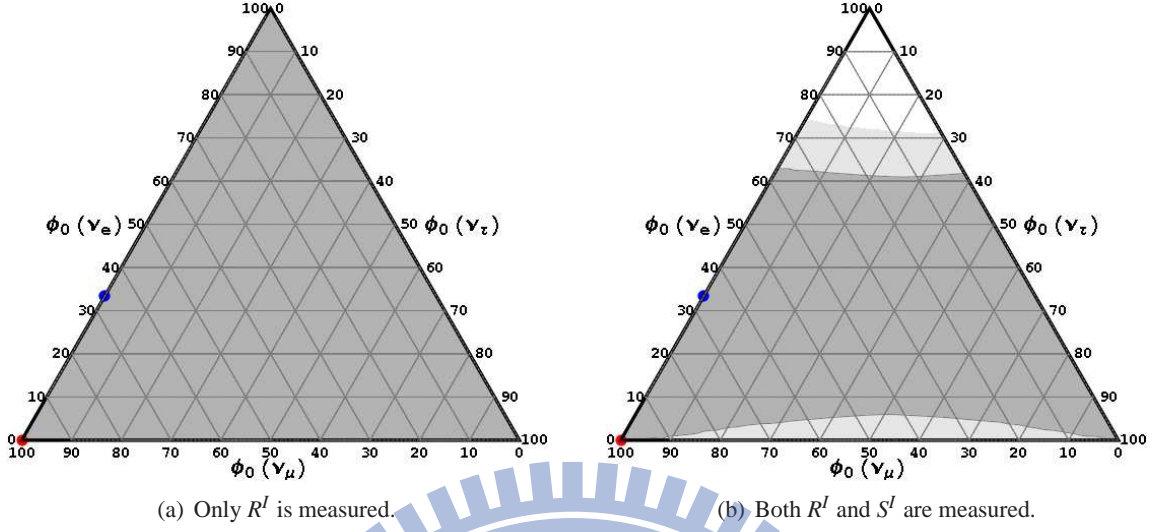


Figure 2.17: The reconstructed ranges for pion source with 200 events and neutrino energy below 33.3 PeV. The range for possibly measured flavor ratio is cut off at 68.2%. The dark and light shades area denote  $1\sigma$  and  $3\sigma$  reconstructed ranges.

### 2.6.1.2 The Reconstructed Neutrino Flavor Ratios at High Energy, $E_\nu \geq 33.3$ PeV

At high energy,  $E_\nu \geq 33.3$  PeV, we can derive

$$\frac{\Delta R^{II}}{R^{II}} = \sqrt{\frac{1}{N_\mu + N_\tau} + \frac{1}{N_e}}, \quad \frac{\Delta S^{II}}{S^{II}} = \sqrt{\frac{1}{N_\mu} + \frac{1}{N_\tau}} \quad (2.24)$$

where  $N_e$ ,  $N_\mu$  and  $N_\tau$  are the event numbers of electron, muon and tau flavor, and  $N_e + N_\mu + N_\tau = 200$ .

In 99.7% cut-off case, the distribution leads to  $\Delta R^{II}/R^{II} = (14.21 - 16.93)\%$  and  $\Delta S^{II}/S^{II} = (16.06 - 19.16)\%$ . The values of mixing angles are same as Table 2.5. The left panel in Fig. 2.18 shows the reconstructed neutrino flavor ratios for an input pion source by measuring  $\Delta R^{II}/R^{II}$  only. The muon-damped source cannot be ruled out even at  $1\sigma$  level. The right panel shows the reconstructed neutrino flavor ratios for an input pion source by measuring  $\Delta R^{II}/R^{II}$  and  $\Delta S^I/S^I$ . The muon-damped source cannot be ruled out even at  $1\sigma$  level too.

In 68.2% cut-off case, the distribution leads to  $\Delta R^{II}/R^{II} = (14.53 - 15.66)\%$  and  $\Delta S^{II}/S^{II} = (16.73 - 18.04)\%$ . The values of mixing angles are same as Table 2.5. The left panel in Fig. 2.19 shows the reconstructed neutrino flavor ratios for an input pion source by measuring parameter  $R^{II}$  only. The muon-damped source cannot be ruled out even at  $1\sigma$  level. The right panel shows

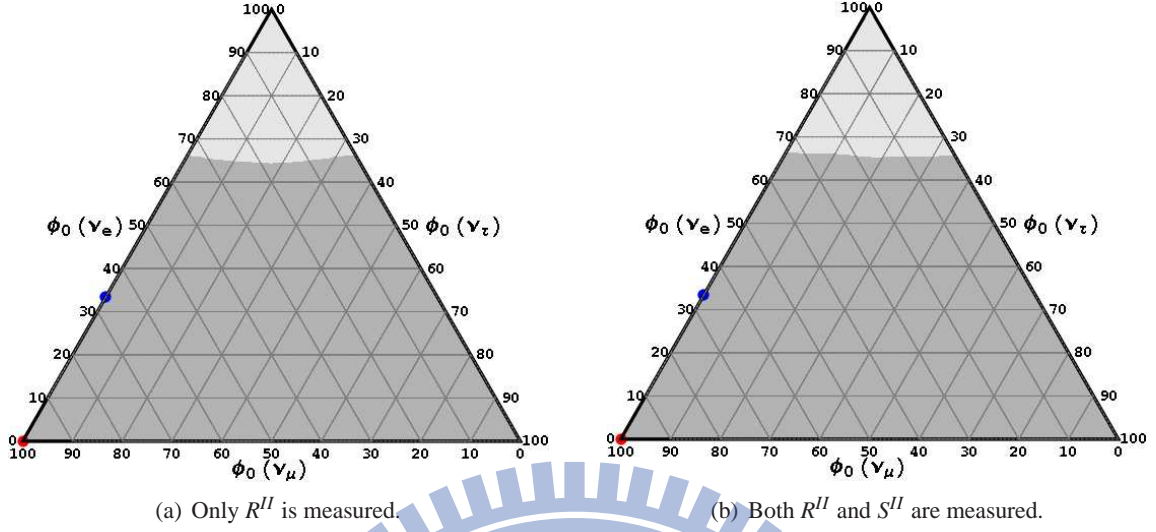


Figure 2.18: The reconstructed ranges for pion source with 200 events and neutrino energy above 33.3 PeV. The range for possibly measured flavor ratio is cut off at 99.7%. The dark and light shades area denote  $1\sigma$  and  $3\sigma$  reconstructed ranges.

the reconstructed neutrino flavor ratios for an input pion source by measuring parameters  $R^{II}$  and  $S^{II}$ . The muon-damped source cannot be ruled out even at  $1\sigma$  level too.

## 2.6.2 The flavor ratios on the Earth from the Muon-damped source with 200 events

The neutrino flavor ratio on the Earth from muon-damped source is  $\phi_\mu(\nu_e) : \phi_\mu(\nu_\mu) : \phi_\mu(\nu_\tau) = 0.24 : 0.37 : 0.39$ . This result only considers the best-fit values of mixing angles, and this flavor ratio has been shown in Fig. 2.2(a). This flavor ratio also represent the probability for observing each neutrino flavor in a single event. In this section, each flavor ratio is determined by 200 events with Monte-Carlo method. Fig. 2.20 show the distributions of flavor ratios on the Earth by Monte-Carlo method. The distribution of flavor ratios is formed by repeating 10 million experiments and the long tail of distribution is cut off at 99.7% and 68.2%.

### 2.6.2.1 The Reconstructed Neutrino Flavor Ratios at Low Energy, $E_\nu \leq 33.3$ PeV

In 99.7% cut-off case, the distribution leads to  $\Delta R^I/R^I = (14.14 - 15.84)\%$  and  $\Delta S^I/S^I = (17.08 - 23.50)\%$  with  $E_\nu \leq 33$  PeV. The values of mixing angles are same as Table 2.5. The left panel in Fig. 2.21 shows the reconstructed neutrino flavor ratios for an input pion source by measuring  $R^I$  only. The pion source cannot be ruled out even at  $1\sigma$  level. The right panel shows

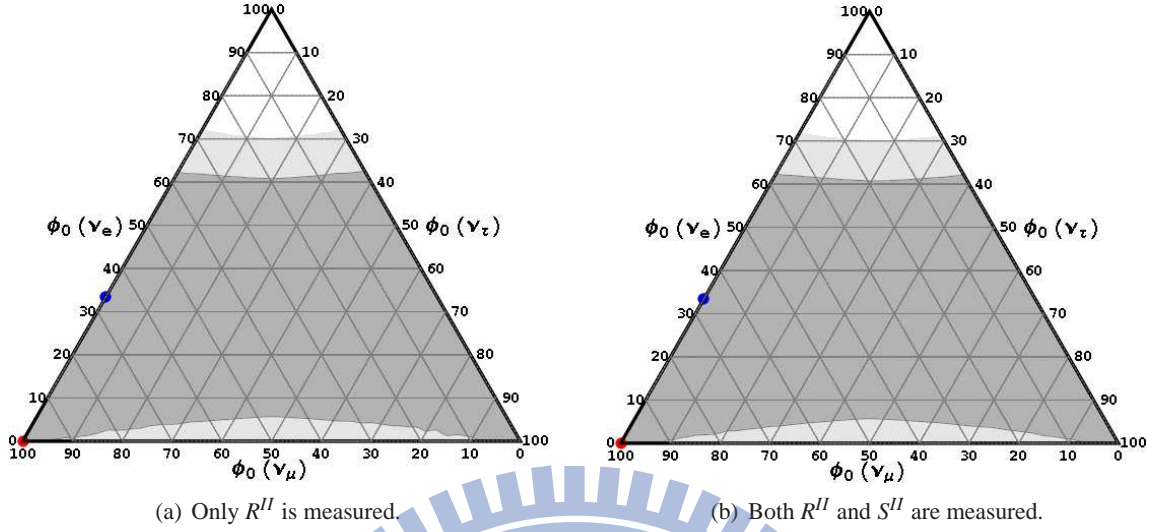


Figure 2.19: The reconstructed ranges for pion source with 200 events and neutrino energy above 33.3 PeV. The range for possibly measured flavor ratio is cut off at 68.2%. The dark and light shades area denote  $1\sigma$  and  $3\sigma$  reconstructed ranges.

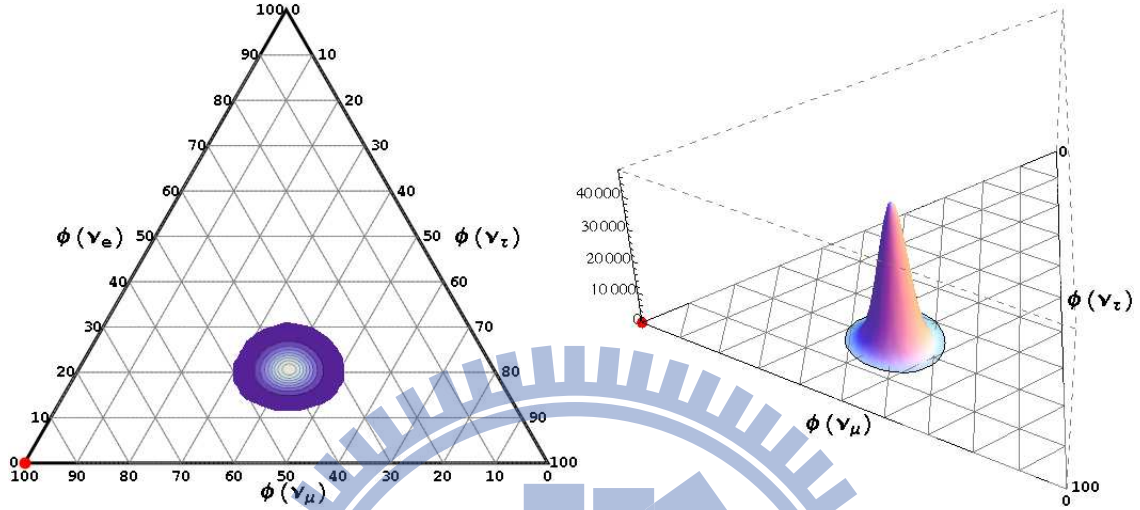
the reconstructed neutrino flavor ratios for an input muon-damped source by measuring both  $R^I$  and  $S^I$ . The muon-damped source cannot be ruled out even at  $1\sigma$  level too.

In 68.2% cut-off case, the distribution leads to  $\Delta R^I/R^I = (14.25 - 14.93)\%$  and  $\Delta S^I/S^I = (18.10 - 20.58)\%$ . The values of mixing angles are same as Table 2.5. The left panel in Fig. 2.22 shows the reconstructed neutrino flavor ratios for an input muon-damped source by measuring  $R^I$  only. The pion source cannot be ruled out even at  $1\sigma$  level. The right panel shows the reconstructed neutrino flavor ratios for an input muon-damped source by measuring both  $R^I$  and  $S^I$ . The pion source can be ruled out even at  $1\sigma$  level.

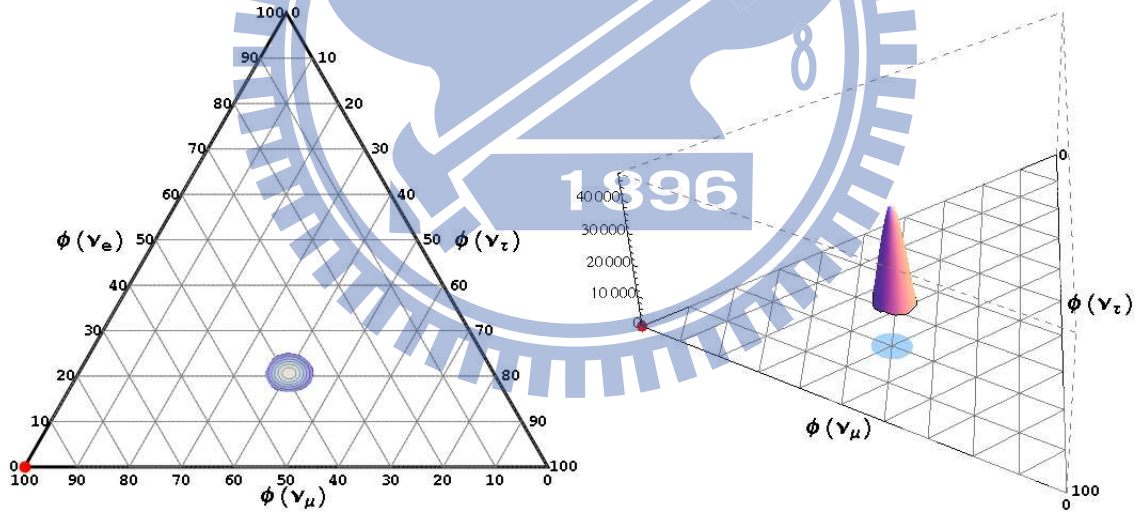
### 2.6.2.2 The Reconstructed Neutrino Flavor Ratios at Low Energy, $E_\nu \geq 33.3$ PeV

In 99.7% cut-off case, the distribution leads to  $\Delta R^{II}/R^{II} = (15.29 - 22.16)\%$  and  $\Delta S^{II}/S^{II} = (15.03 - 17.08)\%$  with  $E_\nu \geq 33$  PeV. The values of mixing angles are same as Table 2.5. The left panel in Fig. 2.23 shows the reconstructed neutrino flavor ratios for an input muon-damped source by measuring  $R^{II}$  only. The pion source cannot be ruled out even at  $1\sigma$  level. The right panel shows the reconstructed neutrino flavor ratios for an input muon-damped source by measuring both  $R^{II}$  and  $S^{II}$ . The pion source cannot be ruled out even at  $1\sigma$  level too.

In 68.2% cut-off case, the distribution leads to  $\Delta R^{II}/R^{II} = (16.33 - 19.05)\%$  and  $\Delta S^{II}/S^{II} =$



(a) The contour at the left plot denotes the boundary of flavor ratios. The right plot shows the distribution of the flavor ratios. The distribution leads  $\Delta R^I/R^I = (15.29 - 22.16)\%$  and  $\Delta S^I/S^I = (15.03 - 17.08)\%$  with  $E_\nu < 33$  PeV. This distribution also leads  $\Delta R^{II}/R^{II} = (14.14 - 15.84)\%$  and  $\Delta S^{II}/S^{II} = (17.08 - 23.50)\%$  with  $E_\nu > 33$  PeV.



(b) The contour at the left plot denotes the boundary of flavor ratios. The right plot shows the distribution of the flavor ratios. The distribution leads  $\Delta R^I/R^I = (14.25 - 14.93)\%$  and  $\Delta S^I/S^I = (18.10 - 20.58)\%$  with  $E_\nu < 33$  PeV. This distribution also leads  $\Delta R^{II}/R^{II} = (16.33 - 19.05)\%$  and  $\Delta S^{II}/S^{II} = (15.48 - 16.34)\%$  with  $E_\nu > 33$  PeV.

Figure 2.20: The distribution of neutrino flavor ratio on the Earth from muon-damped source for 200 events. Each flavor ratio on the ternary plot is generated by 200 events. There are 10 million flavor ratios generated on the ternary plot, which form the distribution of flavor ratios. The red point denotes the original flavor ratio of muon-damped source. In panel (a), the distribution of flavor ratios is cut off at 99.7%. In panel (b), the distribution of flavor ratios is cut off at 68.2%.

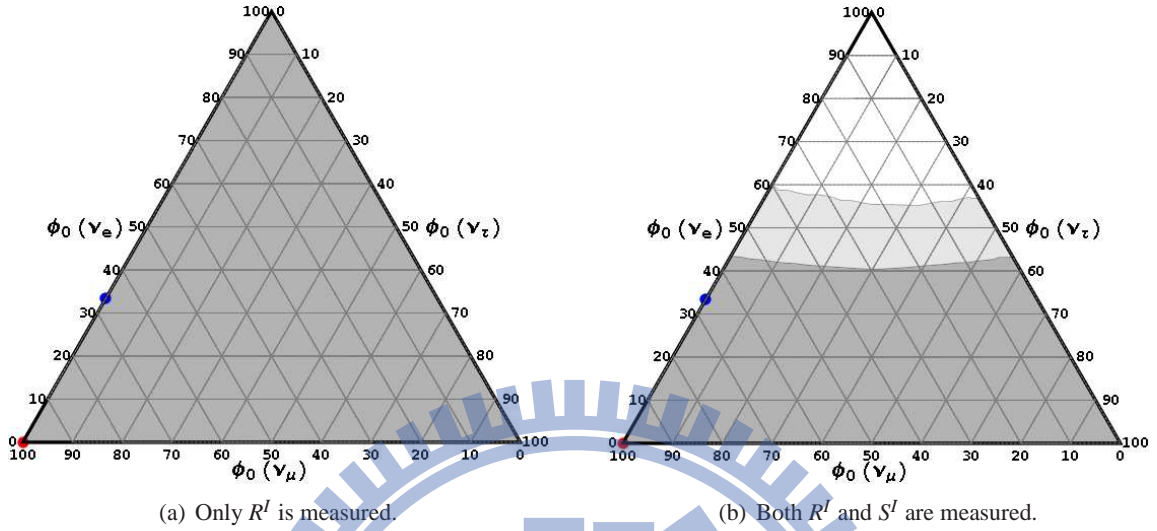


Figure 2.21: The reconstructed ranges for muon-damped source with 200 events and neutrino energy below 33.3 PeV. The range for possibly measured flavor ratio is cut off at 99.7%. The dark and light shades area denote  $1\sigma$  and  $3\sigma$  reconstructed ranges.

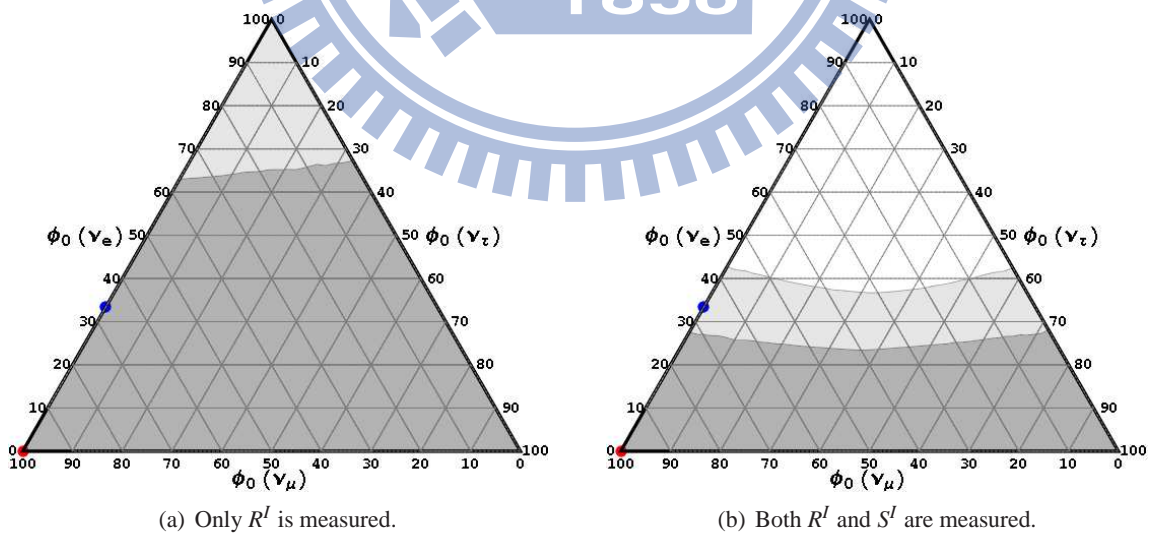


Figure 2.22: The reconstructed ranges for muon-damped source with 200 events and neutrino energy below 33.3 PeV. The range for possibly measured flavor ratio is cut off at 68.2%. The dark and light shades area denote  $1\sigma$  and  $3\sigma$  reconstructed ranges.

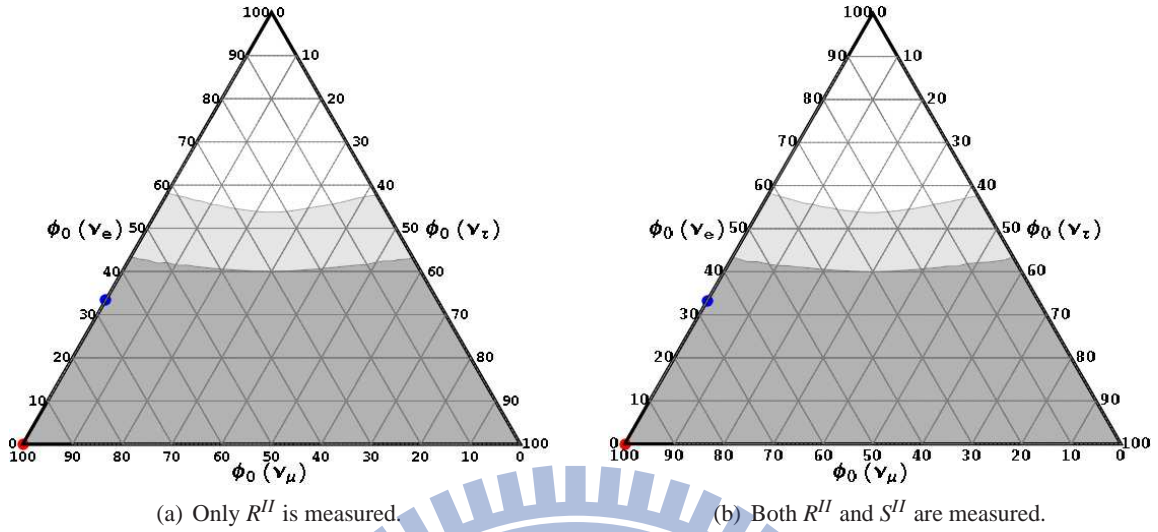


Figure 2.23: The reconstructed ranges for muon-damped source with 200 events and neutrino energy above 33.3 PeV. The range for possibly measured flavor ratio is cut off at 99.7%. The dark and light shades area denote  $1\sigma$  and  $3\sigma$  reconstructed ranges.

(15.48 – 16.34)%. The values of mixing angles are same as Table 2.5. The left panel in Fig. 2.24 shows the reconstructed neutrino flavor ratios for an input muon-damped source by measuring  $R^{II}$  only. The pion source can be ruled out even at  $1\sigma$  level. The right panel shows the reconstructed neutrino flavor ratios for an input pion source by measuring both  $R^{II}$  and  $S^{II}$ . The pion source can be ruled out even at  $1\sigma$  level too.

### 2.6.2.3 Summary of the Reconstructed Neutrino Flavor Ratios with 200 Events

Our studies show that thee input source cannot be distinguished from the other well-known source in  $3\sigma$  level with 200 events. The result is similar to Section.2.5.  $R^{II}$  is more efficient than  $R^I$  for reducing the source uncertainty. The pion source can be ruled out at  $1\sigma$  level with the muon-damped source as the true source.

### 2.6.3 The Flavor Ratios on the Earth from Pion Source with 400 Events

The neutrino flavor ratio on the Earth from pion source is  $\phi_\pi(\nu_e) : \phi_\pi(\nu_\mu) : \phi_\pi(\nu_\tau) = 0.35 : 0.33 : 0.32$ . This result only considers the best-fit values of mixing angles, and this flavor ratio has been shown in Fig. 2.2(a). This flavor ratio also represent the probability for observing each neutrino flavor in s single event. In this section, each flavor ratio is determined by 400 events with

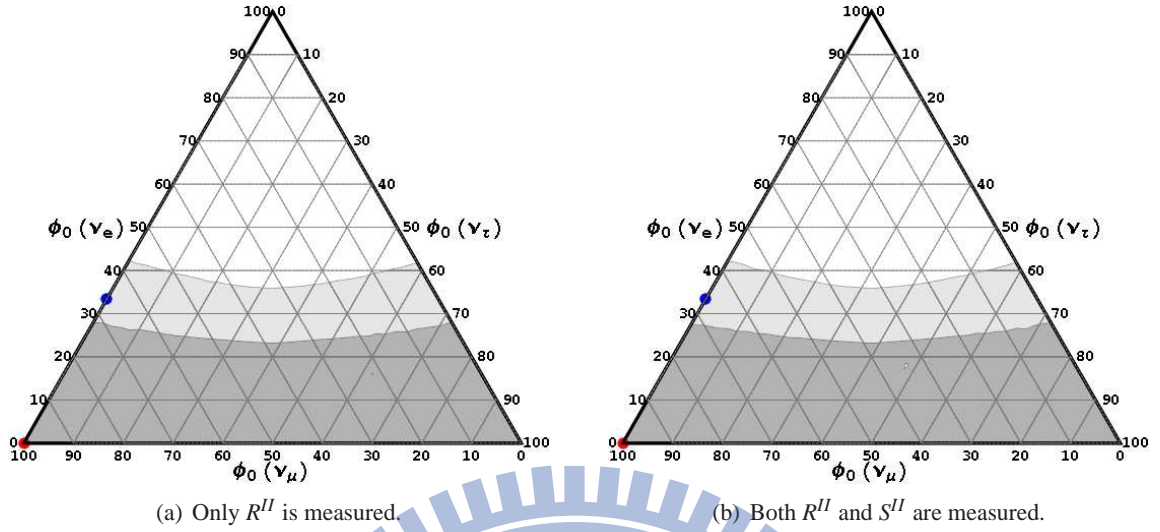


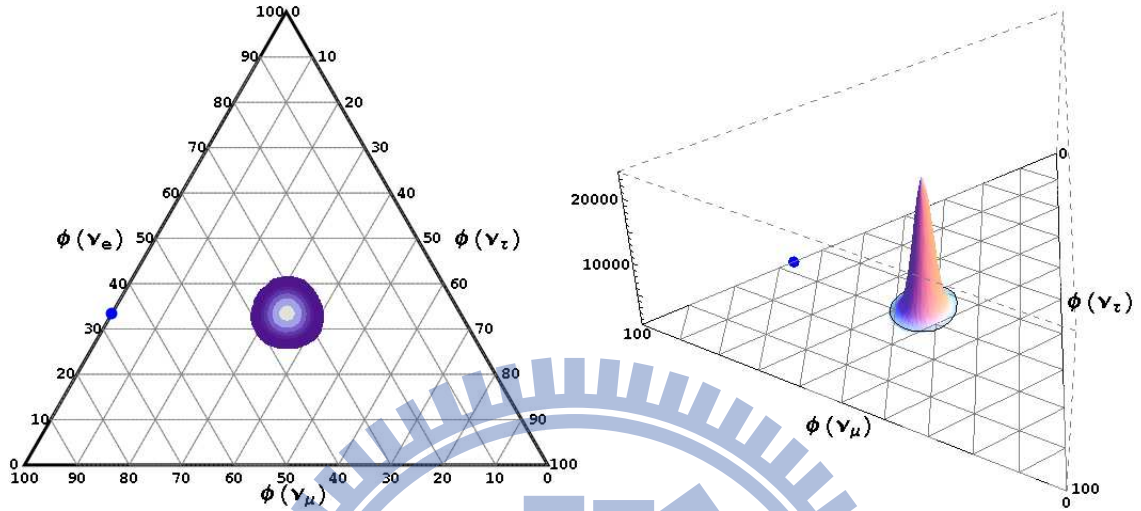
Figure 2.24: The reconstructed ranges for muon-damped source with 200 events and neutrino energy above 33.3 PeV. The range for possibly measured flavor ratio is cut off at 68.2%. The dark and light shades area denote  $1\sigma$  and  $3\sigma$  reconstructed ranges.

Monte-Carlo method. Fig. 2.15 shows the distributions of flavor ratios on the Earth by Monte-Carlo method. The distribution of flavor ratios is formed by repeating 10 million experiments and the long tail of distribution is cut off at 99.7% and 68.2%.

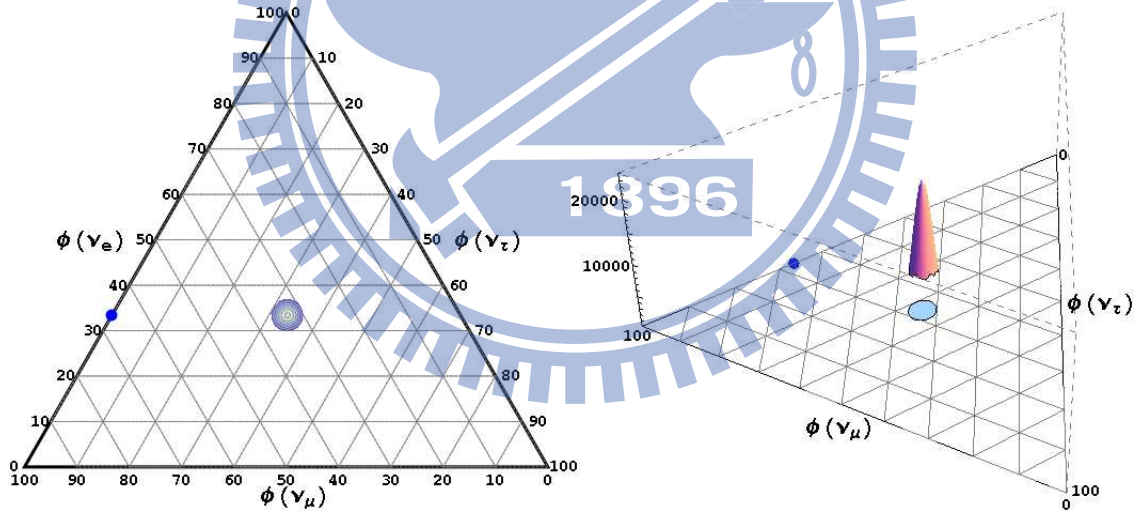
### 2.6.3.1 The Reconstructed Neutrino Flavor Ratios at Low Energy, $E_\nu \leq 33.3$ PeV

In 99.7% cut-off case, the distribution leads to  $\Delta R^I/R^I = (10.16 - 11.51)\%$  and  $\Delta S^I/S^I = (11.57 - 13.06)\%$ . The values of mixing angles are same as Table 2.5. The left panel in Fig. 2.26 shows the reconstructed neutrino flavor ratios for an input pion source by measuring  $R^I$  only. The muon-damped source cannot be ruled out even at  $1\sigma$  level. The right panel shows the reconstructed neutrino flavor ratios for an input pion source by measuring both  $R^I$  and  $S^I$ . The muon-damped source cannot be ruled out even at  $1\sigma$  level too.

In 68.2% cut-off case, the distribution leads to  $\Delta R^I/R^I = (10.39 - 10.96)\%$  and  $\Delta S^I/S^I = (11.91 - 12.55)\%$ . The values of mixing angles are same as Table 2.5. The left panel in Fig. 2.27 shows the reconstructed neutrino flavor ratios for an input pion source by measuring  $R^I$  only. The muon-damped source cannot be ruled out even at  $1\sigma$  level. The right panel shows the reconstructed neutrino flavor ratios for an input pion source by measuring both  $R^I$  and  $S^I$ . The muon-damped source can be ruled out even at  $1\sigma$  level.



(a) The contour at the left plot denote the boundary of flavor ratios. The right plot shows the distribution of the flavor ratios. The distribution leads  $\Delta R^I/R^I = (10.16 - 11.57)\%$  and  $\Delta S^I/S^I = (11.57 - 13.06)\%$  with  $E_\nu < 33$  PeV. This distribution also leads  $\Delta R^{II}/R^{II} = (10.14 - 11.47)\%$  and  $\Delta S^{II}/S^{II} = (11.59 - 13.09)\%$  with  $E_\nu > 33$  PeV.



(b) The contour at the left plot denotes the boundary of flavor ratios. The right plot shows the distribution of the flavor ratios. The distribution leads  $\Delta R^I/R^I = (10.39 - 10.96)\%$  and  $\Delta S^I/S^I = (11.91 - 12.55)\%$  with  $E_\nu < 33$  PeV. This distribution also leads  $\Delta R^{II}/R^{II} = (10.36 - 10.91)\%$  and  $\Delta S^{II}/S^{II} = (11.95 - 12.60)\%$  with  $E_\nu > 33$  PeV.

Figure 2.25: The distribution of neutrino flavor ratio on the Earth from pion source for 400 events. Each flavor ratio on the ternary plot is generated by 400 events. There are 10 million flavor ratios generated on the ternary plot, which form the distribution of flavor ratios. The blue point denotes the original flavor ratio of pion source. In panel (a), the distribution of flavor ratios is cut off at 99.7%. In panel (b), the distribution of flavor ratios is cut off at 68.2%.



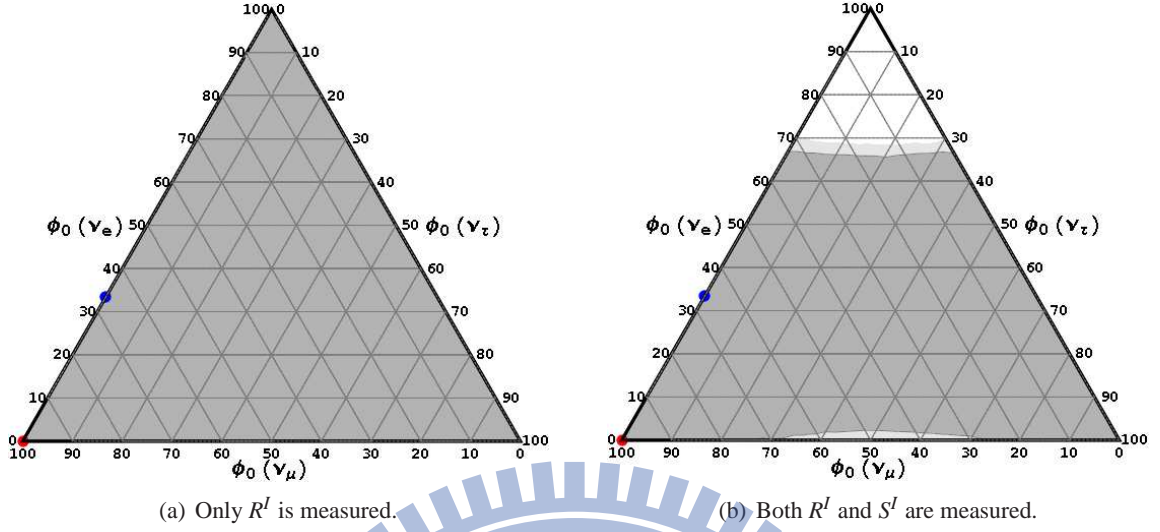


Figure 2.26: The reconstructed ranges for pion source with 400 events below 33.3 PeV. The range for possibly measured flavor ratio is cut off at 99.7%. The dark and light shades area denote  $1\sigma$  and  $3\sigma$  reconstructed ranges.

### 2.6.3.2 The Reconstructed Neutrino Flavor Ratios at High Energy, $E_\nu \geq 33.3$ PeV

In 99.7% cut-off case, the distribution leads to  $\Delta R^{II}/R^{II} = (10.14 - 11.47)\%$  and  $\Delta S^{II}/S^{II} = (11.59 - 13.09)\%$ . The values of mixing angles are same as Table 2.5. The left panel in Fig. 2.28 shows the reconstructed neutrino flavor ratios for an input pion source by measuring  $R^{II}$  only. The muon-damped source cannot be ruled out even at  $1\sigma$  level. The right panel shows the reconstructed neutrino flavor ratios for an input pion source by measuring both  $R^{II}$  and  $S^{II}$ . The muon-damped source cannot be ruled out even at  $1\sigma$  level too.

In 68.2% cut-off case, the distribution leads to  $\Delta R^{II}/R^{II} = (10.36 - 10.91)\%$  and  $\Delta S^{II}/S^{II} = (11.95 - 12.60)\%$ . The values of mixing angles are same as Table 2.5. The left panel in Fig. 2.29 shows the reconstructed neutrino flavor ratios for an input pion source by measuring  $R^{II}$  only. The muon-damped source can be ruled out even at  $1\sigma$  level. The right panel shows the reconstructed neutrino flavor ratios for an input pion source by measuring  $R^{II}$  and  $S^{II}$ . The muon-damped source can be ruled out even at  $1\sigma$  level too.

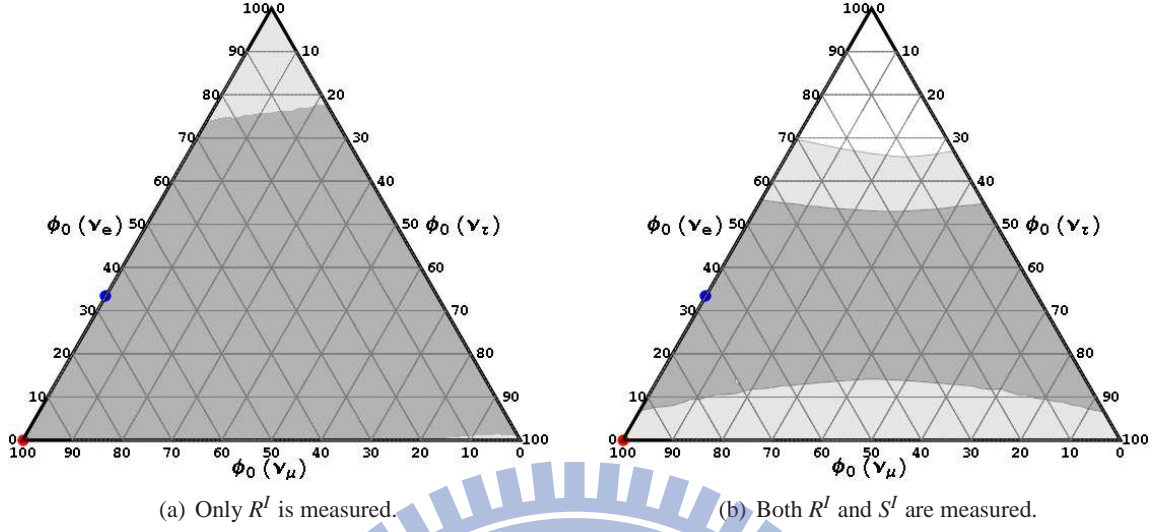


Figure 2.27: The reconstructed ranges for pion source with 400 events below 33.3 PeV. The range for possibly measured flavor ratio is cut off at 68.2%. The dark and light shades area denote  $1\sigma$  and  $3\sigma$  reconstructed ranges.

## 2.6.4 The Flavor Ratios on the Earth from the Muon-damped Source with 400 Events

The neutrino flavor ratio on the Earth from pion source is  $\phi_\mu(\nu_e) : \phi_\mu(\nu_\mu) : \phi_\mu(\nu_\tau) = 0.24 : 0.37 : 0.39$ . This result only considers the best-fit values of mixing angles, and this flavor ratio has been shown in Fig. 2.2(a). This flavor ratio also represent the probability for observing each neutrino flavor in a single event. In this section, each flavor ratio is determined by 400 events in Monte-Carlo method. Fig. 2.30 show the distributions of flavor ratios on the Earth by Monte-Carlo method. The distribution of flavor ratios is formed by repeating 10 million experiments. The long tail of distribution is cut off at 99.7% and 68.2%.

### 2.6.4.1 The Reconstructed Neutrino Flavor Ratios at Low Energy, $E_\nu \leq 33.3$ PeV

In 99.7% cut-off case, the distribution leads to  $\Delta R^I/R^I = (10.01 - 10.79)\%$  and  $\Delta S^I/S^I = (12.43 - 15.43)\%$ . The values of mixing angles are same as Table 2.5. The left panel in Fig. 2.31 shows the reconstructed neutrino flavor ratios for an input muon-damped source by measuring  $R^I$  only. The pion source cannot be ruled out even at  $1\sigma$  level. The right panel shows the reconstructed neutrino flavor ratios for an input muon-damped source by measuring both  $R^I$  and  $S^I$ . The pion source can be ruled out even at  $1\sigma$  level too.

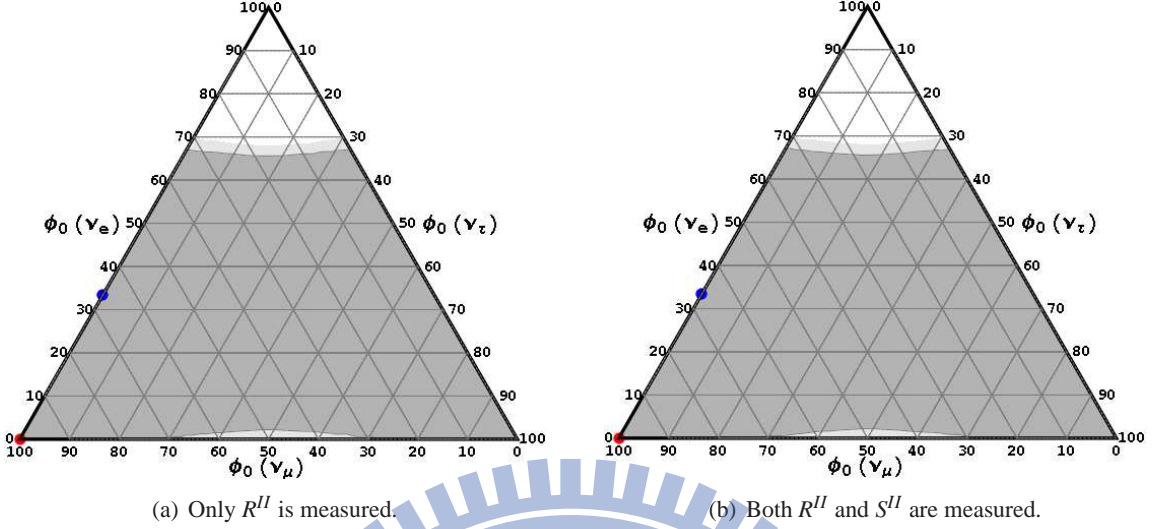


Figure 2.28: The reconstructed ranges for pion source with 400 events and neutrino energy above 33.3 PeV. The range for possibly measured flavor ratio is cut off at 99.7%. The dark and light shades area denote  $1\sigma$  and  $3\sigma$  reconstructed ranges.

In 68.2% cut-off case, the distribution leads to  $\Delta R^I/R^I = (10.09 - 10.43)\%$  and  $\Delta S^I/S^I = (13.0 - 14.22)\%$ . The values of mixing angles are same as Table 2.5. The left panel in Fig. 2.32 shows the reconstructed neutrino flavor ratios for an input muon-damped source by measuring  $R^I$  only. The pion source cannot be ruled out even at  $1\sigma$  level. The right panel shows the reconstructed neutrino flavor ratios for an input muon-damped source by measuring both  $R^I$  and  $S^I$ . The pion source can be ruled out even at  $3\sigma$  level.

#### 2.6.4.2 The Reconstructed Neutrino Flavor Ratios at High Energy, $E_\nu \geq 33.3$ PeV

In 99.7% cut-off case, the distribution leads to  $\Delta R^{II}/R^{II} = (11.10 - 14.4)\%$  and  $\Delta S^{II}/S^{II} = (10.78 - 11.78)\%$ . The values of mixing angles are same as Table 2.5. The left panel in Fig. 2.33 shows the reconstructed neutrino flavor ratios for an input muon-damped source by measuring  $R^{II}$  only. The pion source can be ruled out even at  $1\sigma$  level. The right panel shows the reconstructed neutrino flavor ratios for an input muon-damped source by measuring both  $R^{II}$  and  $S^{II}$ . The pion source can be ruled out even at  $1\sigma$  level too.

In 68.2% cut-off case, the distribution leads to  $\Delta R^{II}/R^{II} = (11.70 - 13.08)\%$  and  $\Delta S^{II}/S^{II} = (11.02 - 11.45)\%$ . The values of mixing angles are same as Table 2.5. The left panel in Fig. 2.34 shows the reconstructed neutrino flavor ratios for an input muon-damped source by measuring  $R^{II}$

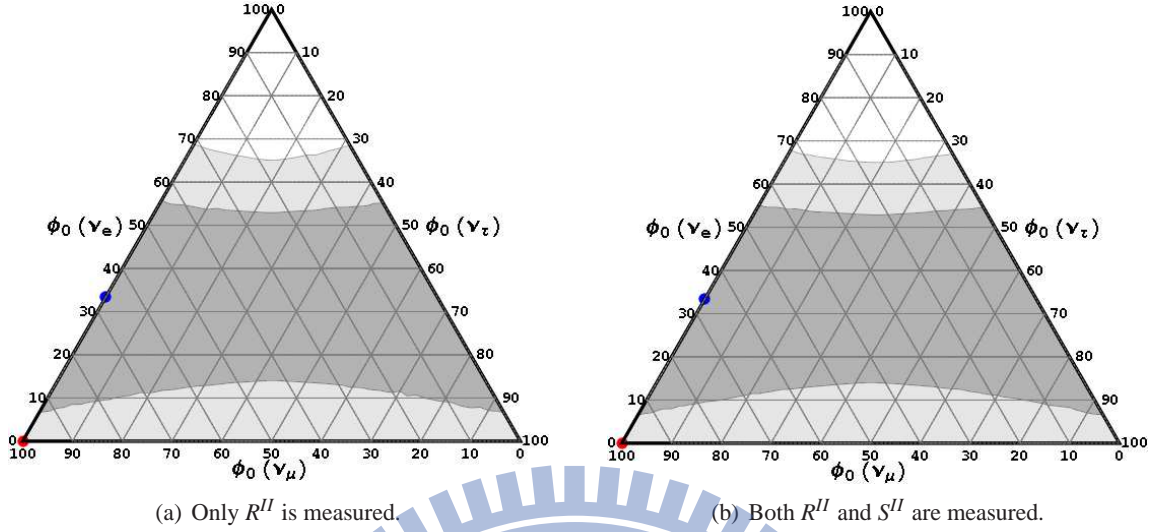
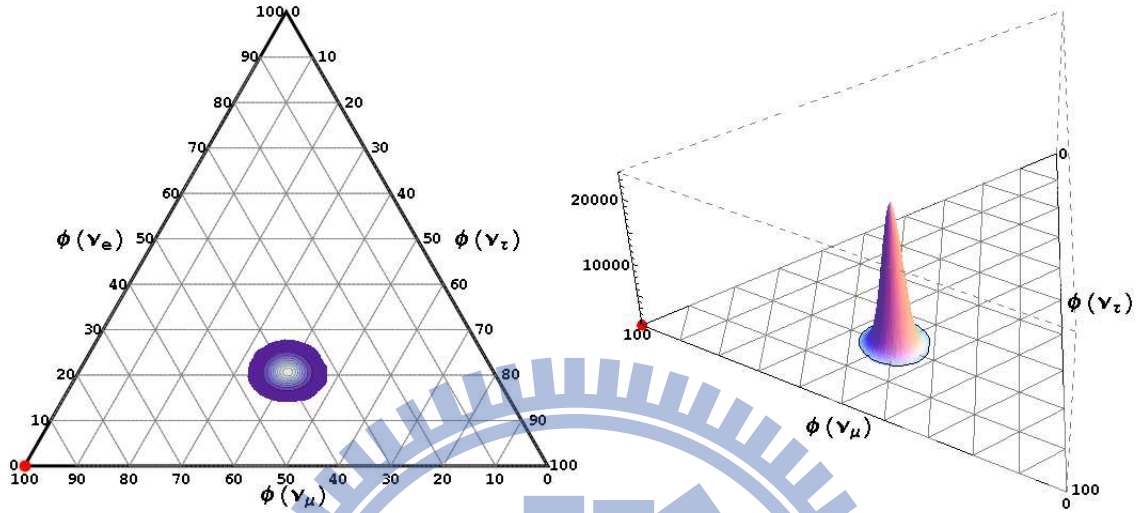


Figure 2.29: The reconstructed ranges for pion source with 400 events and neutrino energy above 33.3 PeV. The range for possibly measured flavor ratio is cut off at 68.2%. The dark and light shades area denote  $1\sigma$  and  $3\sigma$  reconstructed ranges.

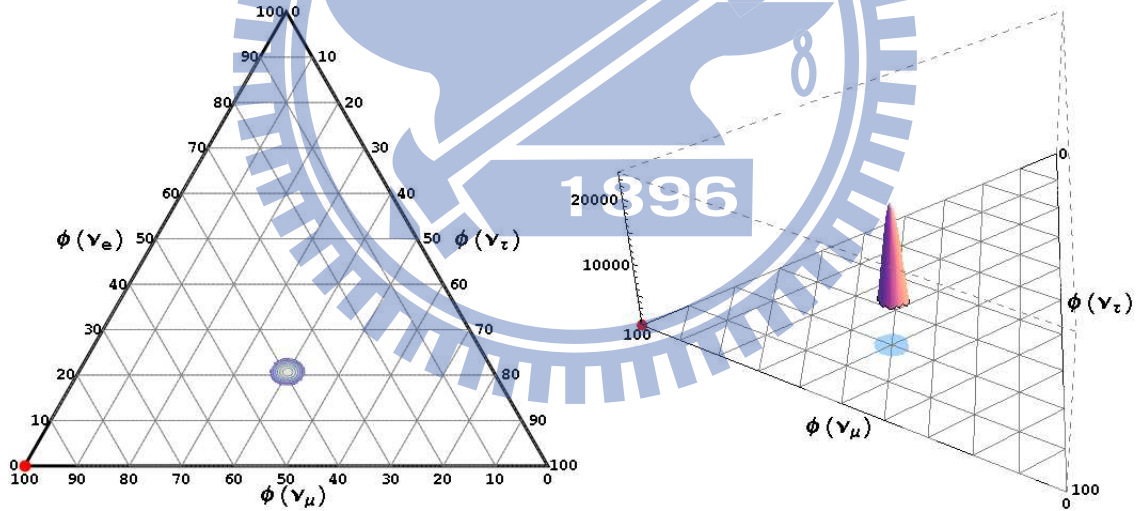
only. The pion source can be ruled out even at  $1\sigma$  level. The right panel shows the reconstructed neutrino flavor ratios for an input muon-damped source by measuring both  $R^{II}$  and  $S^{II}$ . The pion source can be ruled out even at  $3\sigma$  level too.

### 2.6.4.3 Summary of the Reconstructed Neutrino Flavor Ratios with 400 Events

Our studies show that the most input source cannot be distinguished from the other well-known source in  $1\sigma$  level with 400 events, The  $R^{II}$  is more efficient than  $R^I$  for reducing the source uncertainty. In 68.2% cut-off case, the true input source can be separated from other source in  $3\sigma$  level by measuring both the  $R^I$  and  $S^I$ . The true input source also can be separated from other source in  $3\sigma$  level by measuring the  $R^{II}$  only in 68.2% cut-off case. The results show 400 observed neutrino events is critical condition to distinguish the pion and muon-damped source by measuring both  $R^I$  and  $S^I$  at low energy. At high energy, 400 observed neutrino events is critical condition to distinguish the pion and muon-damped source by measuring only  $R^{II}$  parameter.



(a) The contour at the left plot denotes the boundary of flavor ratios. The right plot shows the distribution of the flavor ratios. The distribution leads  $\Delta R^I/R^I = (10.01 - 10.79)\%$  and  $\Delta S^I/S^I = (12.43 - 15.43)\%$  with  $E_\nu < 33$  PeV. This distribution also leads  $\Delta R^{II}/R^{II} = (11.10 - 14.4)\%$  and  $\Delta S^{II}/S^{II} = (10.78 - 11.78)\%$  with  $E_\nu > 33$  PeV.



(b) The contour at the left plot denotes the boundary of flavor ratios. The right plot shows the distribution of the flavor ratios. The distribution leads  $\Delta R^I/R^I = (10.09 - 10.43)\%$  and  $\Delta S^I/S^I = (13.0 - 14.22)\%$  with  $E_\nu < 33$  PeV. This distribution also leads  $\Delta R^{II}/R^{II} = (11.70 - 13.08)\%$  and  $\Delta S^{II}/S^{II} = (11.02 - 11.45)\%$  with  $E_\nu > 33$  PeV.

Figure 2.30: The distribution of neutrino flavor ratio on the Earth from muon-damped source for 400 events. Each flavor ratio on the ternary plot is generated by 400 events. There are 10 million flavor ratios generated on the ternary plot, which form the distribution of flavor ratios. The red point denotes the original flavor ratio of muon-damped source. In panel (a), the distribution of flavor ratios is cut off at 99.7%. In panel (b), the distribution of flavor ratios is cut off at 68.2%.

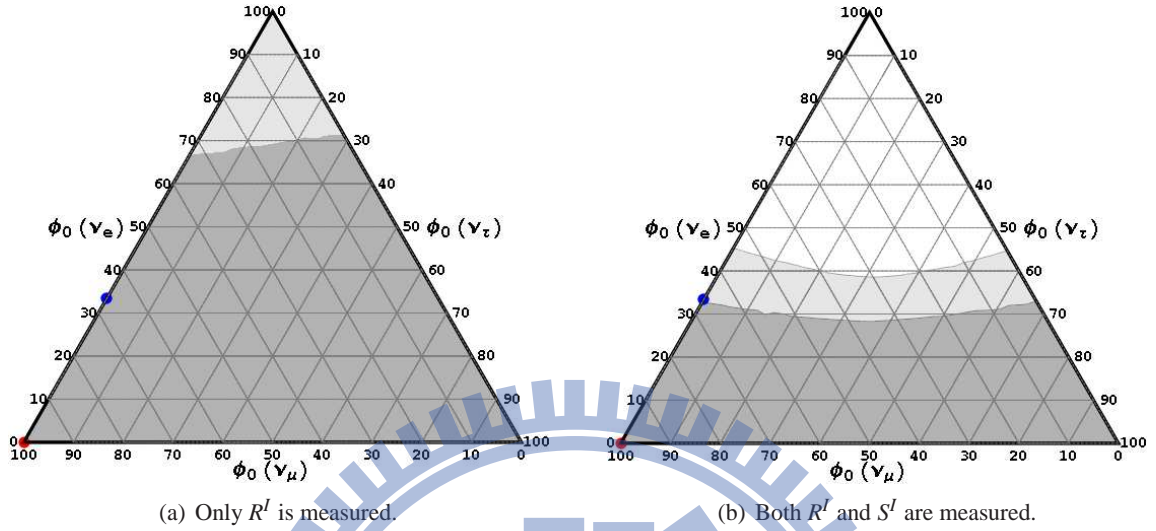


Figure 2.31: The reconstructed ranges for muon-damped source with 400 events below 33.3 PeV. The range for possibly measured flavor ratio is cut off at 99.7%. The dark and light shades area denote  $1\sigma$  and  $3\sigma$  reconstructed ranges.

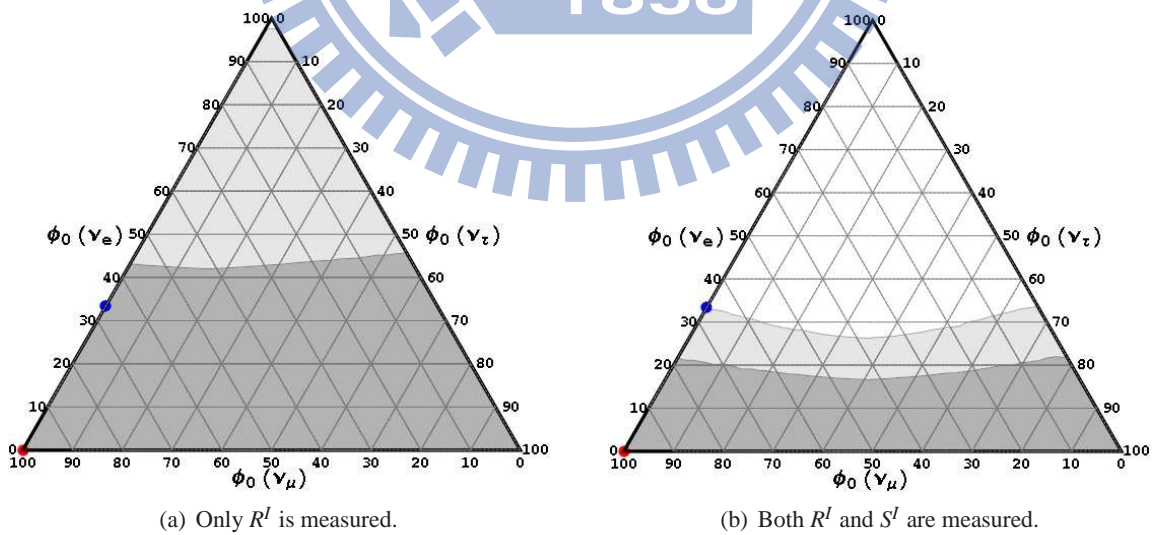


Figure 2.32: The reconstructed ranges for muon-damped source with 400 events below 33.3 PeV. The range for possibly measured flavor ratio is cut off at 68.2%. The dark and light shades area denote  $1\sigma$  and  $3\sigma$  reconstructed ranges.

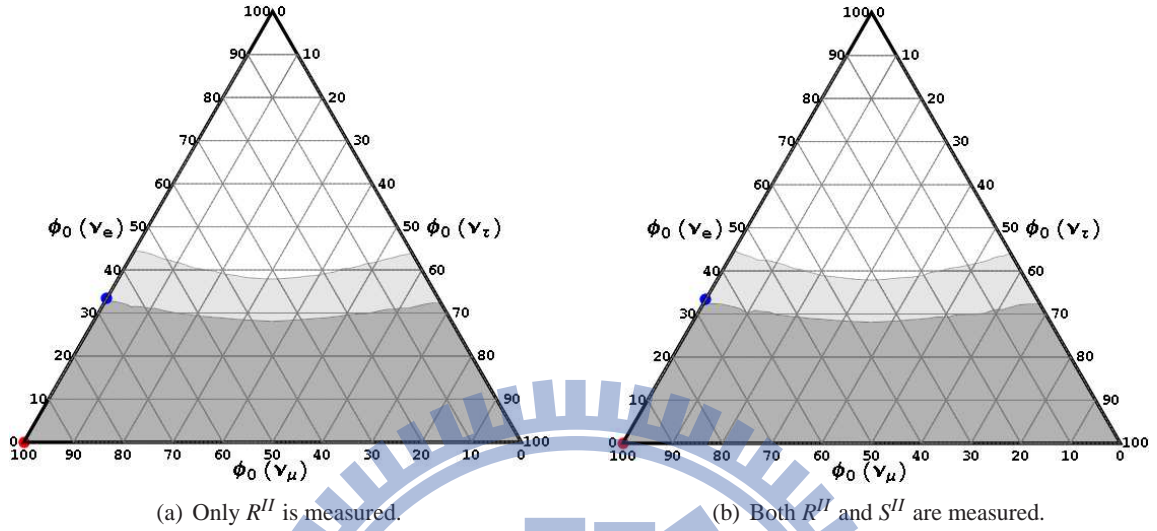


Figure 2.33: The reconstructed ranges for muon-damped source with 400 events above 33.3 PeV. The range for possibly measured flavor ratio is cut off at 99.7%. The dark and light shades area denote  $1\sigma$  and  $3\sigma$  reconstructed ranges.

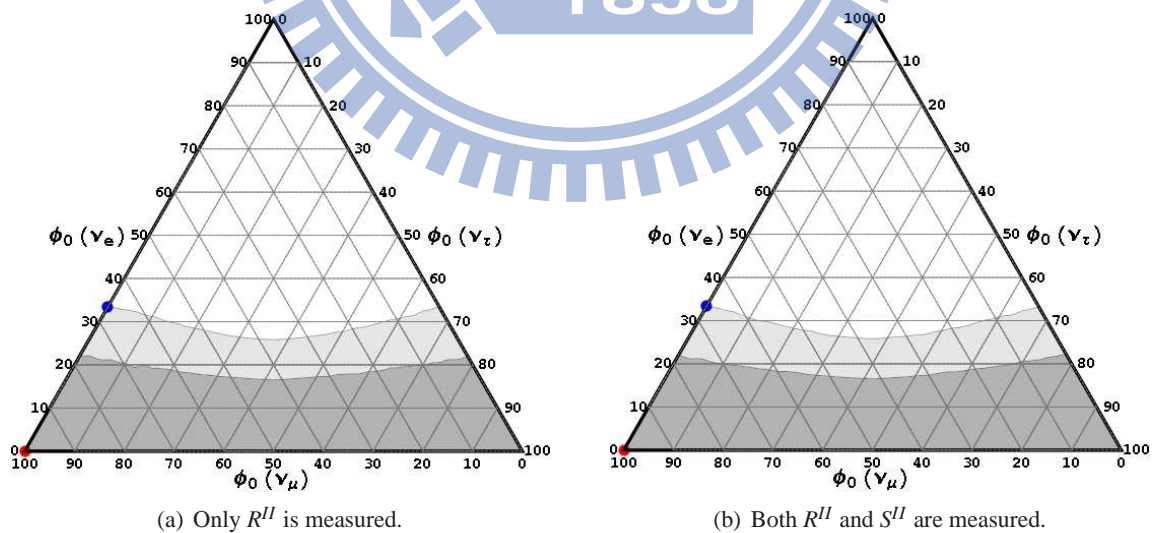


Figure 2.34: The reconstructed ranges for muon-damped source with 400 events above 33.3 PeV. The range for possibly measured flavor ratio is cut off at 68.2%. The dark and light shades area denote  $1\sigma$  and  $3\sigma$  reconstructed ranges.

## Chapter 3

# Flavor Ratios on the Earth from Neutrino Decay

The flavor ratio of astrophysical neutrinos observed on the Earth depend on both the initial flavor ratio at the source and flavor mixing mechanisms during the propagation of these neutrinos. In section 2.2, Fig. 2.2 shows the neutrino flavor ratios on the Earth from pion source and muon-damped source. In this chapter, we consider more general source,  $\phi_0(\nu_e) : \phi_0(\nu_\mu) : \phi_0(\nu_\tau) = \alpha : \beta : 1 - \alpha - \beta$ , with  $\alpha > 0$ ,  $\beta > 0$  and  $\alpha + \beta < 1$ , and neutrino decay mechanisms. Fig. 3.1 shows the ranges for neutrino flavor ratios on the Earth resulting from standard neutrino oscillation. The values of mixing angles are same as set 1 in Table 2.5 in Section 2.2.

### 3.1 $Q$ Matrix Representation

#### 3.1.1 $Q$ Matrix Representation for Oscillations of Astrophysical Neutrinos

The effect of  $P^{\text{osc}}$  on flavor transition of astrophysical neutrinos can be better understood by diagonalizing  $P^{\text{osc}}$ . In the tri-bimaximal limit of mixing angles, we obtain  $P^{\text{osc}} \rightarrow P_0^{\text{osc}} = \mathbf{A}Q_0^{\text{osc}}\mathbf{A}^{-1}$  with [15]



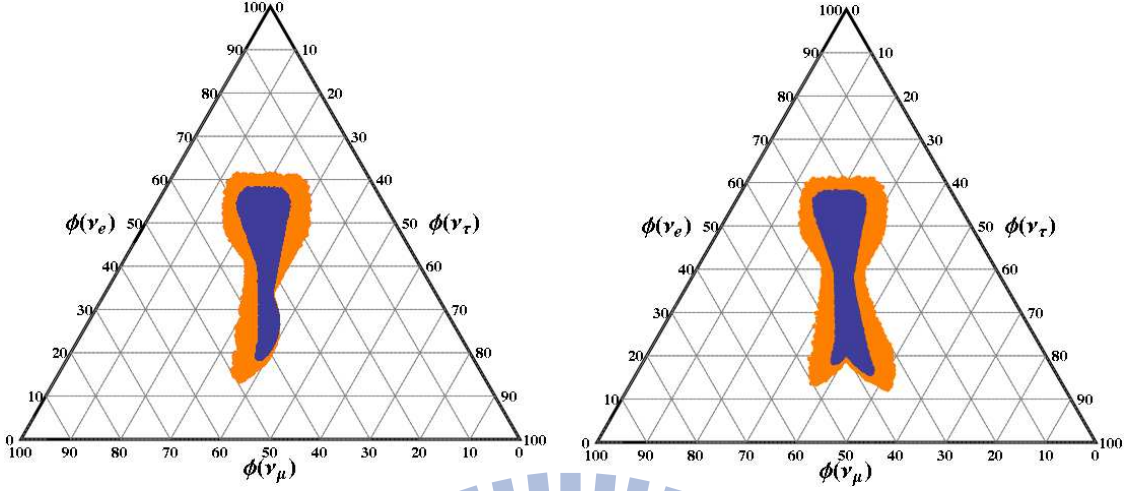


Figure 3.1: The ranges for the neutrino flavor ratios on the Earth resulting from standard neutrino oscillation. The left panel shows the range of neutrino flavor ratios from the source flavor ratios,  $\phi_0(\nu_e) : \phi_0(\nu_\mu) : \phi_0(\nu_\tau) = \alpha : 1 - \alpha : 0$ , with  $0 \leq \alpha \leq 1$ . The violet and orange colors correspond the  $1\sigma$  and  $3\sigma$  level of neutrino mixing angles respectively. The right panel shows the range of neutrino flavor ratios from the source flavor ratios,  $\phi_0(\nu_e) : \phi_0(\nu_\mu) : \phi_0(\nu_\tau) = \alpha : \beta : 1 - \alpha - \beta$ , with  $\alpha > 0$ ,  $\beta > 0$  and  $\alpha + \beta \leq 1$ . The violet and orange colors correspond the  $1\sigma$  and  $3\sigma$  level of neutrino mixing angles respectively. The values of mixing angles are same as the set 1 in Table 2.5.

$$Q_0^{\text{osc}} = \begin{pmatrix} 1 & 0 & 0 \\ 0 & 0 & 0 \\ 0 & 0 & 1/3 \end{pmatrix}, \quad (3.1)$$

and

$$\mathbf{A} = \begin{pmatrix} 1 & 0 & 2 \\ 1 & -1 & -1 \\ 1 & 1 & -1 \end{pmatrix}, \quad (3.2)$$

where each column of this matrix corresponds to an eigenvector of  $P_0^{\text{osc}}$ . As we shall see later, for a general flavor transition matrix  $P$ , it remains useful to write  $P = \mathbf{A}Q\mathbf{A}^{-1}$  with the same matrix  $\mathbf{A}$ , although the resulting  $Q$  might not be diagonal any more. Let us first illustrate this with  $P^{\text{osc}}$  evaluated at general  $\theta_{13}$  and  $\theta_{23}$  while keeping  $\sin^2 \theta_{12} = 1/3$ . In this case  $P^{\text{osc}} = P_0^{\text{osc}} + P_1^{\text{osc}} + \dots$  where  $P_1^{\text{osc}}$  is the leading order correction in powers of  $\cos 2\theta_{23}$  and  $\sin \theta_{13}$ .

We have

$$P_1^{\text{osc}} = \begin{pmatrix} 0 & \varepsilon & -\varepsilon \\ \varepsilon & -\varepsilon & 0 \\ -\varepsilon & 0 & \varepsilon \end{pmatrix}. \quad (3.3)$$

where  $\varepsilon = 2 \cos 2\theta_{23}/9 + \sqrt{2} \sin \theta_{13} \cos \delta/9$  with  $\delta$  the  $CP$  phase. Taking into account the correction term  $P_1^{\text{osc}}$ , we obtain  $Q^{\text{osc}} = Q_0^{\text{osc}} + Q_1^{\text{osc}}$  with

$$Q_1^{\text{osc}} = \mathbf{A}^{-1} P_1^{\text{osc}} \mathbf{A} = \begin{pmatrix} 0 & 0 & 0 \\ 0 & 0 & -3\varepsilon \\ 0 & -\varepsilon & 0 \end{pmatrix}. \quad (3.4)$$

Therefore  $Q^{\text{osc}}$  reads

$$Q^{\text{osc}} = \mathbf{A}^{-1} P^{\text{osc}} \mathbf{A} = \begin{pmatrix} 1 & 0 & 0 \\ 0 & 0 & -3\varepsilon \\ 0 & -\varepsilon & 1/3 \end{pmatrix}. \quad (3.5)$$

We note that  $Q_0^{\text{osc}}$  ( $P_0^{\text{osc}}$ ) preserves the  $\nu_\mu - \nu_\tau$  symmetry while  $Q_1^{\text{osc}}$  ( $P_1^{\text{osc}}$ ) breaks it. The exact  $\nu_\mu - \nu_\tau$  symmetry amounts to the condition  $|U_{\mu i}| = |U_{\tau i}|$  for  $i = 1, 2, 3$  [25, 26]. This condition can be realized by having both  $\sin^2 \theta_{23} = 1/2$  and  $\sin \theta_{13} \cos \delta = 0$ , which are what we have taken for  $P_0^{\text{osc}}$ . The condition  $|U_{\mu i}| = |U_{\tau i}|$  leads to  $P_{0,e\mu}^{\text{osc}} = P_{0,e\tau}^{\text{osc}}$ ,  $P_{0,\mu e}^{\text{osc}} = P_{0,\tau e}^{\text{osc}}$  and  $P_{0,\mu\tau}^{\text{osc}} = P_{0,\tau\mu}^{\text{osc}} = P_{0,\mu\mu}^{\text{osc}} = P_{0,\tau\tau}^{\text{osc}}$  as can be seen from Eq. (2.6). With these relations and  $Q_0^{\text{osc}} = \mathbf{A}^{-1} P_0^{\text{osc}} \mathbf{A}$ , it can be explicitly shown that both the second row and the second column of  $Q_0^{\text{osc}}$  vanish. This is indeed seen in Eq. (3.1).

Since we have chosen  $Q^{\text{osc}}$  to describe the oscillation effect, it is appropriate to parametrize the source flavor composition in this new basis such that

$$\Phi_0 = \frac{1}{3} \mathbf{V}_1 + a \mathbf{V}_2 + b \mathbf{V}_3, \quad (3.6)$$

where  $\mathbf{V}_1$ ,  $\mathbf{V}_2$  and  $\mathbf{V}_3$  are vectors representing each column of  $\mathbf{A}$ , *i.e.*,  $\mathbf{V}_1 = (1, 1, 1)^T$ ,  $\mathbf{V}_2 = (0, -1, 1)^T$  and  $\mathbf{V}_3 = (2, -1, -1)^T$ . The ranges for  $a$  and  $b$  are  $-1/3 + b \leq a \leq 1/3 - b$  and  $-1/6 \leq b \leq 1/3$ . The pion source and the muon-damped source correspond to  $(a, b) =$

$(-1/3, 0)$  and  $(a, b) = (-1/2, -1/6)$  respectively. In general, a source with a negligible  $\nu_\tau$  flux corresponds to  $a = -1/3 + b$ . The vector  $\mathbf{V}_1$  gives the normalization of the neutrino flux since the sum of the elements in  $\mathbf{V}_1/3$  is equal to unity while the sums of the elements in  $\mathbf{V}_2$  and  $\mathbf{V}_3$  are both equal to zero. The vector  $b\mathbf{V}_3$  determines the electron neutrino flux  $\phi_{0,e}$  or equivalently the sum of muon and tau neutrino fluxes  $\phi_{0,\mu} + \phi_{0,\tau}$ . However this vector preserves the difference  $\phi_{0,\mu} - \phi_{0,\tau}$ . Finally the vector  $a\mathbf{V}_2$  determines  $\phi_{0,\mu} - \phi_{0,\tau}$  while preserves  $\phi_{0,\mu} + \phi_{0,\tau}$  or equivalently  $\phi_{0,e}$ . The neutrino flux on the Earth is given by

$$\Phi = (\mathbf{A}Q^{\text{osc}}\mathbf{A}^{-1})\Phi_0 = \kappa\mathbf{V}_1 + \rho\mathbf{V}_2 + \lambda\mathbf{V}_3, \quad (3.7)$$

with  $\kappa = 1/3$ ,  $\rho = -3\epsilon b$  and  $\lambda = b/3 - \epsilon a$ .

### 3.1.2 $Q$ Matrix Representation for General Flavor Transitions of Astrophysical Neutrinos

For a general flavor transition mechanism, the final state on the Earth may contain particles other than usual three generation of neutrinos, although these particles are assumed to be absent at the astrophysical source. However, since we are only interested in detecting ordinary neutrino states, a  $3 \times 3$  matrix is sufficient to relate the initial flavor composition to the one observed on the Earth. This amounts to having a general matrix  $Q$  such that the general flavor transition matrix  $P$  is given by  $P = \mathbf{A}Q\mathbf{A}^{-1}$ . In this case, we replace  $Q^{\text{osc}}$  in Eq. (3.7) by a general matrix  $Q$  and obtain

$$\begin{aligned} \kappa &= \frac{1}{3}Q_{11} + aQ_{12} + bQ_{13}, \\ \rho &= \frac{1}{3}Q_{21} + aQ_{22} + bQ_{23}, \\ \lambda &= \frac{1}{3}Q_{31} + aQ_{32} + bQ_{33}. \end{aligned} \quad (3.8)$$

We also note from Eq. (3.7) that the flux of each neutrino flavor is given by

$$\phi_e = \kappa + 2\lambda, \quad \phi_\mu = \kappa - \rho - \lambda, \quad \phi_\tau = \kappa + \rho - \lambda, \quad (3.9)$$

with the normalization  $\phi_e + \phi_\mu + \phi_\tau = 3\kappa$ . Since we have chosen the normalization  $\phi_{0,e} + \phi_{0,\mu} + \phi_{0,\tau} = 1$  for the neutrino flux at the source, the conservation of total neutrino flux during propagation corresponds to  $\kappa = 1/3$ . In general flavor transition models,  $\kappa$  could be less than  $1/3$  as a consequence of (ordinary) neutrino decaying into invisible states or oscillating into sterile neutrinos.

To continue our discussions, it is helpful to rewrite Eq. (3.9) as

$$\rho = (\phi_\tau - \phi_\mu)/2, \quad \lambda = \phi_e/3 - (\phi_\mu + \phi_\tau)/6. \quad (3.10)$$

It is clearly seen from Eq. (3.8) and Eq. (3.10) that, for fixed  $a$  and  $b$ , the first row of matrix  $Q$  determines the normalization of total neutrino flux reaching to the Earth, the second row of  $Q$  determines the breaking of  $\nu_\mu - \nu_\tau$  symmetry in the arrival neutrino flux, and the third row of  $Q$  determines the flux difference  $\phi_e - (\phi_\mu + \phi_\tau)/2$ .

### 3.2 Neutrino Decay Mechanisms

In neutrino decay mechanisms, we consider only two-body decay modes with three active neutrino flavors and assume the decays are complete. As discussed in Ref. [27], the probability transition matrix characterizing the the decay scenario is written in terms of PMNS matrix and corresponding branching ratios

$$P_{\alpha\beta}^{dec} = \sum_{i \text{ stable}} (|U_{\alpha i}|^2 + \sum_{j \text{ unstable}} |U_{\alpha j}|^2 \text{Br}_{j \rightarrow i}) |U_{\beta i}|^2, \quad (3.11)$$

where indices  $i$  and  $j$  denote mass eigenstates and  $\text{Br}_{i \rightarrow j}$  shows branching ratio for unstable state  $i$  decays to stable state  $j$ .  $\sum_f \text{Br}_{i \rightarrow j} = 1$  for  $i$  state fully decays to  $j$  state. In general,  $\sum_f \text{Br}_{i \rightarrow j} < 1$  and  $\text{Br}_{i \rightarrow \text{invisible}} = 1 - \sum_f \text{Br}_{i \rightarrow j}$  denotes the probability for  $i$  state fully decays to invisible states. The invisible states is invisible for neutrino detector. Those states could be unparticle states, Majorons *etc.* Table 3.1 lists all possibilities of decays with oscillation included for comparison.

type	Hierarchy	H	M	L	Scenarios	figure number	degeneracy
I					Oscillation	3.1	
II	Normal	3	2	1	Heaviest & middle decay	3.2a	3.8b
III	Inverted	2	1	3	Heaviest & middle decay	3.2b	3.7a
IV	Normal	3	2	1	Heaviest decay	3.3d	3.6b
V	Inverted	2	1	3	Heaviest decay	3.4d	3.5a
V	Normal	3	2	1	Middle decay	3.5a	3.4d
VI	Inverted	2	1	3	Middle decay	3.5b	3.6a
VI	Normal	3	2	1	Lightest decay to invisible	3.6a	3.5b
IV	Inverted	2	1	3	Lightest decay to invisible	3.6b	3.3d
III	Normal	3	2	1	Middle decay & Lightest	3.7a	3.2b
VII	Inverted	2	1	3	decay to invisible	3.7b	3.8a
VII	Normal	3	2	1	Heaviest decay & Lightest	3.8a	3.7b
II	Inverted	2	1	3	decay to invisible	3.8b	3.2a

Table 3.1: The neutrino decay and oscillation scenarios. The suffix ‘‘H’’, ‘‘M’’, and ‘‘L’’ label the heaviest, middle and lightest mass eigenstates. The number ‘‘1’’, ‘‘2’’ and ‘‘3’’ label  $\nu_1$ ,  $\nu_2$  and  $\nu_3$  mass eigenstates. The red numbers and black numbers correspond to the unstable and stable eigenstates respectively.

### 3.3 The Range of Neutrino Flavor Ratios on the Earth

#### 3.3.1 The Heaviest and Middle Mass Eigenstates decay to the Lightest and Invisible States.

##### 3.3.1.1 Normal Mass Hierarchy

The transition probability matrix for the heaviest mass and middle eigenstates decay to the lightest and invisible state in the normal mass hierarchy is written as

$$P_{\alpha\beta}^{dec} = (|U_{\alpha 1}|^2 + |U_{\alpha 3}|^2 Br_{3 \rightarrow 1} + |U_{\alpha 2}|^2 Br_{2 \rightarrow 1}) |U_{\beta 1}|^2 \quad (3.12)$$

where  $0 \leq Br_{3 \rightarrow 1} \leq 1$  and  $0 \leq Br_{2 \rightarrow 1} \leq 1$ . If the heaviest mass eigenstate only decays to invisible states,  $Br_{3 \rightarrow 1} = 0$ , Eq. (3.12) is identical to the case of the heaviest and lightest mass eigenstates decay to the middle and invisible state in the inverted mass hierarchy. Fig. 3.2(a) shows the range of flavor ratios on the Earth with source flavor ratios,  $\phi_0(\nu_e) : \phi_0(\nu_\mu) : \phi_0(\nu_\tau) = \alpha : \beta : 1 - \alpha - \beta$ . Comparing this result with the result of standard neutrino oscillation in Fig. 3.1(b), The overlapped region between those two cases is around  $\phi(\nu_e) \sim 0.6$ .

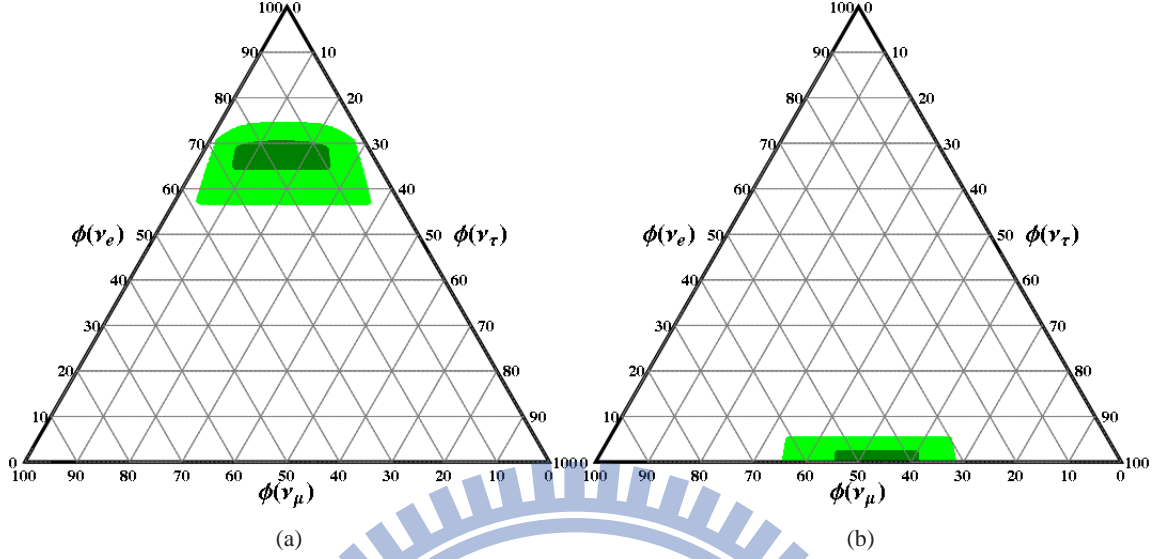


Figure 3.2: The range of flavor ratios on the Earth from the heaviest and middle mass eigenstates decay to the lightest mass eigenstate and invisible states. The final branching ratios of the heaviest and lightest mass eigenstates are  $Br_{H \rightarrow L} + Br_{H \rightarrow \text{invisible}} = 1$  and  $Br_{M \rightarrow L} + Br_{M \rightarrow \text{invisible}} = 1$ . Panel (a) shows the range of flavor ratios on the Earth in the normal mass hierarchy. Panel (b) shows the range of flavor ratios on the Earth in the inverted mass hierarchy.

### 3.3.1.2 Inverted Mass Hierarchy

The transition probability matrix for the heaviest mass and middle eigenstates decay to the lightest and invisible state in the inverted mass hierarchy is written as

$$P_{\alpha\beta}^{dec} = (|U_{\alpha 3}|^2 + |U_{\alpha 2}|^2 Br_{2 \rightarrow 3} + |U_{\alpha 1}|^2 Br_{1 \rightarrow 3}) |U_{\beta 3}|^2, \quad (3.13)$$

where  $0 \leq Br_{2 \rightarrow 3} \leq 1$  and  $0 \leq Br_{1 \rightarrow 3} \leq 1$ . If all unstable states decay to invisible states,  $Br_{2 \rightarrow 3} = 0$  and  $Br_{1 \rightarrow 3} = 0$ , Eq. (3.13) is identical to the case of the middle and lightest mass eigenstates decay all into invisible state in the normal mass hierarchy. Fig. 3.2(b) shows the range of flavor ratios on the Earth with source flavor ratios,  $\phi_0(\nu_e) : \phi_0(\nu_\mu) : \phi_0(\nu_\tau) = \alpha : \beta : 1 - \alpha - \beta$ . Comparing this result with the result of standard neutrino oscillation in Fig. 3.1(b), The range of flavor ratios from the decay of heaviest and middle mass eigenstates in the inverted mass hierarchy can be total separated from the flavor ratios from standard neutrino oscillation in Fig. 3.1(b).

### 3.3.2 The Heaviest Mass Eigenstate Decays to the Middle, Lightest and Invisible States

#### 3.3.2.1 Normal Mass Hierarchy

The transition probability matrix for the heaviest mass eigenstate decays to the middle, lightest and invisible state in the normal mass hierarchy is written as

$$P_{\alpha\beta}^{dec} = |U_{\alpha 2}|^2 |U_{\beta 2}|^2 + |U_{\alpha 1}|^2 |U_{\beta 1}|^2 + |U_{\alpha 3}|^2 |U_{\beta 2}|^2 Br_{3 \rightarrow 2} + |U_{\alpha 3}|^2 |U_{\beta 1}|^2 Br_{3 \rightarrow 1}, \quad (3.14)$$

where  $0 \leq Br_{3 \rightarrow 2} \leq 1$  and  $0 \leq Br_{3 \rightarrow 1} \leq 1$ . In the limit of  $Br_{3 \rightarrow 2} = 0$  and  $Br_{3 \rightarrow 1} = 0$ , Eq. (3.14) is identical to the case of the lightest mass eigenstate decays to invisible states in the inverted mass hierarchy. Fig. 3.3(a) shows the range of flavor ratios on the Earth with source flavor ratios,  $\phi(\nu_e) : \phi_0(\nu_\mu) : \phi_0(\nu_\tau) = \alpha : \beta : 1 - \alpha - \beta$ . Comparing this result with the result of standard neutrino oscillation in Fig. 3.1(b). The range of flavor ratios from the heaviest mass eigenstate decay in the normal mass hierarchy overlap almost fully with the range given by standard neutrino oscillation.

#### 3.3.2.2 Inverted Mass Hierarchy

The transition probability matrix for the heaviest mass eigenstate decays to the middle, lightest and invisible state in the normal mass hierarchy is written as

$$P_{\alpha\beta}^{dec} = |U_{\alpha 1}|^2 |U_{\beta 1}|^2 + |U_{\alpha 3}|^2 |U_{\beta 3}|^2 + |U_{\alpha 2}|^2 |U_{\beta 1}|^2 Br_{2 \rightarrow 1} + |U_{\alpha 2}|^2 |U_{\beta 3}|^2 Br_{2 \rightarrow 3}, \quad (3.15)$$

where  $0 \leq Br_{2 \rightarrow 3} \leq 1$  and  $0 \leq Br_{2 \rightarrow 1} \leq 1$ . In the limit of  $Br_{2 \rightarrow 3} = 0$ , Eq. (3.15) is identical to the case of the middle mass eigenstate decay inverted in the normal mass hierarchy. Fig. 3.4(a) shows the range of flavor ratios on the Earth with source flavor ratios,  $\phi(\nu_e) : \phi_0(\nu_\mu) : \phi_0(\nu_\tau) = \alpha : \beta : 1 - \alpha - \beta$ . Comparing this result with the result of standard neutrino oscillation in Fig. 3.1(b). The range of flavor ratios from the heaviest mass eigenstate decay in the inverted mass

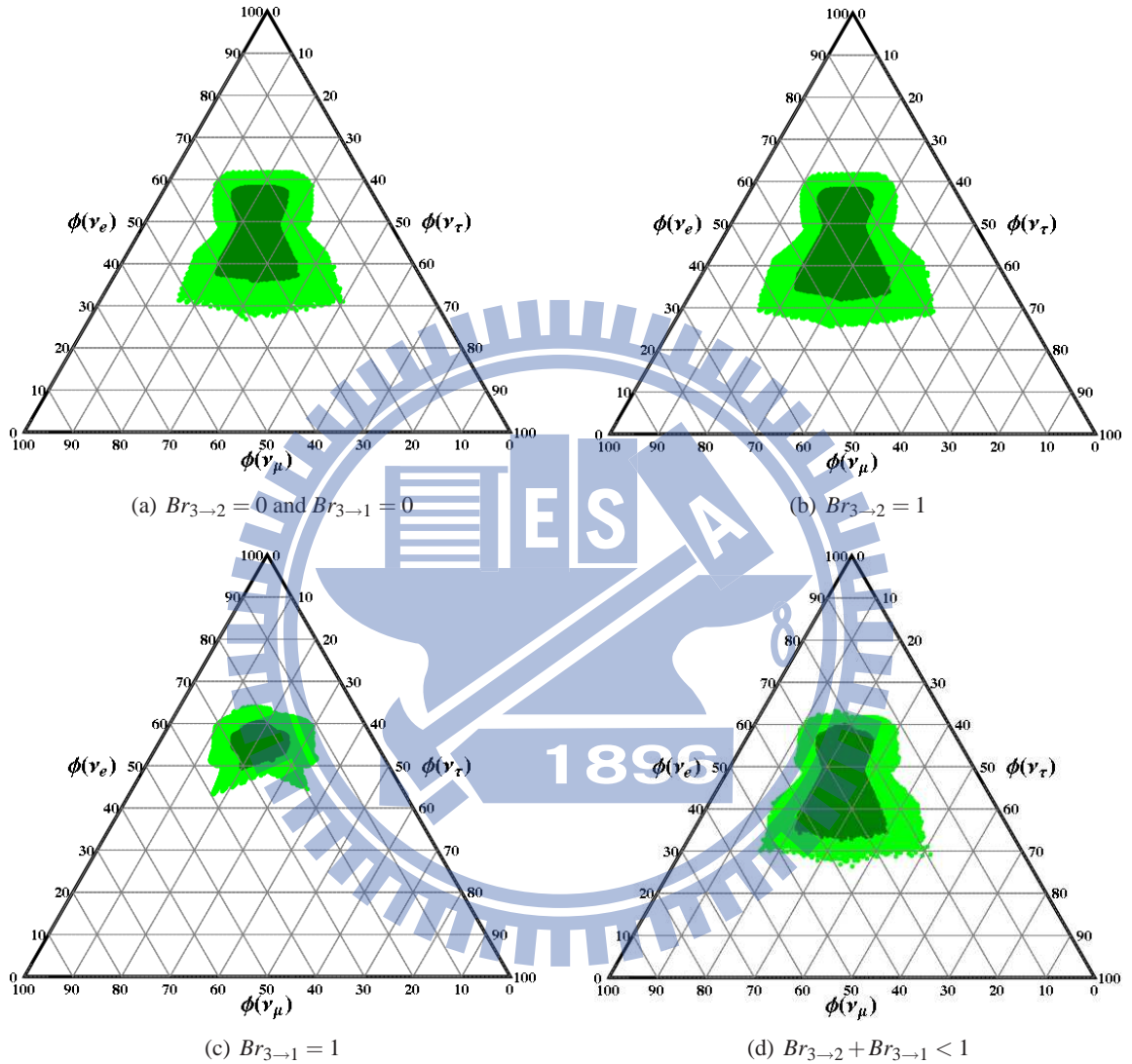


Figure 3.3: The range of flavor ratios on the Earth from the heaviest mass eigenstate decays to the middle, lightest and invisible state in the normal mass hierarchy. Panel (a) shows the range of flavor ratios on the Earth from the heaviest eigenstate decays to invisible eigenstates only. Panel (b) shows the range of flavor ratios on the Earth from the heaviest eigenstate decays to the middle eigenstate only. Panel (c) shows the range of flavor ratios on the Earth from the heaviest eigenstate decays to the lightest eigenstate only. Panel (d) shows the all possible flavor ratios on the Earth which satisfy  $Br_{H \rightarrow M} + Br_{H \rightarrow L} + Br_{H \rightarrow \text{invisible}} = 1$ .



hierarchy overlap almost fully with the range given by standard neutrino oscillation.

### 3.3.3 The Middle Mass Eigenstate Decays to the Lightest and Invisible States

#### 3.3.3.1 Normal Mass Hierarchy

The transition probability matrix for the middle mass eigenstate decays to the lightest and invisible states in the normal mass hierarchy is written as

$$P_{\alpha\beta}^{dec} = |U_{\alpha 3}|^2 |U_{\beta 3}|^2 + |U_{\alpha 1}|^2 |U_{\beta 1}|^2 + |U_{\alpha 2}|^2 |U_{\beta 1}|^2 Br_{2\rightarrow 1}, \quad (3.16)$$

where  $0 \leq Br_{2\rightarrow 1} \leq 1$ . In the limit of  $Br_{2\rightarrow 1} = 0$ , Eq. (3.16) is identical to the case of the middle mass eigenstate fully decays to invisible states in the normal mass hierarchy. Fig. 3.5(a) shows the range of flavor ratios on the Earth with source flavor ratios,  $\phi_0(\nu_e) : \phi_0(\nu_\mu) : \phi_0(\nu_\tau) = \alpha : \beta : 1 - \alpha - \beta$ . Comparing this result with the result of standard neutrino oscillation in Fig. 3.1(b). The range of flavor ratios from the middle mass eigenstate decay in the normal mass hierarchy overlap almost fully with the range given by standard neutrino oscillation.

#### 3.3.3.2 Inverted Mass Hierarchy

The transition probability matrix for the middle mass eigenstate decays to the lightest and invisible states in the normal mass hierarchy is written as

$$P_{\alpha\beta}^{dec} = |U_{\alpha 2}|^2 |U_{\beta 2}|^2 + |U_{\alpha 3}|^2 |U_{\beta 3}|^2 + |U_{\alpha 1}|^2 |U_{\beta 3}|^2 Br_{1\rightarrow 3}, \quad (3.17)$$

where  $0 \leq Br_{1\rightarrow 3} \leq 1$ . In the limit of  $Br_{1\rightarrow 3} = 0$ , Eq. (3.17) is identical to the case of the lightest mass eigenstate fully decays to invisible states in the normal mass hierarchy. Fig. 3.5(b) shows the range of flavor ratios on the Earth with source flavor ratios,  $\phi_0(\nu_e) : \phi_0(\nu_\mu) : \phi_0(\nu_\tau) = \alpha : \beta : 1 - \alpha - \beta$ . Comparing this result with the result of standard neutrino oscillation in Fig. 3.1(b). The range of flavor ratios from the middle mass eigenstate decay in the inverted mass hierarchy overlap the range given by standard neutrino oscillation in  $0.15 < \phi(\nu_e) < 0.4$ .

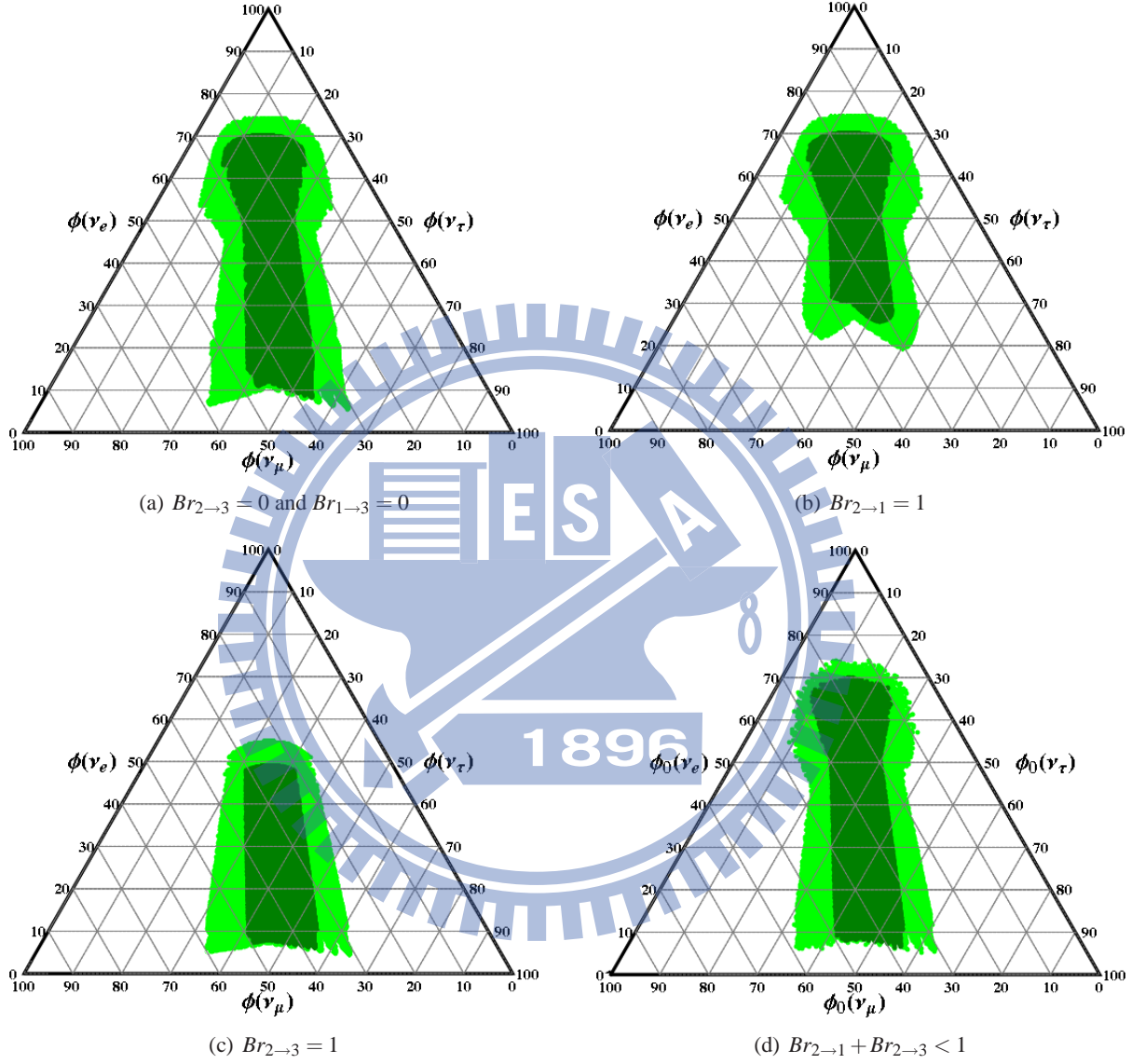


Figure 3.4: The range of flavor ratios on the Earth from the heaviest mass eigenstate decays to the middle, lightest and invisible state in the inverted mass hierarchy. Panel (a) shows the range of flavor ratios on the Earth from the heaviest eigenstate decays to invisible eigenstates only. Panel (b) shows the range of flavor ratios on the Earth from the heaviest eigenstate decays to the middle eigenstate only. Panel (c) shows the range of flavor ratios on the Earth from the heaviest eigenstate decays to the lightest eigenstate only. Panel (d) shows the all possible flavor ratios on the Earth which satisfy  $Br_{H\rightarrow M} + Br_{H\rightarrow L} + Br_{H\rightarrow\text{invisible}} = 1$ .

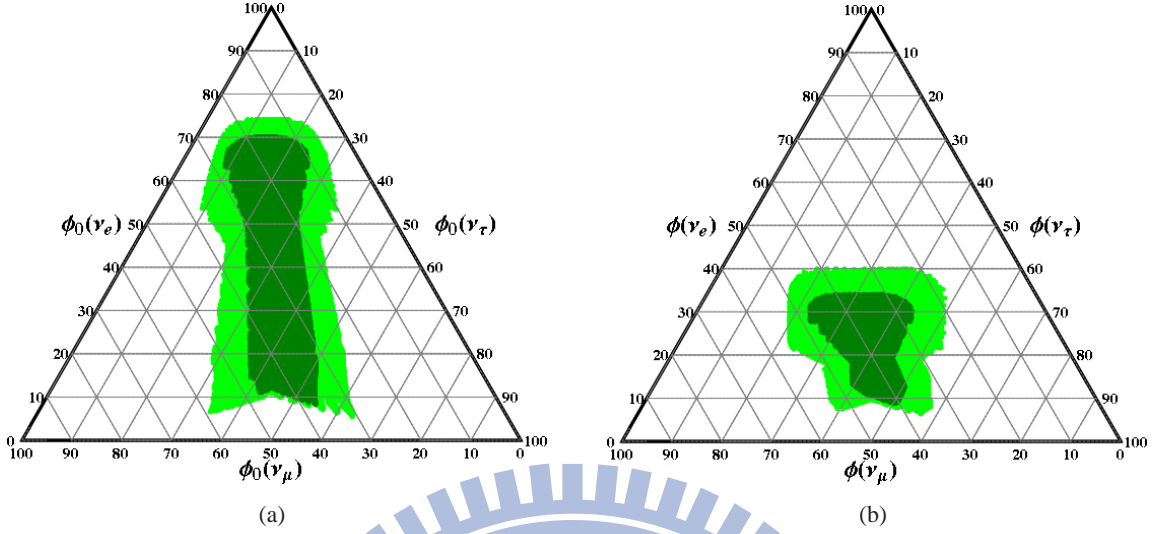


Figure 3.5: The range of flavor ratios on the Earth from the middle mass eigenstate decays to the lightest and invisible states. The branching ratio,  $Br_{M \rightarrow L} + Br_{M \rightarrow \text{invisible}} = 1$ , for both hierarchy. Panel (a) shows the flavor ratios on the Earth from the middle mass eigenstate decays to the lightest and invisible states in the normal mass hierarchy. In this case, the range of flavor ratios on the Earth from the heaviest mass eigenstate decay in the inverted mass hierarchy is same as the middle mass eigenstate decay in the normal mass hierarchy. Panel (b) shows the flavor ratios on the Earth from the middle mass eigenstate decays to the lightest and invisible states in the inverted mass hierarchy.

### 3.3.4 The Lightest Mass Eigenstate decays to Invisible States Only

#### 3.3.4.1 Normal Mass Hierarchy

The transition probability matrix for the lightest mass eigenstate decays to invisible states in the normal mass hierarchy is written as

$$P_{\alpha\beta}^{dec} = |U_{\alpha 3}|^2 |U_{\beta 3}|^2 + |U_{\alpha 2}|^2 |U_{\beta 2}|^2. \quad (3.18)$$

Eq. (3.18) is identical to the case of the middle eigenstate fully decays to invisible state in the inverted mass hierarchy. Fig. 3.6(a) shows the range of flavor ratios on the Earth with source flavor ratios,  $\phi_0(\nu_e) : \phi_0(\nu_\mu) : \phi_0(\nu_\tau) = \alpha : \beta : 1 - \alpha - \beta$ . Comparing this result with the result of standard neutrino oscillation in Fig. 3.1(b). The range of flavor ratios from the lightest mass eigenstate decay in the normal mass hierarchy overlap the range given by standard neutrino oscillation in  $0.15 < \phi(\nu_e) < 0.4$ .

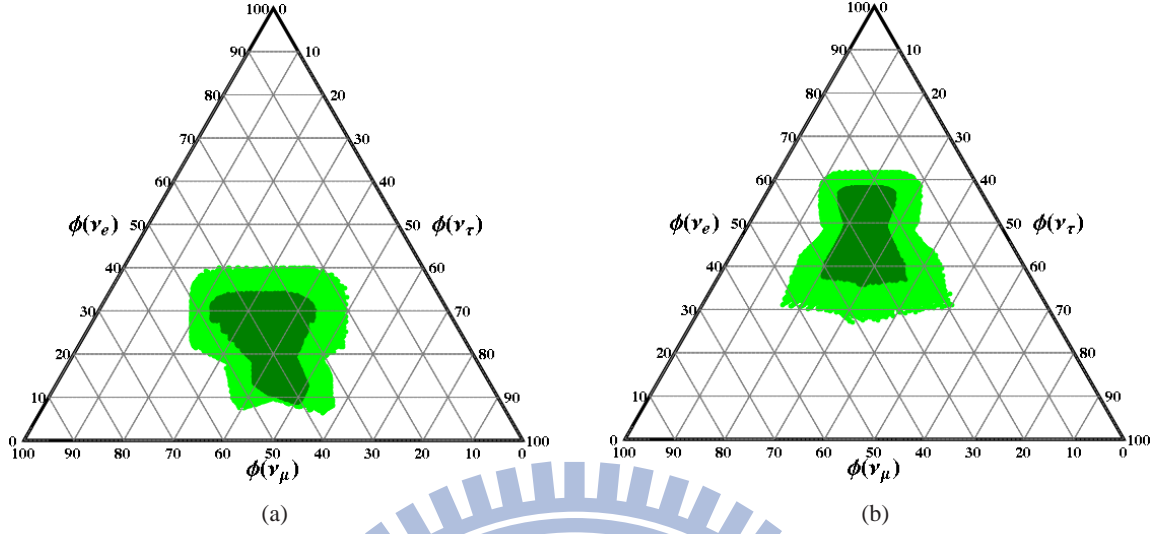


Figure 3.6: The range of flavor ratios on the Earth from the lightest mass eigenstate decays to invisible states only. The lightest neutrino mass eigenstate decays to invisible state only. The branching ratio,  $Br_{L \rightarrow \text{invisible}} = 1$ , for both hierarchy. Panel (a) shows the lightest eigenstate decays to invisible states in the normal mass hierarchy. The possible flavor ratios are same as the case of the middle mass eigenstate decay. Panel (b) shows the lightest eigenstate decays to invisible state only in the inverted mass hierarchy. The possible flavor ratios are same as the case of the heaviest mass eigenstate decay in the normal mass hierarchy.

### 3.3.4.2 Inverted Mass Hierarchy

The transition probability matrix for the lightest mass eigenstate decays to invisible states in the inverted mass hierarchy is written as

$$P_{\alpha\beta}^{dec} = |U_{\alpha 2}|^2 |U_{\beta 2}|^2 + |U_{\alpha 1}|^2 |U_{\beta 1}|^2. \quad (3.19)$$

Eq. (3.19) is identical to the case of the heaviest mass eigenstate fully decays to invisible states in the normal mass hierarchy. Fig. 3.6(b) shows the range of flavor ratios on the Earth with source flavor ratios,  $\phi_0(\nu_e), \phi_0(\nu_\mu), \phi_0(\nu_\tau) = \alpha, \beta, 1 - \alpha - \beta$ . Comparing this result with the result of standard neutrino oscillation in Fig. 3.1(b). The range of flavor ratios from the lightest mass eigenstate decay in the inverted mass hierarchy overlap the range given by standard neutrino oscillation in  $0.3 < \phi(\nu_e) < 0.6$ .

### 3.3.5 The Middle and Lightest Mass Eigenstates decay to Invisible States Only

#### 3.3.5.1 Normal Mass Hierarchy

The transition probability matrix for the middle and lightest mass eigenstates fully decays to invisible states in the inverted mass hierarchy is written as

$$P_{\alpha\beta}^{dec} = |U_{\alpha 3}|^2 |U_{\beta 3}|^2. \quad (3.20)$$

Eq. (3.20) is identical to the case of the heaviest and middle mass eigenstates fully decay to invisible state in the inverted mass hierarchy. Fig. 3.7(a) shows the range of flavor ratios on the Earth with source flavor ratios,  $\phi_0(\nu_e) : \phi_0(\nu_\mu) : \phi_0(\nu_\tau) = \alpha : \beta : 1 - \alpha - \beta$ . Comparing this result with the result of standard neutrino oscillation in Fig. 3.1(b), The range of flavor ratios from the middle and lightest mass eigenstates decay in the normal mass hierarchy can be total separated from the flavor ratios from standard neutrino oscillation in Fig. 3.1(b).

#### 3.3.5.2 Inverted Mass Hierarchy

The transition probability matrix for the middle and lightest mass eigenstates fully decays to invisible states in the inverted mass hierarchy is written as

$$P_{\alpha\beta}^{dec} = |U_{\alpha 2}|^2 |U_{\beta 2}|^2. \quad (3.21)$$

Eq. (3.21) is identical to the case of the heaviest and lightest mass eigenstates fully decay to invisible state in the inverted mass hierarchy. Fig. 3.7(a) shows the range of flavor ratios on the Earth with source flavor ratios,  $\phi_0(\nu_e) : \phi_0(\nu_\mu) : \phi_0(\nu_\tau) = \alpha : \beta : 1 - \alpha - \beta$ . Comparing this result with the result of standard neutrino oscillation in Fig. 3.1(b), The overlapped region of those two cases is between  $\phi(\nu_e) = 0.4$  to  $\phi(\nu_e) = 0.25$ .

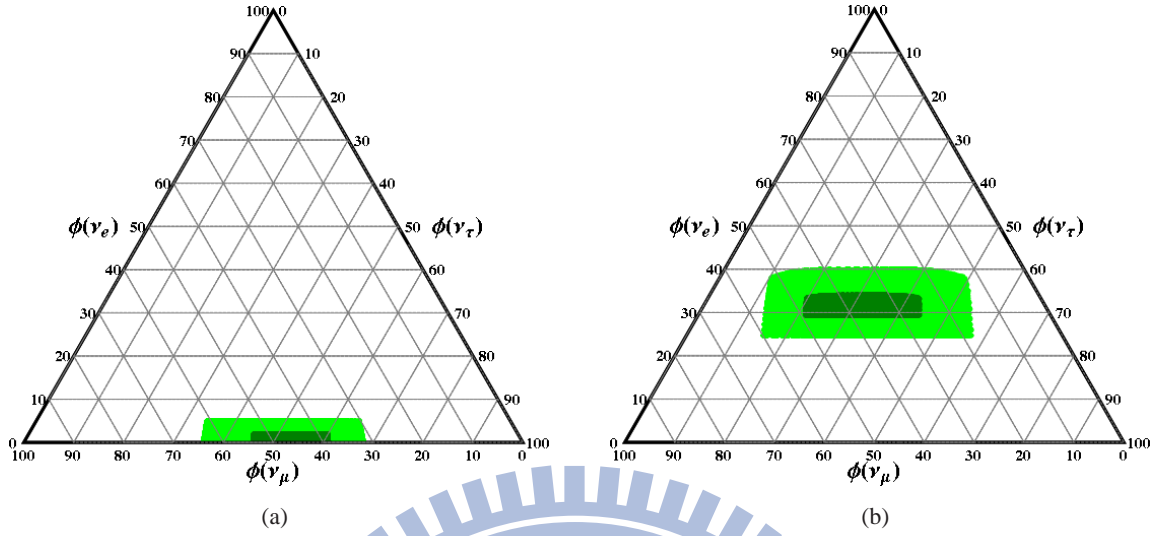


Figure 3.7: The range of flavor ratios on the Earth from the middle and the lightest mass eigenstates decay to invisible states. The middle mass eigenstate can decay to the lightest and invisible eigenstates, but the lightest neutrino mass eigenstate only can decay to invisible state. Hence the final branching ratios of the middle and lightest mass eigenstates are  $Br_{M \rightarrow \text{invisible}} = 1$  and  $Br_{L \rightarrow \text{invisible}} = 1$  for both hierarchy. Panel (a) shows the middle and lightest mass eigenstates decay to invisible states in the normal mass hierarchy. Panel (b) shows the middle and lightest mass eigenstates decay to invisible states only in the inverted mass hierarchy.

### 3.3.6 The heaviest and lightest mass eigenstates decay to the middle mass eigenstate and invisible states only

#### 3.3.6.1 Normal Mass Hierarchy

The transition probability matrix for the lightest mass eigenstate decays to invisible states in the inverted mass hierarchy is written as

$$P_{\alpha\beta}^{dec} = |U_{\alpha 2}|^2 |U_{\beta 2}|^2 + |U_{\alpha 3}|^2 |U_{\beta 2}|^2 Br_{3 \rightarrow 2}. \quad (3.22)$$

It is easy to find the Eq. (3.22) is identical to the case of the middle and lightest mass eigenstates fully decay to invisible state in the inverted mass hierarchy. Fig. 3.8(a) shows the range of flavor ratios on the Earth with source flavor ratios,  $\phi_0(\nu_e) : \phi_0(\nu_\mu) : \phi_0(\nu_\tau) = \alpha : \beta : 1 - \alpha - \beta$ . Comparing this result with the result of standard neutrino oscillation in Fig. 3.1(b), The overlapped region of those two cases is between  $\phi(\nu_e) = 0.4$  to  $\phi(\nu_e) = 0.25$ .

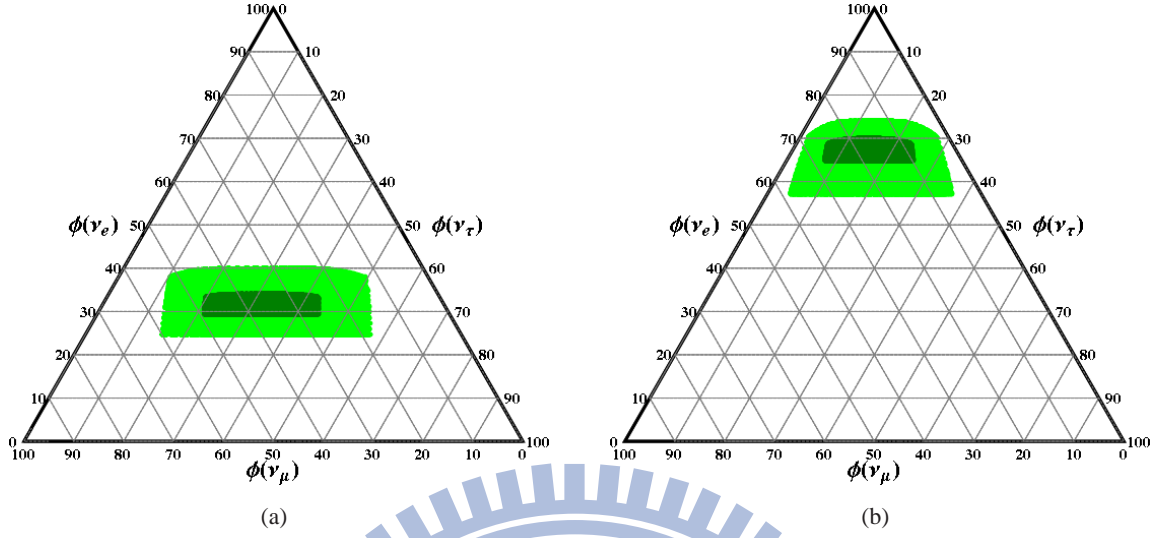


Figure 3.8: The range of flavor ratios on the Earth from the heaviest and lightest mass eigenstates decay to the middle mass eigenstate and invisible states. The heaviest mass eigenstate can decay to the middle mass eigenstate and invisible eigenstates, but the lightest neutrino mass eigenstate only can decay to invisible eigenstates. Hence the final branching ratios of the heaviest and lightest mass eigenstates are  $Br_{H \rightarrow M} + Br_{H \rightarrow invisible} = 1$  and  $Br_{L \rightarrow invisible} = 1$  for both hierarchy. Panel (a) shows the possible flavor ratios on the Earth in the normal mass hierarchy. Panel (b) shows the possible flavor ratios on the Earth in the inverted mass hierarchy.

### 3.3.6.2 Inverted Mass Hierarchy

The transition probability matrix for the lightest mass eigenstate decays to invisible states in the inverted mass hierarchy is written as

$$P_{\alpha\beta}^{dec} = |U_{\alpha 1}|^2 |U_{\beta 1}|^2 + |U_{\alpha 2}|^2 |U_{\beta 2}|^2 Br_{2 \rightarrow 1}. \quad (3.23)$$

Eq. (3.23) is identical to the case of the heaviest and middle mass eigenstates fully decay to invisible state in the normal mass hierarchy. Fig. 3.8(a) shows the range of flavor ratios on the Earth with source flavor ratios,  $\phi_0(\nu_e) : \phi_0(\nu_\mu) : \phi_0(\nu_\tau) = \alpha : \beta : 1 - \alpha - \beta$ . Comparing this result with the result of standard neutrino oscillation in Fig. 3.1(b), The overlapped region between those two cases is around  $\phi(\nu_e) \sim 0.6$ .

### 3.4 The Most Probable Neutrino Flavor Ratios on the Earth Induced by Standard Neutrino Oscillation and Neutrino Decays

Summarizing the above results, it is easy to realize the relationship between measured ratios and neutrino flavor transition mechanisms. Fig. 3.9 shows the most probable flavor ratios on the Earth induced by standard neutrino oscillation and neutrino decays. The red line indicates the range of flavor ratios from standard neutrino oscillation and the other lines indicate those from the different neutrino decay mechanisms. The saturation of color is proportional to the observed number of neutrino flavor transition mechanisms. The most probable flavor ratios on the Earth are around the flavor ratio,  $\phi_0(\nu_e) : \phi_0(\nu_\mu) : \phi_0(\nu_\tau) = 1/3 : 1/3 : 1/3$  and denoted by label “#” in Fig. 3.9. This flavor ratios is situated at the union of the neutrino oscillation and the most of decay mechanisms. This flavor ratio can rule out type-II, type-III and type-IV decay models in  $1\sigma$  level and can rule out type-II and type-III decay models in  $3\sigma$  level. The types of neutrino decay models are listed in Table 3.1. The flavor ratio,  $\phi_0(\nu_e) : \phi_0(\nu_\mu) : \phi_0(\nu_\tau) = 0.03 : 0.52 : 0 : 46$ , lays on the “\*” point in Fig. 3.9(b) is the forbidden region for neutrino oscillation mechanisms and the type-III decay model is the only possible mechanism to produce such a flavor ratio. The colorless area is the forbidden region for all decay and oscillation mechanisms. For example, if some experiment observed a flavor ratio,  $\phi_0(\nu_e) : \phi_0(\nu_\mu) : \phi_0(\nu_\tau) = 0.87 : 0.07 : 0.06$ , lays on the “%” point in Fig. 3.9(b). This flavor ratio can be ruled out by all decay and oscillation mechanisms at  $3\sigma$  level.



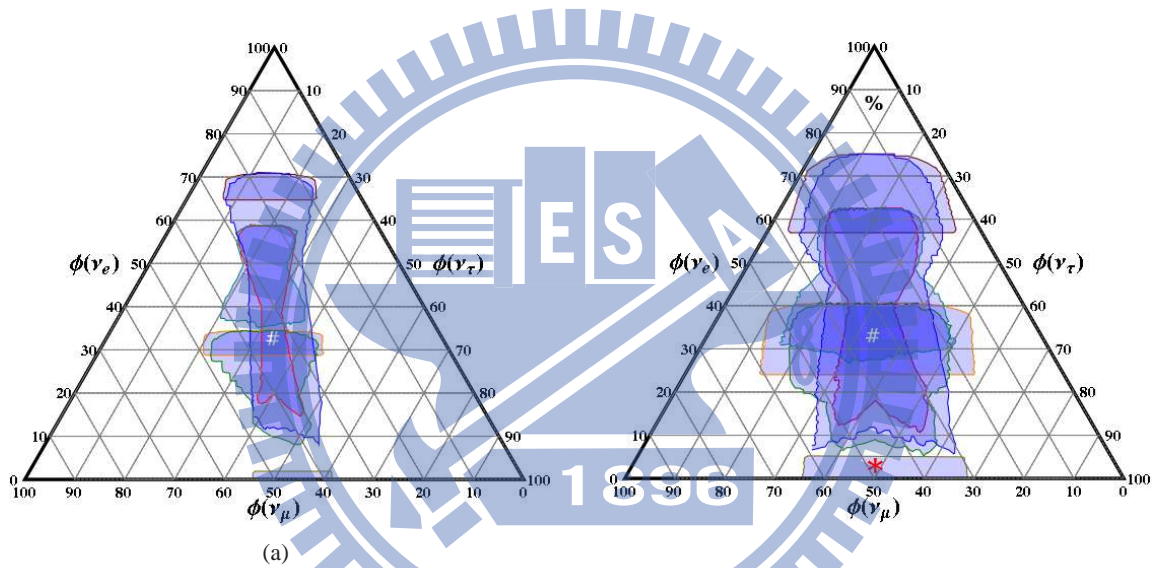
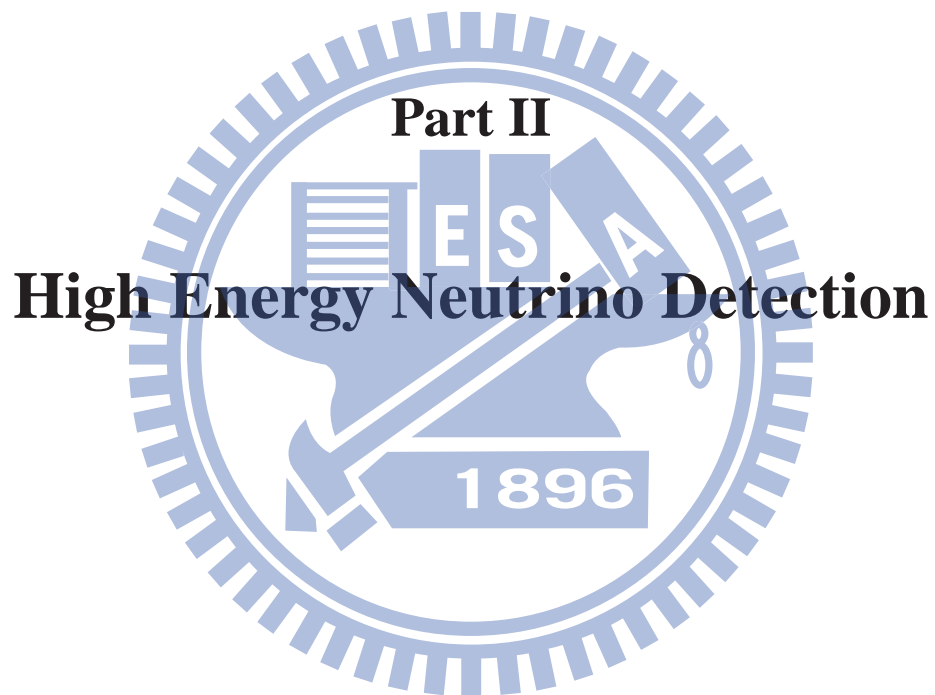


Figure 3.9: The neutrino flavor ratios on the Earth induced by different flavor transition mechanisms. The left panel shows the range of flavor ratios on the Earth from decay and oscillation in  $1\sigma$  level. The right panel shows the ranges at  $3\sigma$  level. Both panels show the most probable flavor ratios on the Earth is around  $\phi_0(\nu_e) : \phi_0(\nu_\mu) : \phi_0(\nu_\tau) = 1/3 : 1/3 : 1/3$



## Chapter 4

# Simulation of High Energy Neutrino

## Interacting with the Earth

This chapter describes the Monte-Carlo simulation code for the interactions and propagation of neutrinos and leptons inside the Earth at energy greater than  $10^{14}$  eV. The neutrino may change to the other kind of particles and lose energy during its propagation. This code can choose both AGN [1] and GZK [6] neutrino flux as initial flux and the distributions of fluxes shown in Fig. 2.1.2. The code simulates the neutrino-nucleon interaction and energy loss process in the Earth. The simulation result can be applied to the underground or above-ground neutrino telescopes. The previous results show that the shower energy are mostly in between  $3 \times 10^{14}$  eV to  $3 \times 10^{16}$  eV for AGN neutrinos and in between  $10^{16}$  eV to  $10^{18}$  eV for GZK neutrinos.

### 4.1 Introduction

In chapter 2, we introduced the neutrino telescope experiment, IceCube [9] or KM3NeT [11], with target volume in the order of  $\text{km}^3$  water-equivalent. In terms of detector acceptance, their typical values are approximately in the order of  $2\pi \text{ km}^2 \text{ sr}$ , since it is sensitive to up-going events and its efficiency depends on the zenith or nadir angle. Tseng *et al.* [29] estimated that  $1 \text{ km}^2 \text{ sr}$  is required to detect PeV level neutrinos from AGN [30] and  $100 \text{ km}^2 \text{ sr}$  is required to detect GZK neutrinos [31]. Such  $\text{km}^3$  size detectors are predicted to observe AGN neutrinos in several years of full-detector operation. The fluorescence detector (FD) such as Fly's Eye/HiRes has larger

observation range. This compact size detector can reach acceptance in the order of  $300 \text{ km}^2 \text{ sr}$  (assumed 10% duty cycle) [32]. However, the current threshold of FD is approximately  $3 \times 10^{17}$  eV and requires some modifications to extend to lower energy. In order to increase photon counts, Cherenkov lights must be included. NuTel [33, 34] and CRTNT [35] experiments try to develop a wide FOV Cherenkov telescopes to aim for detection of high energy neutrinos.

Based on analytical calculation, Tseng *et al.* [29] had provided many useful insights for the design of neutrino telescope using Earth skimming neutrinos. However, detailed simulation of neutrino interactions with the Earth is still required to produce events for further detector simulation. We had developed a Monte-Carlo simulation code for ground based neutrino detector and underground detectors such as IceCube, KM3NeT *etc.*. This code called SHINIE, Simulation of High-energy Neutrino Interacting with the Earth. Several preliminary versions of SHINIE were used in various stages of NuTel [33, 34, 36, 37] and a semi-Monte-Carlo version [36] was used in NuTel [38] and CRTNT [35]. This semi-Monte-Carlo code use deterministic energy loss for tau leptons, which is similar to the formula used in Tseng *et al.* [29].

## 4.2 Interactions

SHINIE considers neutrino nucleon interaction, energy loss and decays of particles in the Earth. We calculate the differential cross section of those interactions and selection one interaction by Monte-Carlo method in one step of interaction.

### 4.2.1 Energy Loss of Leptons

Leptons lose energy by ionization, photonuclear interaction, bremsstrahlung, and pair production. The general form of energy loss for leptons written as

$$\frac{dE}{dX} = -\alpha_{ion} - \sum_i \beta_i E = -\alpha_{ion} - (\beta_{brem} + \beta_{pair} + \beta_{nuc})E, \quad (4.1)$$

where  $X$  is the slant depth,  $\alpha_{ion}$  is ionization contribution,  $\beta_{brem}$ ,  $\beta_{pair}$  and  $\beta_{nuc}$  correspond the contributions from bremsstrahlung, photonuclear interaction and pair production respectively. those three processes are simulated in stochastic procedure. Each process has its own differential

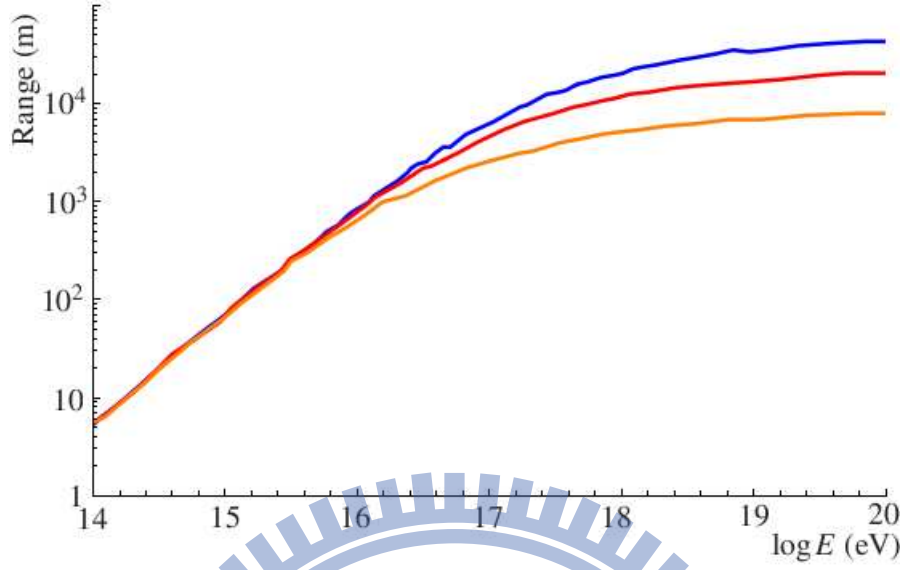


Figure 4.1: The range of tau leptons in materials. Blue, red and orange lines correspond to the range of tau leptons in water, standard rock, and iron respectively. The range of tau in iron is much lower than standard rock and water at  $10^{20}$  eV.

cross-section,  $\sigma^{brem}$ ,  $\sigma^{pair}$  and  $\sigma^{nuc}$ .  $\beta_i$  are define as

$$\beta_i(E) = \frac{N}{A} \int_{ymin}^{ymax} y \frac{d\sigma^i(y, E)}{dy} dy, \quad (4.2)$$

where  $N$  is Avogadro's number,  $A$  is atomic mass number and  $\sigma^i$  is cross section for individual interaction. The  $y$  is the fraction of lepton energy loss in interaction and written as

$$y = \frac{E - E'}{E}, \quad (4.3)$$

where  $E$  is the energy of incident lepton,  $E'$  is the energy of same particle after interaction. The way to perform the energy loss of leptons in Monte-Carlo method is shown in App. B. The range of tau in SHINIE have simulated by Iong and Hung and shown in Fig. 4.1 [71, 72].

#### 4.2.1.1 Ionization

The ionization, soft energy loss, losses only a small amount of energy with high probability. To save simulation time, it is simulated with analytical method by  $E' = E - \alpha_{ion}dX$  for a step size in depth of  $dX$ . The threshold of this soft energy cut is set at  $10^{-3}$ .

material	ionization potential (eV)	Z/A	density (g/cm <sup>3</sup> )	$\xi_0$	$\xi_1$	a	C	m
Iron	286	0.46562	7.87	-0.0012	3.153	0.147	4.291	2.963
Water	75	0.55509	1	0.240	2.800	0.091	3.502	3.477
Rook	136.4	0.50000	2.65	0.049	3.055	0.083	3.774	3.412

Table 4.1: The parameters in Bethe-Bloch formula

The energy loss by ionization for incident leptons with energy  $E$  and momentum  $p$  is given by the Bethe-Bloch formula [65]

$$\frac{dE}{dX} = 2\pi\alpha^2 N_A \lambda_e^2 \frac{Zm_e}{A\beta^2} \left( \ln \frac{2m_e \beta^2 \gamma^2 E'_m}{I^2(Z)} \right) - 2\beta^2 + \frac{E'_m{}^2}{4E^2} - \delta(\xi), \quad (4.4)$$

with fine structure constant  $\alpha = 1/137$ , Avogadro's number  $N_A = 6.023 \times 10^{23}$ , atomic mass number  $Z$ , atomic weight of medium  $A$ .  $E_{max}$  is the maximum transferred energy from lepton to electron. The relationship between  $\beta$ ,  $\gamma$ ,  $E$  and  $p$  is

$$\gamma = E/m_l, \quad \beta = p/E.$$

The mean ionization potential,  $I(Z)$ , for rock, iron and water are listed in Table 4.1. The density correction is parameterized by  $\delta(\xi)$  for  $\xi = \log_{10} \beta\gamma$  [66] as

$$\delta(\xi) = 4.6052\xi + C + a(\xi_1 - \xi)^m \quad \xi_0 < \xi < \xi_1$$

$$\delta(\xi) = 4.6052\xi + C \quad \xi_1 < \xi \quad (4.5)$$

#### 4.2.1.2 Bremsstrahlung

The contribution by bremsstrahlung in energy loss is proportional to the energy of incident particle. The differential cross section of bremsstrahlung written as

$$\frac{d\sigma}{dy} = \alpha^3 (2Z_e \frac{m_e}{m_l})^2 \frac{1}{y} \left( \frac{4}{3} - \frac{4}{3}y + y^2 \right) \phi(\delta), \quad (4.6)$$

where  $\delta = \frac{m_l^2 y}{2E(1-y)}$  and  $\phi(\delta)$  written as

$$\phi(\delta) = \ln\left[\frac{\zeta 189 m_l Z^{-1/3}}{m_e + 189 e^{1/2} \delta Z^{-1/3}}\right], \quad (4.7)$$

where  $\zeta = 1$  for  $Z \leq 10$  and  $\zeta = \frac{2}{3} Z^{-1/3}$  for  $Z > 10$ .

#### 4.2.1.3 Pair production

The differential cross section of pair production is parameterized by the energy of positron,  $E^+$ , and the energy of electron,  $E^-$ . We define the asymmetry parameter as  $\rho = \frac{(E^+ - E^-)}{(E^+ + E^-)}$ . The differential cross section written as [68]

$$\frac{d^2\sigma}{dyd\rho} = \alpha^4 \frac{2}{3\pi} (Z\lambda_e)^2 \frac{1-y}{y} \left[\phi_e + \frac{m_e^2}{m_l^2} \phi_l\right]. \quad (4.8)$$

The form of  $\phi_e$  and  $\phi_l$  are listed in App. A.1.

#### 4.2.1.4 Photonuclear

The differential cross section of photonuclear is written[69] as

$$\begin{aligned} \frac{d\sigma}{dy} = & \frac{\alpha}{2\pi} A \sigma_{\gamma N, y} \left[ \frac{3}{4} G(x) \left( \kappa \ln\left(1 + \frac{m_1^2}{t}\right) - \frac{\kappa m_1^2}{m_1^2 + t} - \frac{2m_1^2}{t} \right) + \right. \\ & \left. \frac{1}{4} \left( \kappa \ln\left(1 + \frac{m_2^2}{t}\right) - \frac{2m_2^2}{t} \right) + \frac{m_l^2}{2t} \left( \frac{3}{4} G(x) \frac{m_1^2}{m_1^2 + t} + \frac{m_2^2}{4t} \ln\left(1 + \frac{t}{m_2^2}\right) \right) \right]. \quad (4.9) \end{aligned}$$

The value of variables are listed in App. A.2.

#### 4.2.2 Lepton decay

The decay length of tau is  $R_\tau = 49.02(E_\tau/\text{PeV})$  m. The tau lepton decays are simulated with TAUOLA code with the full polarization. Table 5.2 lists the six most possible decay channels. The daughter particles (leptons/neutrinos) are fed back to the simulation. The decay length of muon,  $R_\mu = 6.23381 \times 10^6 (E_\mu/\text{GeV})\text{m}$ , is much longer than the decay length of tau. Therefore, the major process of muon are loss energy while traveling through the Earth.

### 4.2.3 Neutrino Charged Current and Neutral Current Interaction

Neutrino interacts with the matter via those two process, charged current and neutral current interaction. The charged current reactions are those involving emission, absorption or exchange of  $W^\pm$  boson. Neutral Current reactions are those exchanging  $Z^0$ . The differential cross-section  $d\sigma/dy$  were calculated in a separate program using the latest parton distribution function CTEQ6 [39, 40], and then imported to SHINIE by a text file.

Charged current (CC) interaction describes a high energy neutrino hits the nucleon producing a lepton and hadronic state

$$\nu_l + N \longrightarrow l^- + \text{anything}. \quad (4.10)$$

The differential cross section of CC interaction is written as

$$\frac{d^2\sigma_{CC}}{dx dy} = \frac{2G_F^2 M E_\nu}{\pi} \left(\frac{M_W^2}{Q^2 + M_W^2}\right)^2 [xq(x, Q^2) + x\bar{q}(x, Q^2)(1-y)^2], \quad (4.11)$$

with Fermi coupling constant  $G_F = 1.16 \times 10^{-5} \text{ GeV}^{-2}$ , the mass of  $W^\pm = 80.4 \text{ GeV}$  and Bjorken scaling variables,  $x = Q^2/2M\nu$  and  $y = \nu/E_\nu$ . The variable  $\nu = E_\nu - E_l$  in Bjorken scaling variables is the energy loss in the laboratory frame. The quark and antiquark distribution in Eq. (4.11) written as

$$q(x, Q^2) = \frac{u_v(x, Q^2) + d_v(x, Q^2)}{2} + \frac{u_s(x, Q^2) + d_s(x, Q^2)}{2} + s_s(x, Q^2) + b_s(x, Q^2)$$

$$\bar{q}(x, Q^2) = \frac{u_s(x, Q^2) + d_s(x, Q^2)}{2} + c_s(x, Q^2) + t_s(x, Q^2)$$

where the labels, “ $u$ ”, “ $d$ ”, “ $c$ ”, “ $s$ ”, “ $t$ ” and “ $b$ ”, denote the distributions for different quark flavor and subscripts “ $v$ ” and “ $s$ ” label the valence and sea contributions.

Neutral current (NC) interaction describes a high energy neutrino hits the nucleon producing a neutrino with lower energy and invisible hadronic state

$$\nu_l + N \longrightarrow \nu_l + \text{anything}. \quad (4.12)$$



The differential cross section of NC interaction is written as

$$\frac{d^2\sigma_{NC}}{dx dy} = \frac{2G_F^2 M E_\nu}{\pi} \left(\frac{M_Z^2}{Q^2 + M_Z^2}\right)^2 [xq^0(x, Q^2) + x\bar{q}^0(x, Q^2)(1-y)^2], \quad (4.13)$$

with the mass of  $Z^0 = 91.2$  GeV. The quark distribution  $q^0$  and antiquark distribution  $\bar{q}^0$  in Eq. (4.13) written as

$$q^0(x, Q^2) = \left[ \frac{u_v(x, Q^2) + d_v(x, Q^2)}{2} + \frac{u_s(x, Q^2) + d_s(x, Q^2)}{2} \right] \left[ \left(1 - \frac{4}{3}x_W\right)^2 + \left(-1 + \frac{2}{3}x_W\right)^2 \right] +$$

$$\left[ \frac{u_s(x, Q^2) + d_s(x, Q^2)}{2} \right] \left[ \left(\frac{4}{3}x_W\right)^2 + \left(\frac{2}{3}x_W\right)^2 \right] + [s_s(x, Q^2) + b_s(x, Q^2)] \left[ \left(-1 + \frac{2}{3}x_W\right)^2 + \left(\frac{2}{3}x_W\right)^2 \right]$$

$$\bar{q}^0(x, Q^2) = \left[ \frac{u_v(x, Q^2) + d_v(x, Q^2)}{2} + \frac{u_s(x, Q^2) + d_s(x, Q^2)}{2} \right] \left[ \left(\frac{4}{3}x_W\right)^2 + \left(\frac{2}{3}x_W\right)^2 \right] +$$

$$\left[ \frac{u_s(x, Q^2) + d_s(x, Q^2)}{2} \right] \left[ \left(1 - \frac{4}{3}x_W\right)^2 + \left(-1 + \frac{2}{3}x_W\right)^2 \right] + [c_s(x, Q^2) + t_s(x, Q^2)] \left[ \left(1 - \frac{4}{3}x_W\right)^2 + \frac{4}{3}x_W\right]^2$$

, where  $x_W = \sin^2 \theta_W$  is the weak mixing parameter. The cross sections of charged current interaction and neutral current interaction in SHINIE shown in Fig. 4.2.

### 4.3 Environments

Most of previous studies treat the Earth as same material of standard rock. SHINIE use a complete set of materials to describe the Earth, which has iron in the core and rock in the mantle. Since the real surface layer of Earth could be mountain, sea or icy plateau. The materials of surface in SHINIE can be defined by requestion of user. SHINIE support five materials, rock, water, ice, salt, and iron as surface layer.

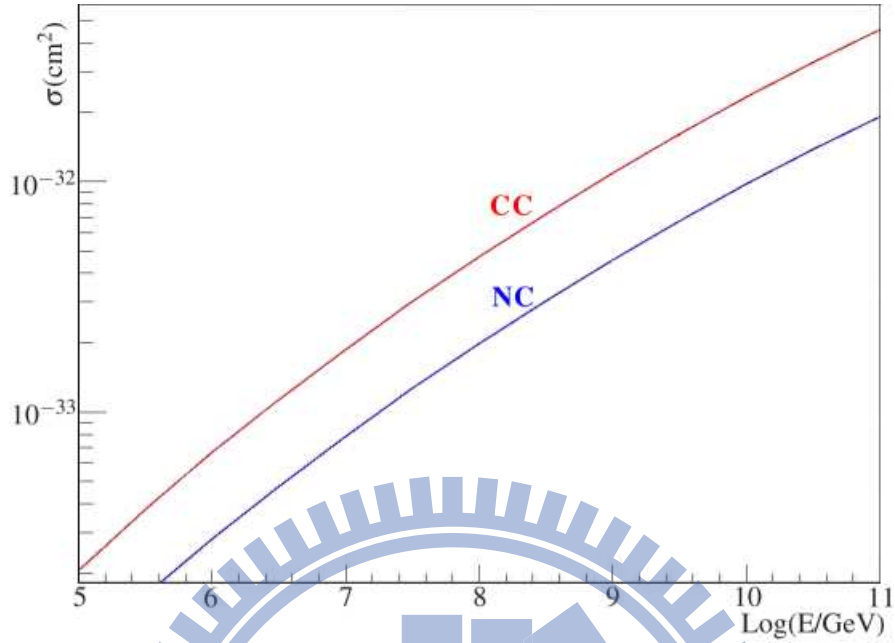


Figure 4.2: Charged current (CC) and neutral current (NC) interaction cross section in SHINIE, according to the CTEQ6-DIS parton distributions. The red and blue curves are CC and NC interaction cross section, respectively, for  $10^5 \leq E_\nu \leq 10^{11}$  GeV.

#### 4.3.1 Earth's Density Model in SHINIE

The earth model in SHINIE is simplified to the perfect sphere with geocentric radius  $R_E = 6371.2$  km, the distance between the mean sea level (MSL) to the center of Earth. Fig. 4.3 and table 4.2 show the density varies with geocentric radius [53]. The material of earth is defined as a three-layer sphere consisting of iron in the core from geocentric radius 0 to 3480 km, rock in the mantle from 3480 to 6367.2 km, which is 4 km below mean sea level. The material of top 4 km layer can be selected by user to suit their needs. Several types of materials such as standard rock, water, ice, salt rock, and iron can be used. For instance, a detector on an island would need the water as top layer of Earth. A detector inside ice could select ice as top layer. The default value of top layer is water, since 70% of Earth is covered by oceans.

For a detector on the ground, user may supply a local map for detailed local materials and elevation. Detector can be placed in above or below Mean Sea Level (MSL). The geometry data, in grid of the longitude, latitude and altitudes can imported to SHINIE as the surface layer. The range of altitudes allowed is between -4 km to 10 km. For interactions inside the range of local map, the local terrain replaces the standard Earth model described in previous paragraph. In a

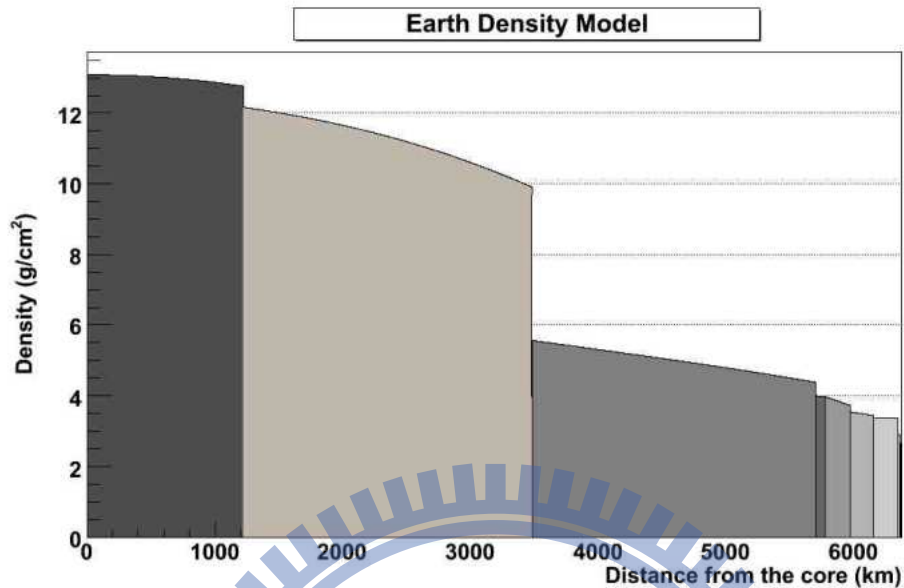


Figure 4.3: density model of earth

simulation with realistic geometry method, SHINIE predefine a layer of air with constant density covering over the top of terrain. Fig. 4.4 shows the allowed import data and the mountain data was used in CRTNT experiment [70].

#### 4.3.2 Detector Sensitive Region (DSR)

User must define the material and dimension of a region, called detector sensitive region (DSR), where all the information of particles within this area will be written to an output files. The information include the particle types, energy, direction and interaction status *etc.*. The interaction status are listed in Table 4.3. This region must be larger than the physical size of real detector. Material can be selected from one of five default materials, standard rock, water, ice, salt rock, and iron. User could also provide their own material with specification of density, mean atomic number, and filename, where coefficients of energy loss are tabulated. DSR material can be different from target materials surrounding DSR.

radius $R$	Density( $\text{g}/\text{cm}^3$ )
$R \leq 1221.5 \text{ km}$	$13.089 - 8.838 \times R_f^2$
$R \leq 3480.0 \text{ km}$	$12.582 - 1.2638 \times R_f - 3.643 \times R_f^2 - 5.528 \times R_f^2$
$R \leq 5701.0 \text{ km}$	$7.957 - 6.476 \times R_f + 5.528 \times R_f^2 - 3.081 \times R_f^3$
$R \leq 5771.0 \text{ km}$	$5.320 - 1.4836 \times R_f;$
$R \leq 5971.0 \text{ km}$	$11.249 - 8.0298 \times R_f;$
$R \leq 6151.0 \text{ km}$	$7.109 - 3.8045 \times R_f;$
$R \leq 6346.6 \text{ km}$	$2.691 + 0.6924 \times R_f;$
$R \leq 6356.0 \text{ km}$	2.9
$R \leq 6367.2 \text{ km}$	2.65 (standard rock)
$R \geq 6372.2 \text{ km}$	0.001 (atmosphere) 0.9 (ice) 1.02 (seawater) 2.65 (rock)

Table 4.2: The Density of Earth,  $R_f$  is fraction of earth radius. The density of the Earth. The symbol “ $R$ ” is the distance from the center of the Earth to an observable location.

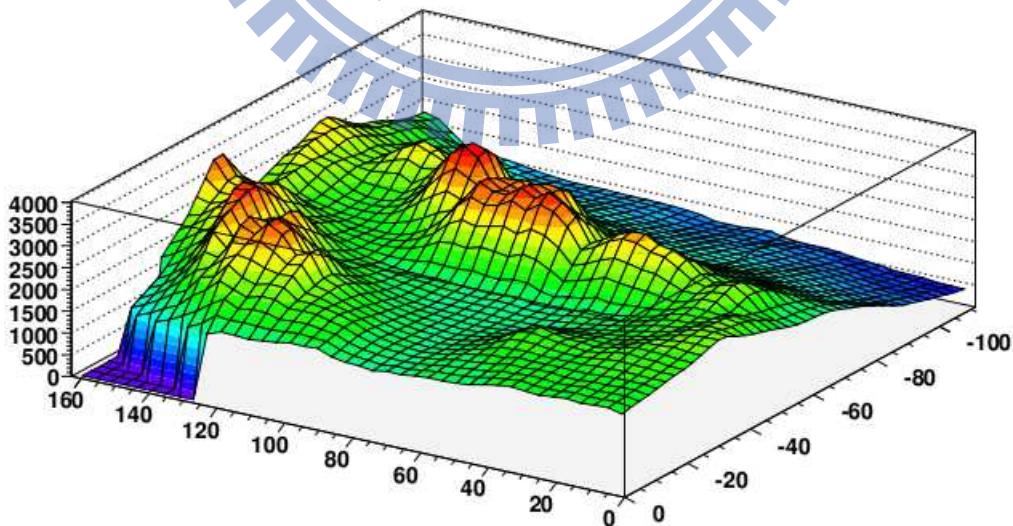


Figure 4.4: The grid map data with altitudes.

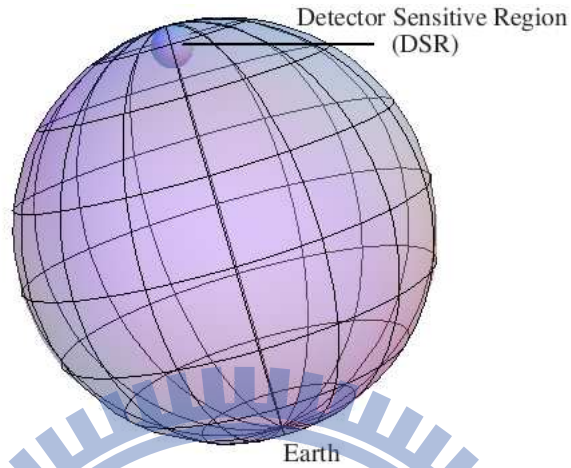


Figure 4.5: Detector sensitive region (DSR). The size, material and position of DSR can be defined by user. SHINIE record all information of particles within this area.

Status identifications	
Status	identifications
Particle initialization	0
Black hole creates lepton	1
Neutrino before NC interaction	2
Neutrino generated by NC interaction	3
Neutrino before CC interaction	4
Lepton generated by CC interaction	5
Lepton energy loss	6
Lepton Before inverse CC interaction to neutrino	8
Neutrino generated by inverse CC interaction	9
Lepton in detector	13
Lepton before decay to neutrino	21
Neutrino created by lepton decay	22
Stopping simulation	100
Stopping simulation by low energy limit	101
Stopping simulation by geometry limit	102

Table 4.3: Status identifications as used in SHINIE.

Particle identifications	
Particle	Identification
$\nu_\tau$	1001
$\tau^-$	1002
$\nu_\mu$	1003
$\mu^-$	1004
$\nu_\tau$	1005
$\tau^-$	1006

Table 4.4: Particle identifications as used in SHINIE.

#### 4.4 Controls of Simulation

All particles are identify by an identification number (ID) and listed in Table. 4.4. Particle energy can be selected from three methods: fixed value, sampling from a power law spectrum, or from a tabulated spectrum, which is supplied by user. Flux between two adjacent energy bins are interpreted as power law spectrum fitted from two adjacent data points. The input to SHINIE is controlled by an input card, similar to the input card of CORSIKA. Fig 4.6 shown the graphic interface system. User can use graphic interface system to setup the parameters for simulation. The input card will be generated automatically and named “UserInput.txt”. Two output format are provided, the default option is printout interaction inside DSR only, the other option is printout all interactions for systematic check.

#### 4.5 Running Options

The basic command to run SHINIE is

```
./main3d UserInput.txt 2>/dev/null> Output.txt &
```

The meaning of each words are listed in Table. 4.5.

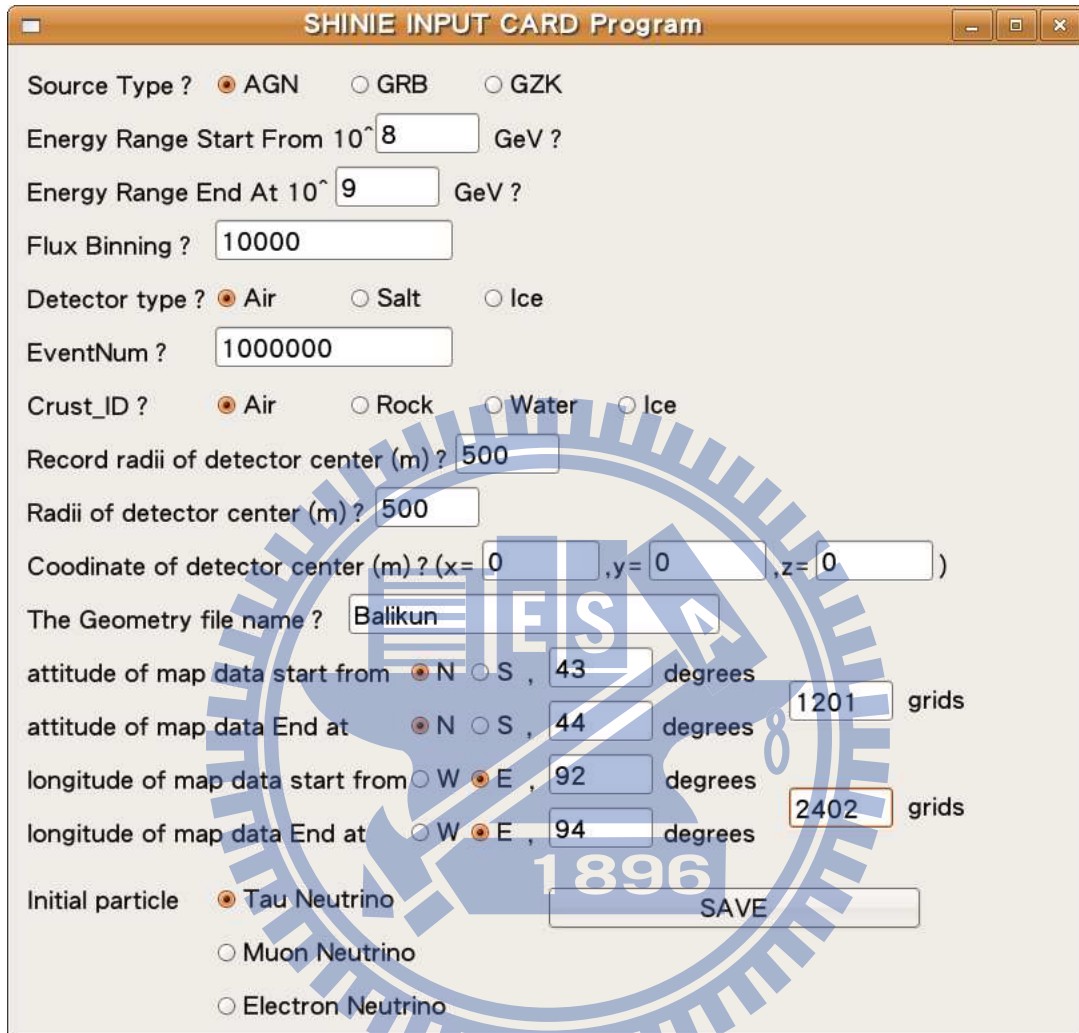


Figure 4.6: Graphic interface system

command	
UserInput.txt	filename of inputcard
2> /dev/null	output err message to null space
Output.txt	filename of output file
&	background

Table 4.5: Running command

## Chapter 5

# Geosynchrotron Raiation Detector

Due to the low interaction cross section of high energy neutrinos, the neutrinos are difficult to interact with intergalactic or interstellar media. Also, neutrinos are neutral particle, they cannot be deflected by the magnetic fields. Unlike charged cosmic rays, neutrinos can be tracked back to their sources and study high energy processes occurring at their sources. Various detectors have been proposed for detecting high energy neutrinos. Some of them rely on measuring the air shower by the so-called earth-skimming  $\nu_\tau$ , for which horizontal showers are generated by the ensuing  $\tau$  decay [41, 42]. However, those events are very rare and required a detector of huge acceptance. Radio detection is a promising techniques, which have advantage of large Cherenkov angle and duty cycle of almost 100%, compared to 10% of opticalshower detector. One type of radio signal is geosynchrotron radiation, which results from charged particles moving in geomagnetic field. This chapter describes a simulation procedures of geosynchrotron radiation. We investigate the shower properties by simulations. Equipped with the knowledge of the  $\nu_\tau$  induced air shower, we are able to calculate the induced geosynchrotron radiation. The CORSIKA [43] simulated shower profile to be employed in the calculation of geosynchrotron radiation in Sec. 5.2. Our calculation is based on the coherent geosynchrotron emission scenario initiated in 1970's [44] and further developed by Huege and Falcke [45]. Finally the reconstructed pulses form emitted radiation are shown in Sec. 5.3.3.



## 5.1 Extensive Air Shower (EAS)

### 5.1.1 Longitudinal Profile

Extensive air shower are generate by high energy particles interacting with the atmosphere. The number of particles reaches the maximum,  $N_{max}$ , when the average energy of secondary particle equal to critical energy,  $E_c$ . The critical energy is defined by the energy loss of ionization equals the energy loss of bremsstrahlung. The  $N_{max}$  can be approximated by

$$N_{max} = N(X_{max}) = E/E_c, \quad (5.1)$$

where  $X_{max}$  is the slant depth at shower maximum,  $E$  is the energy of primary particle,  $E_c = 86$  MeV corresponds to the critical energy of electron in the air. The depth of shower maximum,  $X_{max}$ , is written as

$$X_{max} \sim X_o \ln(E/E_c), \quad (5.2)$$

where  $X_o$  denotes the radiation length of air. The longitudinal profile is parametrised by shower age  $S$ :

$$S(X) = \frac{3X/X_o}{X/X_o + 2 \ln(E/E_c)}$$

$$S(0) = 0, S(X_{max}) = \frac{3X_{max}}{X_{max} + 2X_{max}} = 1. \quad (5.3)$$

The shower starts to develop at  $S = 0$  and reaches it maximum at  $S = 1$ . Figs. 5.2, 5.5 and 5.8 show the longitudinal profiles for electron,  $\pi^-$  and  $K^-$  with energy between  $10^{16.5}$  to  $10^{18.5}$  eV. The relationships between the slant depth and propagation distance in the air with constant density are shown in Fig. 5.1.

### 5.1.2 Lateral Distribution Function

The spread of lateral distribution is proportional to the incident depth,  $X$ , in the air. The previous study of Kamata and Nishimura gave the lateral spread of the purely electromagnetic shower [46].

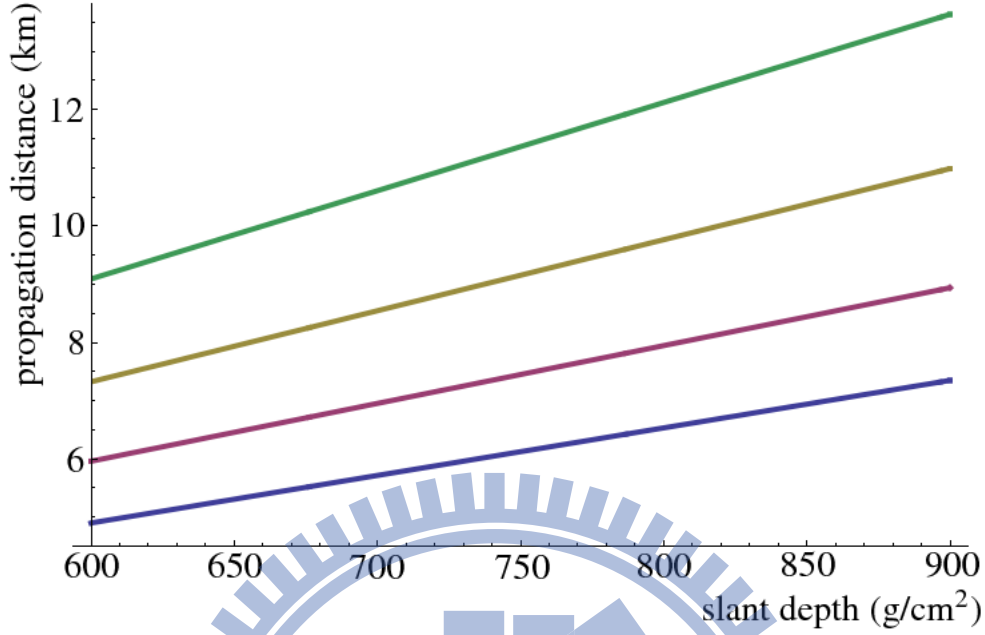


Figure 5.1: The relationship between slant depth and propagation distance in the air with constant density. Blue, red, yellow and green lines correspond to the transition rate for horizontal shower develop in sea level, 2 km, 4 km and 6 km altitudes. The densities of those altitudes are  $1.23 \text{ kg/m}^3$ ,  $1.01 \text{ kg/m}^3$ ,  $0.82 \text{ kg/m}^3$  and  $0.66 \text{ kg/m}^3$ .

The particle density is approximated by a parameterized function [47]

$$\rho(r, S, r_m) = \frac{N_e}{2\pi r_m^2} \left( \frac{\Gamma(4.5 - S)}{\Gamma(S)\Gamma(4.5 - 2S)} \right) \left( \frac{r}{r_m} \right)^{s-1} \left( 1 + \frac{r}{r_m} \right)^{s-4.5}, \quad (5.4)$$

where  $N_e$  is the number of particles,  $r_m$  is the Molière radius,  $S$  is shower age. Since the air shower travels long distance in the atmosphere, the density may change with the incident depth. The Molière radius must depend on the density of air; in other words, the Molière radius depend on altitudes

$$r_m(h) = r_m(h_o) \frac{\rho_{atm}(h_o)}{\rho_{atm}(h)}. \quad (5.5)$$

where  $h$  and  $h_o$  correspond to the altitudes at shower center and altitude at sea level. The value of Molière radius in the air at sea level is about 79 m. For hadronic shower, Eq. (5.4) can be represented by effective shower age,  $S' = 1.25S$ . Fig. 5.3, 5.6 and 5.9 show the lateral distribution at  $X_{max}$  for electron,  $\pi^-$  and  $K^-$  with energy between  $10^{16.5}$  to  $10^{18.5}$  eV.

The decay modes	Branching ratios	total ratio
$\tau^- \rightarrow \pi^- + \pi^0 + \nu_\tau$	$25.25 \pm 0.10\%$	25.25%
$\tau^- \rightarrow e^- + \bar{\nu}_e + \nu_\tau$	$17.85 \pm 0.05\%$	43.1%
$\tau^- \rightarrow \mu^- + \bar{\nu}_\mu + \nu_\tau$	$17.36 \pm 0.05\%$	60.46%
$\tau^- \rightarrow \pi^- + \nu_\tau$	$10.91 \pm 0.07\%$	71.37%
$\tau^- \rightarrow \pi^- + \pi^0 + \pi^0 + \nu_\tau$	$9.27 \pm 0.12\%$	80.64%
$\tau^- \rightarrow \pi^- + \pi^+ + \pi^- + \nu_\tau$	$8.99 \pm 0.12\%$	90.63%
others		100%

Table 5.2: The major branching ratios of  $\tau$ . There are 31 basic decay mode of  $\tau$ . The total branching ratio of first 6 decay channels is more than 90%.

## 5.2 CORSIKA Simulation

Tau decays to some daughter particles, which then initiate air shower. Table 5.2 lists the most possible six decay channels. The total decay ratio of those six modes is more than 90%.  $\pi^-$ ,  $\pi^0$ ,  $\pi^+$ ,  $e^-$  and  $\mu^-$  are the most abundant particles in tau decay. The pions and electrons generate air shower in the atmosphere immediately. Muons have a small cross section for interactions, hence the shower generated by muon in km level are rare. Using CORSIKA code [43], we simulate the showers initiated by pion, electron and kaon with five different energies. Those simulations show that the shower particles reside less than 1 m. Compared with the radiation which traverses a distance about 10 km, the shower front at the shower maximum is treated as longitudinally coherent. The remaining structures are the lateral profile and Lorentz factor distribution representing the spatial and energy distribution of the shower particles.

### 5.2.0.1 Electron Shower

The electron shower is an electromagnetic shower different from the hadronic shower,  $\pi^-$  or  $K^-$  shower. CORSIKA simulates the electron shower with five different energies,  $E_{e^-} = 10^{16.5}$ ,  $E_{e^-} = 10^{17.0}$ ,  $E_{e^-} = 10^{17.5}$ ,  $E_{e^-} = 10^{18.0}$  and  $E_{e^-} = 10^{18.5}$  eV. The mean longitudinal profile of 30 electron shower events are shown in Fig. 5.2. The depths of shower maximums,  $X_{max}$ , increases with the energy of primary electron. The mean shower maximum of electron shower with initial energy  $E_{e^-} = 10^{16.5}$  is  $710 \text{ g/cm}^2$  corresponds to 8.7 km propagation distance in 4 km altitudes. With the raising of energy, the mean shower maximum of primary electron with initial energy  $E_{e^-} = 10^{18.5}$  is  $890 \text{ g/cm}^2$  corresponds to 10.9 km propagation distance in 4 km

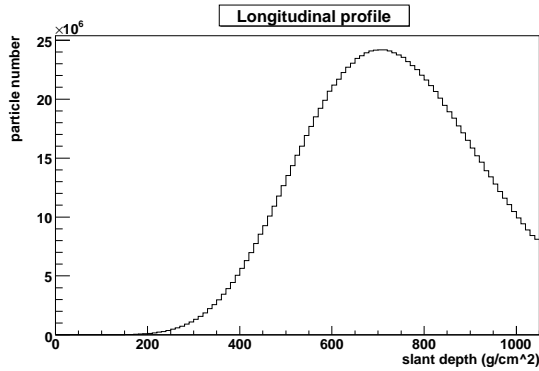
altitudes. The lateral distributions of shower at  $X_{max}$  are shown in Fig. 5.3. The particle numbers are proportional to the initial energy of primary particle. Fig. 5.4 shows the distributions of Lorentz factor at the  $X_{max}$ . The Lorentz factors of most particles are less than 150.

### 5.2.0.2 Pion Shower

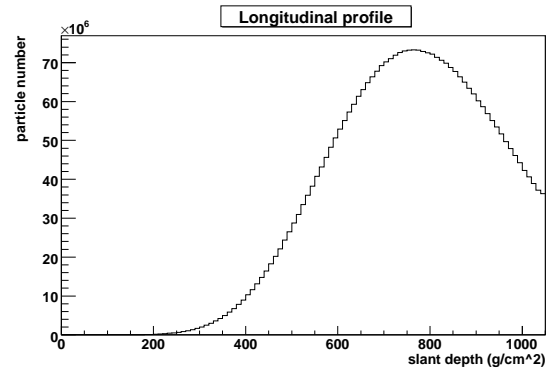
Pion is major component in tau decay channels. Different from electron, pion produces hadronic shower. We also using CORSIKA to simulate the pion shower at five different energies,  $E_{\pi^-} = 10^{16.5}$ ,  $E_{\pi^-} = 10^{17.0}$ ,  $E_{\pi^-} = 10^{17.5}$ ,  $E_{\pi^-} = 10^{18.0}$  and  $E_{\pi^-} = 10^{18.5}$  eV. The mean longitudinal profile of 30 pion showers are shown in Fig. 5.5. The shower maximums,  $X_{max}$ , are increasing with the energy of primary pion. Since the hadronic shower develop faster than the electromagnetic shower, the mean shower maximum of pion shower is shorter than the electron with the same initial energy. The mean shower maximum of pion shower with initial energy  $E_{\pi^-} = 10^{16.5}$  is  $650 \text{ g/cm}^2$  corresponds to 7.7 km propagation distance in 4 km altitudes. With the raising of energy, the mean shower maximum of primary pion with initial energy  $E_{\pi^-} = 10^{18.5}$  is  $750 \text{ g/cm}^2$  corresponds to 9.7 km propagation distance in 4 km altitudes. The lateral distributions of pion showers at  $X_{max}$  are shown in Fig. 5.6. The particle numbers are proportional to the initial energy of primary particle. Fig. 5.7 shows the distributions of Lorentz factor at the  $X_{max}$ .

### 5.2.0.3 Kaon Shower

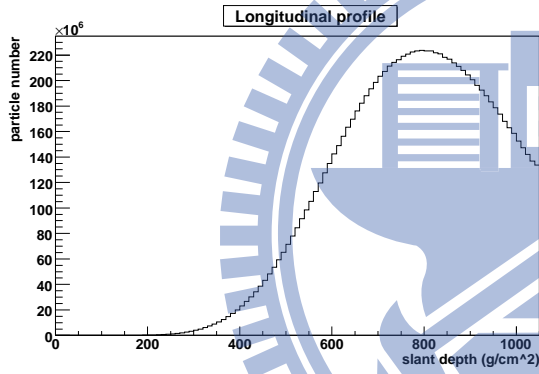
The kaon shower is rare contribution in tau decay. The kaon shower is a hadronic shower same as the pion shower. We also using CORSIKA to simulate the kaon shower at five different energies,  $E_{K^-} = 10^{16.5}$ ,  $E_{K^-} = 10^{17.0}$ ,  $E_{K^-} = 10^{17.5}$ ,  $E_{K^-} = 10^{18.0}$  and  $E_{K^-} = 10^{18.5}$  eV. The mean longitudinal profile of 30 kaon showers are shown in Fig. 5.8. The shower maximums,  $X_{max}$ , of pion shower spread between  $670 \text{ g/cm}^2$  to  $790 \text{ g/cm}^2$  correspond to  $E_{K^-} = 10^{16.5}$  and  $E_{K^-} = 10^{18.5}$  eV. The lateral distributions of kaon showers at  $X_{max}$  are shown in Fig. 5.9. The particle numbers are proportional to the initial energy of primary particle. Fig. 5.10 shows the distribution of Lorentz factor at the  $X_{max}$ .



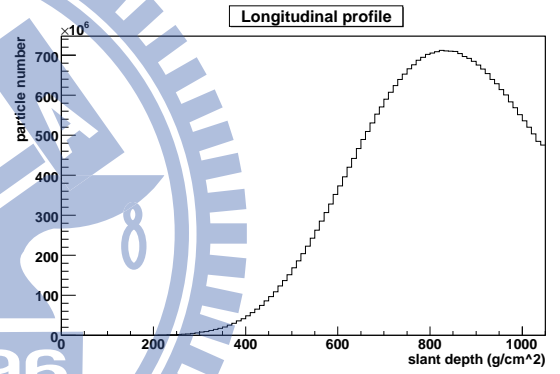
(a) The initial electron with energy  $E_{e^-} = 10^{16.5}$  eV hits atmosphere and generates the electromagnetic shower. The number of total particles at shower maximum,  $X_{max} = 710$  g/cm<sup>2</sup>, equals  $2.4 \times 10^7$ .



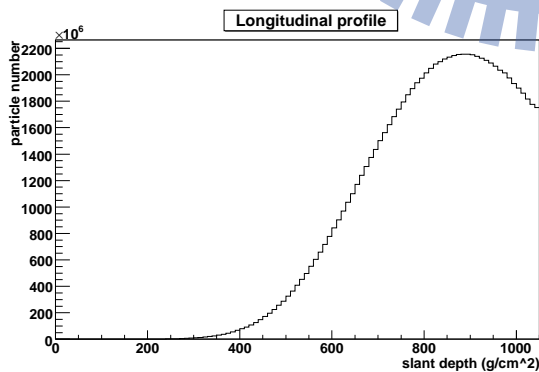
(b) The initial electron with energy  $E_{e^-} = 10^{17.0}$  eV hits atmosphere and generates the electromagnetic shower. The number of total particles at shower maximum,  $X_{max} = 770$  g/cm<sup>2</sup>, equals  $7.3 \times 10^7$ .



(c) The initial electron with energy  $E_{e^-} = 10^{17.5}$  eV hits atmosphere and generates the electromagnetic shower. The number of total particles at shower maximum,  $X_{max} = 800$  g/cm<sup>2</sup>, equals  $2.2 \times 10^8$ .

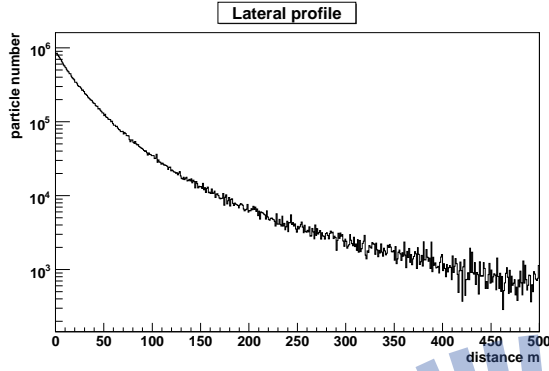


(d) The initial electron with energy  $E_{e^-} = 10^{18.0}$  eV hits atmosphere and generates the electromagnetic shower. The number of total particles at shower maximum,  $X_{max} = 830$  g/cm<sup>2</sup>, equals  $7.1 \times 10^8$ .

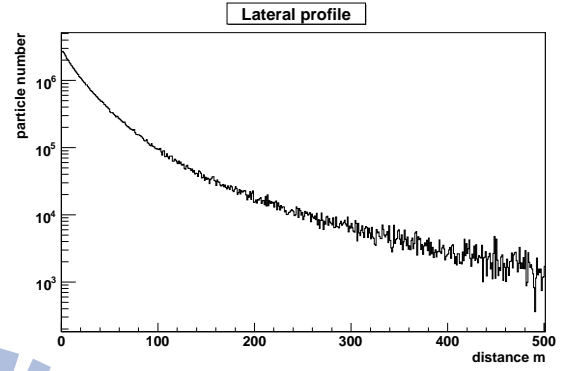


(e) The initial electron with energy  $E_{e^-} = 10^{18.5}$  eV hits atmosphere and generates the electromagnetic shower. The number of total particles at shower maximum,  $X_{max} = 890$  g/cm<sup>2</sup>, equals  $2.24 \times 10^9$ .

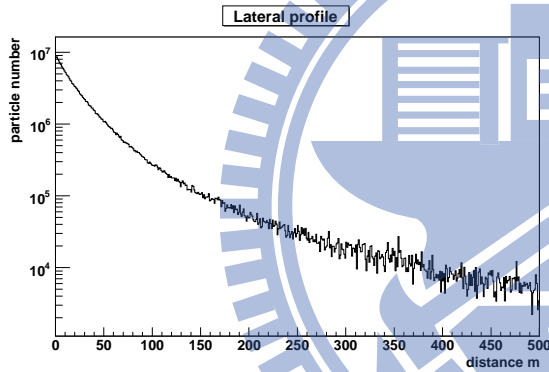
Figure 5.2: Mean longitudinal profile of 30 electron showers at five input energies.



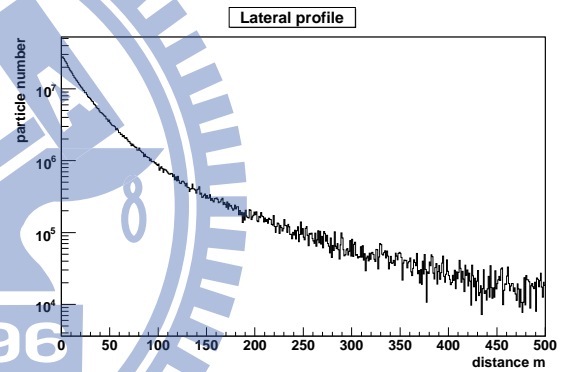
(a) The lateral profile of electron shower at shower maximum,  $X_{max} = 710 \text{ g/cm}^2$ , with initial energy  $E_{e^-} = 10^{16.5} \text{ eV}$ .



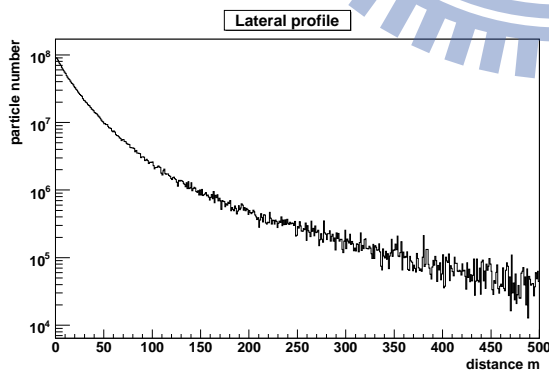
(b) The lateral profile of electron shower at shower maximum,  $X_{max} = 770 \text{ g/cm}^2$ , with initial energy  $E_{e^-} = 10^{17.0} \text{ eV}$ .



(c) The lateral profile of electron shower at shower maximum,  $X_{max} = 800 \text{ g/cm}^2$ , with initial energy  $E_{e^-} = 10^{17.5} \text{ eV}$ .

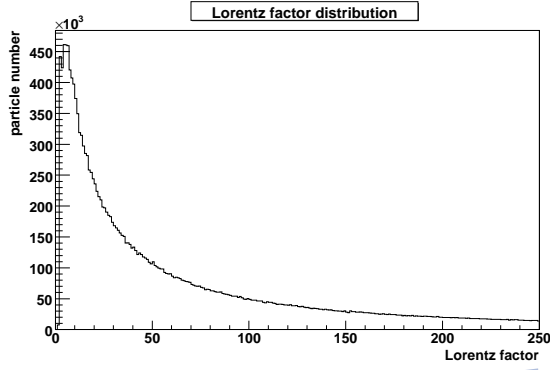


(d) The lateral profile of electron shower at shower maximum,  $X_{max} = 830 \text{ g/cm}^2$ , with initial energy  $E_{e^-} = 10^{18.0} \text{ eV}$ .

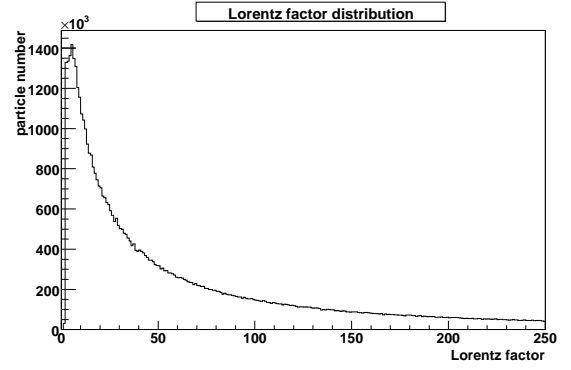


(e) The lateral profile of electron shower at shower maximum,  $X_{max} = 890 \text{ g/cm}^2$ , with initial energy  $E_{e^-} = 10^{18.5} \text{ eV}$ .

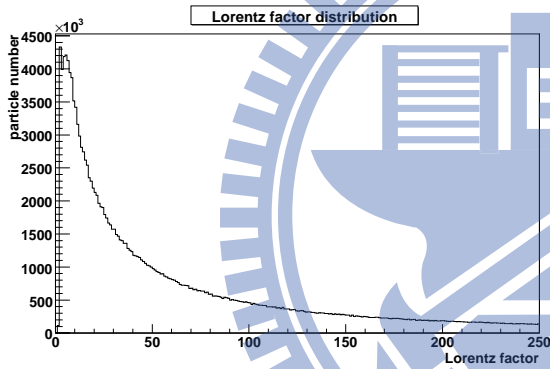
Figure 5.3: Lateral profile of electron showers at five input energies.



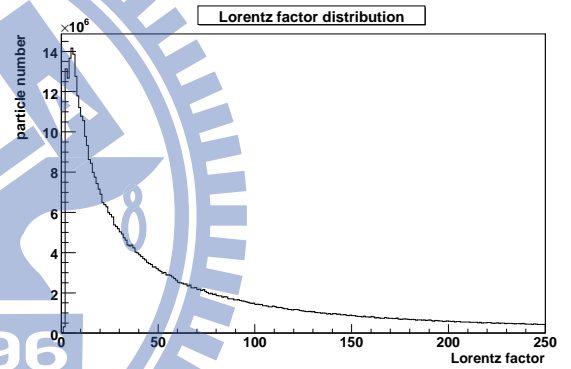
(a) The Lorentz factor distribution of electron shower at shower maximum,  $X_{max} = 710 \text{ g/cm}^2$ , with initial energy  $E_{e^-} = 10^{16.5}$  eV.



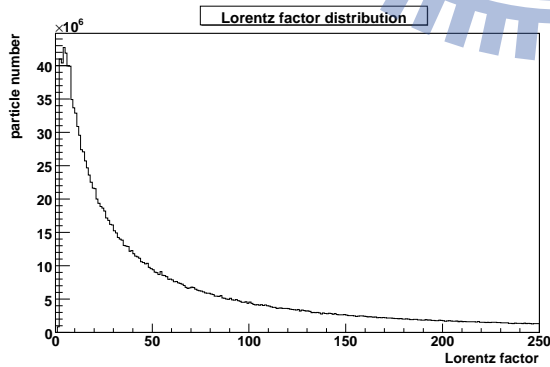
(b) The Lorentz factor distribution of electron shower at shower maximum,  $X_{max} = 770 \text{ g/cm}^2$ , with initial energy  $E_{e^-} = 10^{17.0}$  eV.



(c) The Lorentz factor distribution of electron shower at shower maximum,  $X_{max} = 800 \text{ g/cm}^2$ , with initial energy  $E_{e^-} = 10^{17.5}$  eV.

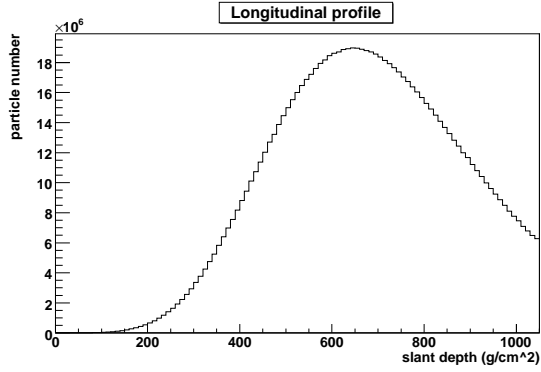


(d) The Lorentz factor distribution of electron shower at shower maximum,  $X_{max} = 830 \text{ g/cm}^2$ , with initial energy  $E_{e^-} = 10^{18.0}$  eV.

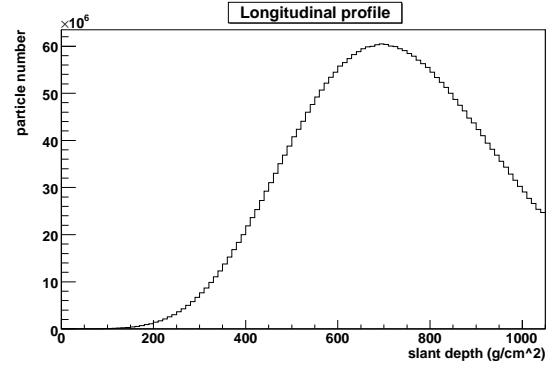


(e) The Lorentz factor distribution of electron shower at shower maximum,  $X_{max} = 890 \text{ g/cm}^2$ , with initial energy  $E_{e^-} = 10^{18.5}$  eV.

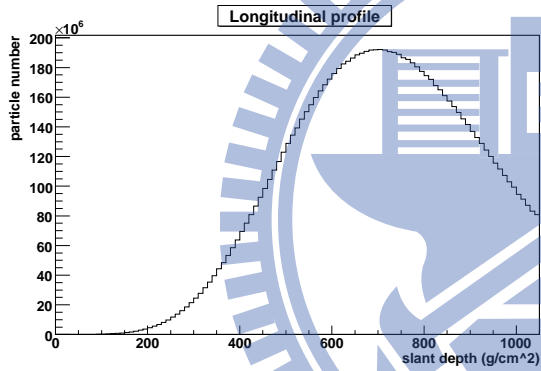
Figure 5.4: Lorentz factor distribution of electron showers at five input energies.



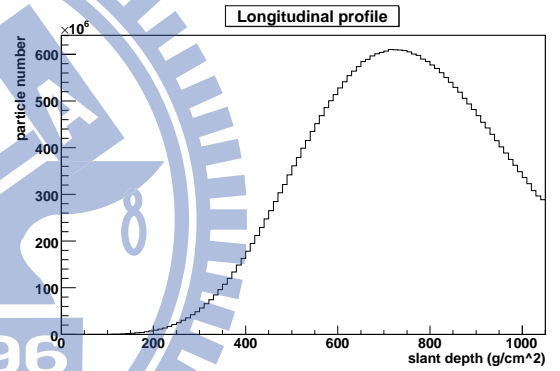
(a) The initial  $\pi^-$  with energy  $E_{\pi^-} = 10^{16.5}$  eV hits atmosphere and genetares the hadronic shower. The number of total particles at shower maximum,  $X_{max} = 650$  g/cm<sup>2</sup>, equals  $1.89 \times 10^7$ .



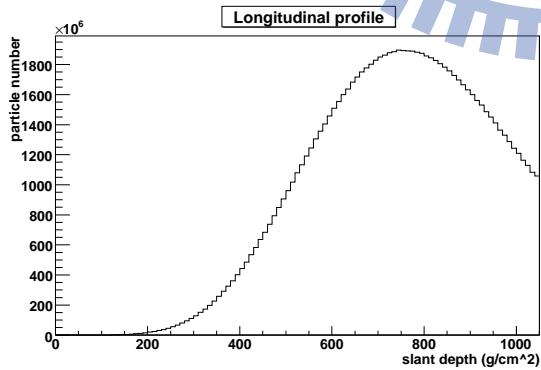
(b) The initial  $\pi^-$  with energy  $E_{\pi^-} = 10^{17.0}$  eV hits atmosphere and genetares the hadronic shower. The number of total particles at shower maximum,  $X_{max} = 700$  g/cm<sup>2</sup>, equals  $6.05 \times 10^7$ .



(c) The initial  $\pi^-$  with energy  $E_{\pi^-} = 10^{17.5}$  eV hits atmosphere and genetares the hadronic shower. The number of total particles at shower maximum,  $X_{max} = 650$  g/cm<sup>2</sup>, equals  $1.97 \times 10^7$ .



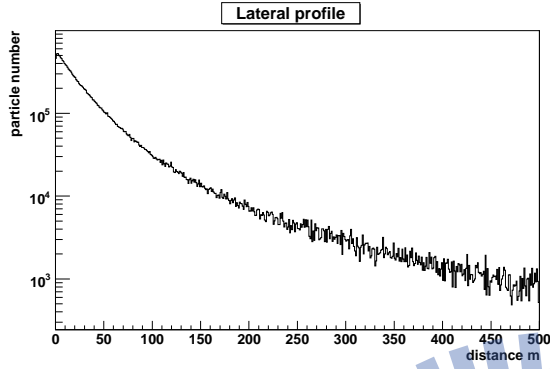
(d) The initial  $\pi^-$  with energy  $E_{\pi^-} = 10^{18.0}$  eV hits atmosphere and genetares the hadronic shower. The number of total particles at shower maximum,  $X_{max} = 720$  g/cm<sup>2</sup>, equals  $6.10 \times 10^8$ .



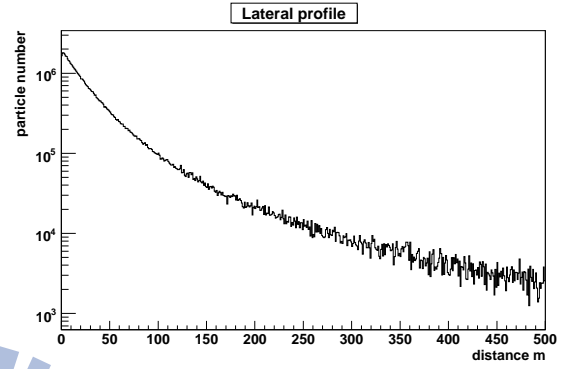
(e) The initial  $\pi^-$  with energy  $E_{\pi^-} = 10^{18.5}$  eV hits atmosphere and genetares the hadronic shower. The number of total particles at shower maximum,  $X_{max} = 750$  g/cm<sup>2</sup>, equals  $1.89 \times 10^9$ .

Figure 5.5: longitudinal profile of pion showers at five input energies.

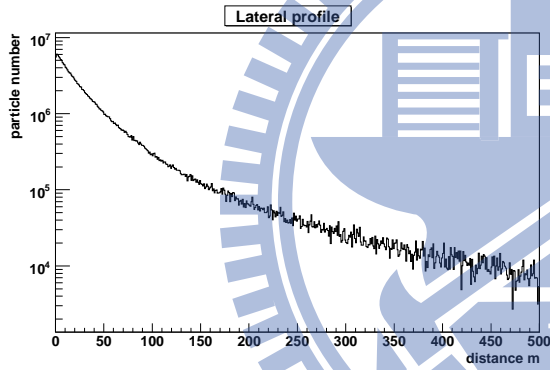




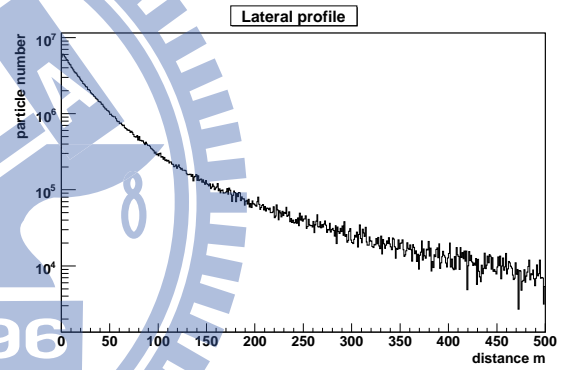
(a) The lateral profile of  $\pi^-$  shower at shower maximum,  $X_{max} = 650 \text{ g/cm}^2$ , with initial energy  $E_{\pi^-} = 10^{16.5} \text{ eV}$ .



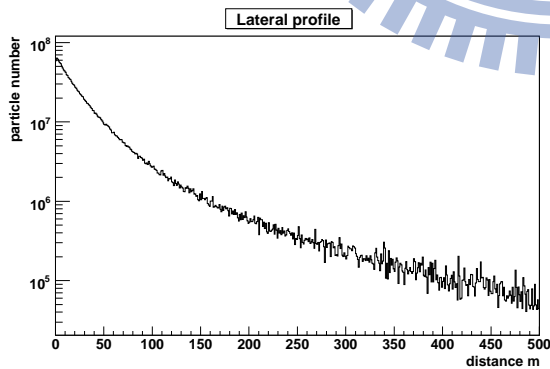
(b) The lateral profile of  $\pi^-$  shower at shower maximum,  $X_{max} = 700 \text{ g/cm}^2$ , with initial energy  $E_{\pi^-} = 10^{17.0} \text{ eV}$ .



(c) The lateral profile of  $\pi^-$  shower at shower maximum,  $X_{max} = 710 \text{ g/cm}^2$ , with initial energy  $E_{\pi^-} = 10^{17.5} \text{ eV}$ .

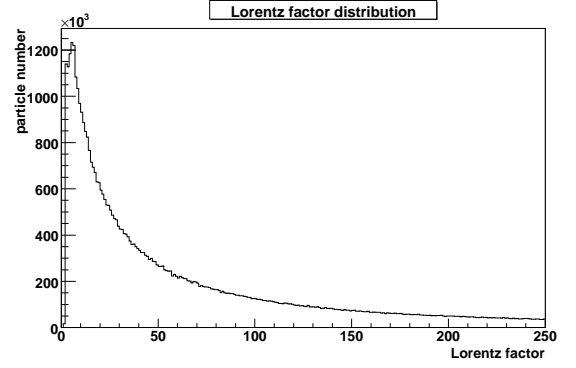
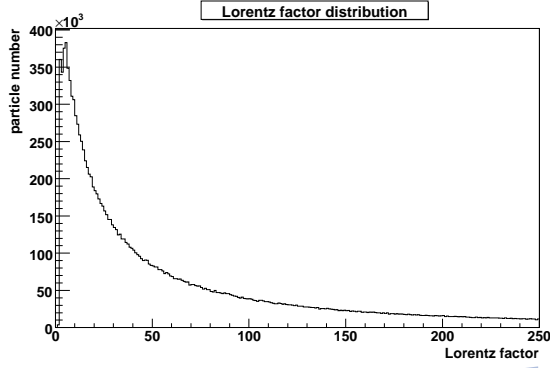


(d) The lateral profile of  $\pi^-$  shower at shower maximum,  $X_{max} = 720 \text{ g/cm}^2$ , with initial energy  $E_{\pi^-} = 10^{18.0} \text{ eV}$ .



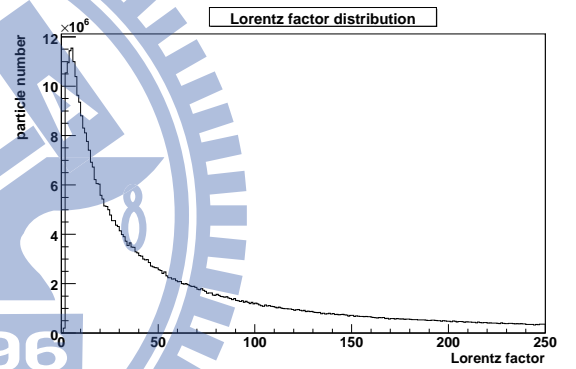
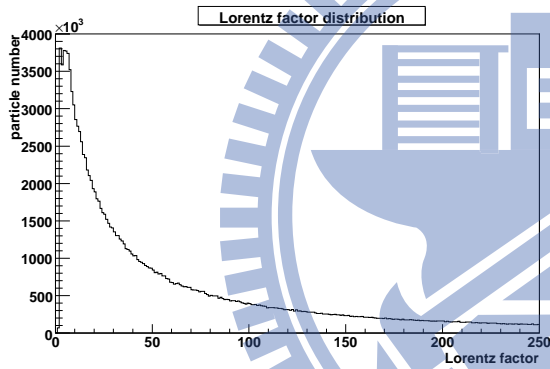
(e) The lateral profile of  $\pi^-$  shower at shower maximum,  $X_{max} = 750 \text{ g/cm}^2$ , with initial energy  $E_{\pi^-} = 10^{18.5} \text{ eV}$ .

Figure 5.6: longitudinal profile of pion showers at five input energies.



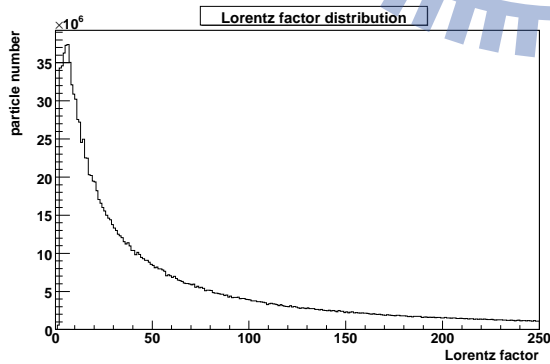
(a) The Lorentz factor distribution of  $\pi^-$  shower at shower maximum,  $X_{max} = 650 \text{ g/cm}^2$ , with initial energy  $E_{\pi^-} = 10^{16.5}$  eV.

(b) The Lorentz factor distribution of  $\pi^-$  shower at shower maximum,  $X_{max} = 700 \text{ g/cm}^2$ , with initial energy  $E_{\pi^-} = 10^{17.0}$  eV.



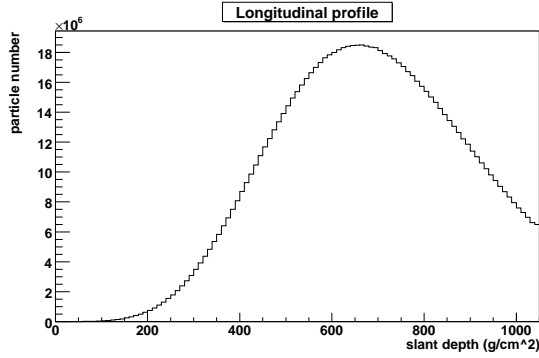
(c) The Lorentz factor distribution of  $\pi^-$  shower at shower maximum,  $X_{max} = 710 \text{ g/cm}^2$ , with initial energy  $E_{\pi^-} = 10^{17.5}$  eV.

(d) The Lorentz factor distribution of  $\pi^-$  shower at shower maximum,  $X_{max} = 720 \text{ g/cm}^2$ , with initial energy  $E_{\pi^-} = 10^{18.0}$  eV.

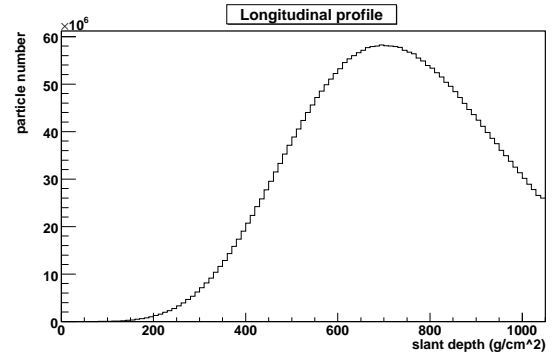


(e) The Lorentz factor distribution of  $\pi^-$  shower at shower maximum,  $X_{max} = 750 \text{ g/cm}^2$ , with initial energy  $E_{\pi^-} = 10^{18.5}$  eV.

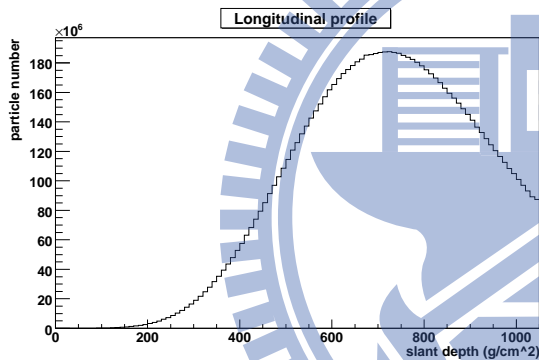
Figure 5.7: The longitudinal profile of pion showers at five input energies.



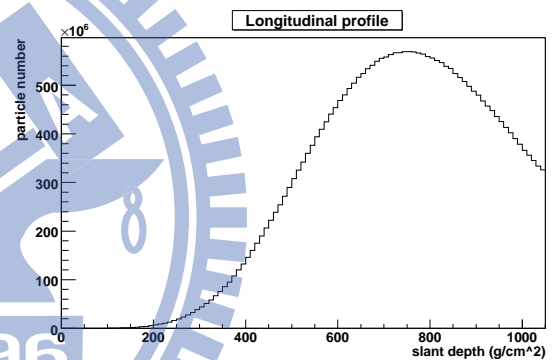
(a) The initial  $K^-$  with energy  $E_{K^-} = 10^{16.5}$  eV hits atmosphere and generates the hadronic shower. The number of total particles at shower maximum,  $X_{max} = 670$  g/cm<sup>2</sup>, equals  $1.84 \times 10^7$ .



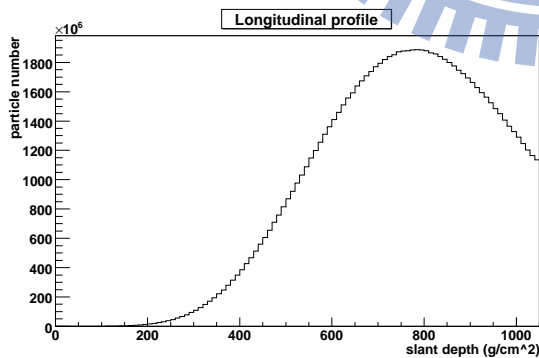
(b) The initial  $K^-$  with energy  $E_{K^-} = 10^{17.0}$  eV hits atmosphere and generates the hadronic shower. The number of total particles at shower maximum,  $X_{max} = 700$  g/cm<sup>2</sup>, equals  $5.82 \times 10^7$ .



(c) The initial  $K^-$  with energy  $E_{K^-} = 10^{17.5}$  eV hits atmosphere and generates the hadronic shower. The total particle number at shower maximum,  $X_{max} = 730$  g/cm<sup>2</sup>, equals  $1.87 \times 10^8$ .

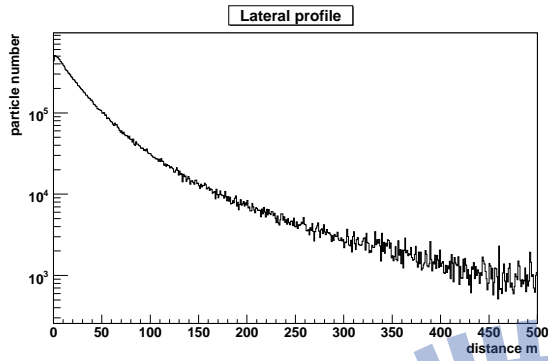


(d) The initial  $K^-$  with energy  $E_{K^-} = 10^{18.0}$  eV hits atmosphere and generates the hadronic shower. The number of total particles at shower maximum,  $X_{max} = 760$  g/cm<sup>2</sup>, equals  $5.69 \times 10^8$ .

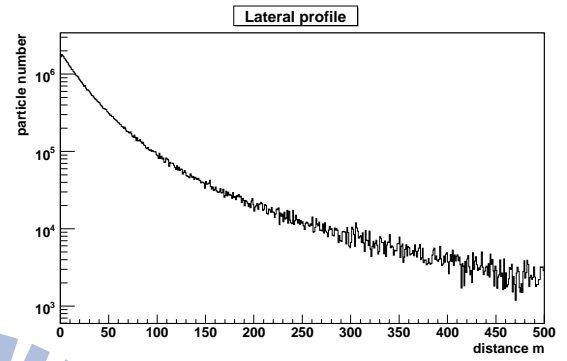


(e) The initial  $K^-$  with energy  $E_{K^-} = 10^{18.5}$  eV hits atmosphere and generates the hadronic shower. The number of total particles at shower maximum,  $X_{max} = 790$  g/cm<sup>2</sup>, equals  $1.88 \times 10^9$ .

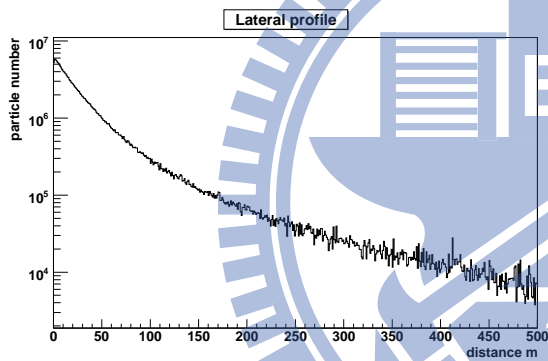
Figure 5.8: longitudinal profile of kaon showers at five input energies.



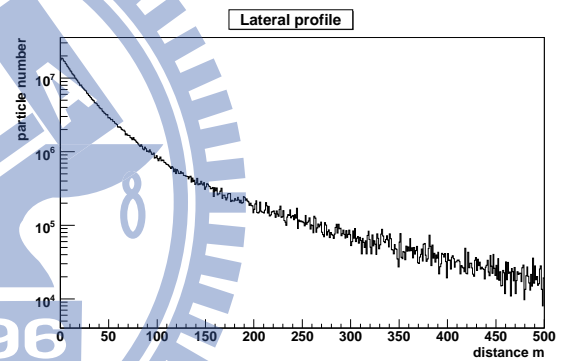
(a) The lateral profile of  $K^-$  shower at shower maximum,  $X_{max} = 670 \text{ g/cm}^2$ , with initial energy  $E_{K^-} = 10^{16.5} \text{ eV}$ .



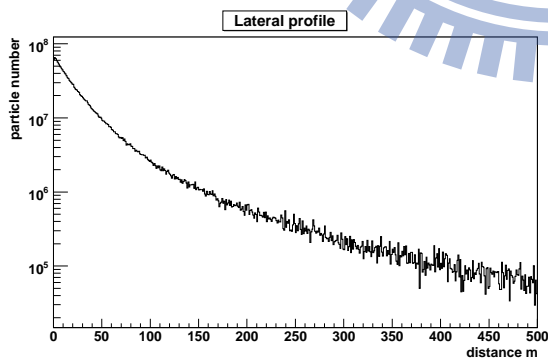
(b) The lateral profile of  $K^-$  shower at shower maximum,  $X_{max} = 700 \text{ g/cm}^2$ , with initial energy  $E_{K^-} = 10^{17.0} \text{ eV}$ .



(c) The lateral profile of  $K^-$  shower at shower maximum,  $X_{max} = 730 \text{ g/cm}^2$ , with initial energy  $E_{K^-} = 10^{17.5} \text{ eV}$ .

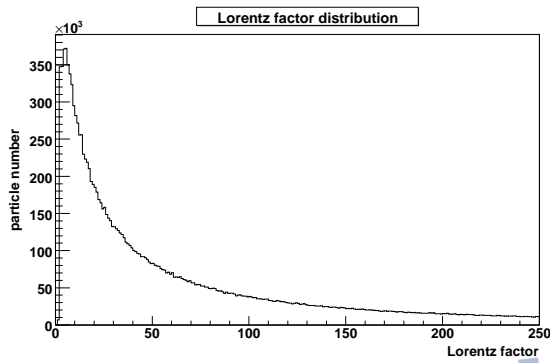


(d) The lateral profile of  $K^-$  shower at shower maximum,  $X_{max} = 760 \text{ g/cm}^2$ , with initial energy  $E_{K^-} = 10^{18.0} \text{ eV}$  hits.

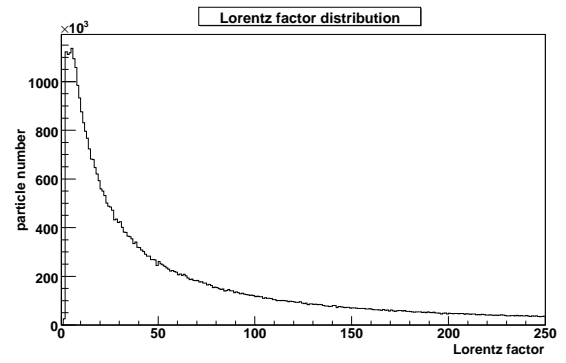


(e) The lateral profile of  $K^-$  shower at shower maximum,  $X_{max} = 790 \text{ g/cm}^2$ , with initial energy  $E_{K^-} = 10^{18.5} \text{ eV}$ .

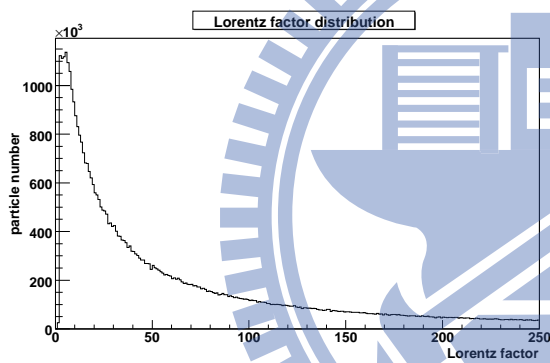
Figure 5.9: The lateral profile of kaon showers at five input energies.



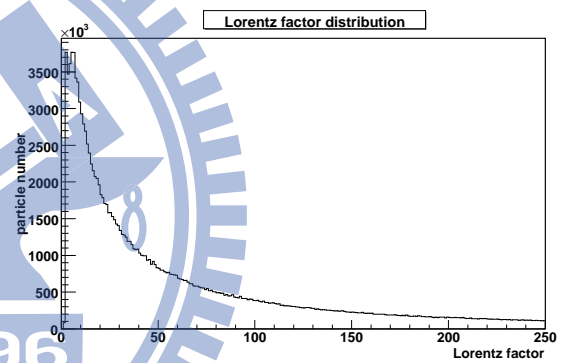
(a) The Lorentz factor distribution of  $K^-$  shower at shower maximum,  $X_{max} = 670 \text{ g/cm}^2$ , with initial energy  $E_{K^-} = 10^{16.5}$  eV.



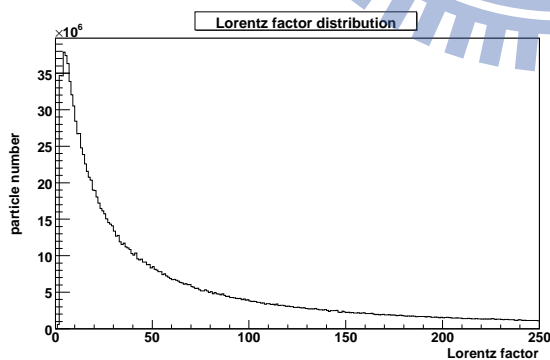
(b) The Lorentz factor distribution of  $K^-$  shower at shower maximum,  $X_{max} = 700 \text{ g/cm}^2$ , with initial energy  $E_{K^-} = 10^{17.0}$  eV.



(c) The Lorentz factor distribution of  $K^-$  shower at shower maximum,  $X_{max} = 730 \text{ g/cm}^2$ , with initial energy  $E_{K^-} = 10^{17.5}$  eV.



(d) The Lorentz factor distribution of  $K^-$  shower at shower maximum,  $X_{max} = 760 \text{ g/cm}^2$ , with initial energy  $E_{K^-} = 10^{18.0}$  eV.



(e) The Lorentz factor distribution of  $K^-$  shower at shower maximum,  $X_{max} = 790 \text{ g/cm}^2$ , with initial energy  $E_{K^-} = 10^{18.5}$  eV.

Figure 5.10: The Lorentz factor distribution of kaon showers at five input energies.

## 5.3 Radiation Emission from Air Shower

### 5.3.1 Radiation by a Moving Charge

We first consider a charged particle moves with speed  $\vec{v}$  in the atmosphere, the magnetic force caused by earth's magnetic field may deflect the particle. If the angle between magnetic field  $\vec{B}$  and the particle's velocity  $\vec{v}$  is  $\alpha$ , the radius of the path is given by

$$\rho = \frac{v\gamma mc}{eB \sin \alpha}, \quad (5.6)$$

where  $\gamma$  is Lorentz factor,  $m$  is the mass of charged particle,  $e$  is the charge of particle. Such a particle emit the radiation in a narrow cone in the direction of the velocity vector. The detector observes a short pulse of radiation. Jackson defines the power radiated per unit solid angle as [48]

$$A(R, \omega) = \frac{e\omega}{\sqrt{8c\pi}} e^{i(\omega \frac{R}{c} - \frac{\pi}{2})} (-\hat{e}_{\parallel} A_{\parallel}(\omega) + \hat{e}_{\perp} A_{\perp}(\omega)), \quad (5.7)$$

where  $\omega = 2\pi\nu$  is the angular frequency corresponding to the observed frequency,  $R$  is the distance to the detector,  $\hat{e}_{\parallel}$  is the unit vector corresponding to polarization in the plane of the orbit,  $\hat{e}_{\perp}$  is the orthogonal polarization. The  $A(R, \omega)$  in Eq. (5.11) is assumed real. The definition of  $A_{\parallel}(\omega)$  and  $A_{\perp}(\omega)$  is

$$A_{\parallel}(\omega) = \left(\frac{\rho}{c}\right) \left(\frac{1}{\gamma^2} + \theta^2\right) \int_{-\infty}^{\infty} x \exp\left[i\frac{3}{2}\xi \left(x + \frac{1}{3}x^3\right)\right] dx = i\left(\frac{\rho}{\sqrt{3}c}\right) \left(\frac{1}{\gamma^2} + \theta^2\right) K_{2/3}(\xi),$$

$$A_{\perp}(\omega) = \left(\frac{\rho\theta}{c}\right) \left(\frac{1}{\gamma^2} + \theta^2\right)^{1/2} \int_{-\infty}^{\infty} \exp\left[i\frac{3}{2}\xi \left(x + \frac{1}{3}x^3\right)\right] dx = \theta \left(\frac{\rho}{\sqrt{3}c}\right) \left(\frac{1}{\gamma^2} + \theta^2\right)^{1/2} K_{1/3}(\xi), \quad (5.8)$$

where  $\xi \equiv \frac{\omega\rho}{3c} \left(\frac{1}{\gamma^2} + \theta^2\right)^{3/2}$ . The integrals in Eq. (5.8) are identifiable as modified Bessel functions. The radiated energy per unit frequency interval per solid angle is

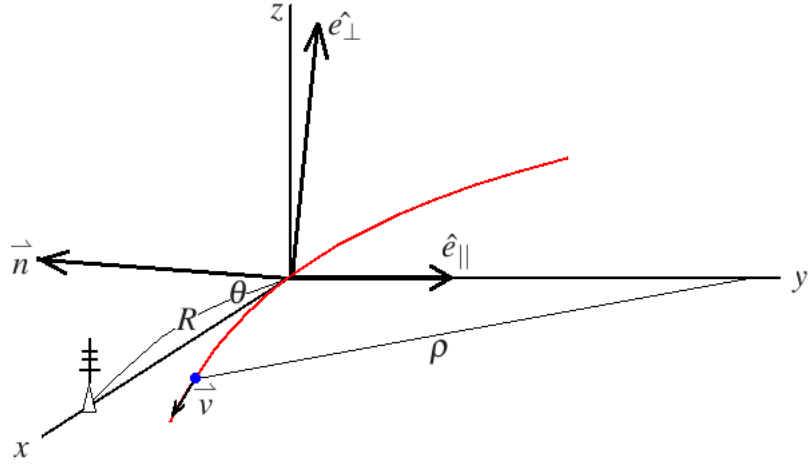


Figure 5.11: Geometry of synchrotron radiation. Blue point denotes the particle moving with velocity  $v$ . Red line is the trajectory of particle lies in  $x-y$  plane with radius  $\rho$ .  $\hat{e}_{\parallel}$  is the unit vector corresponding to the polarization in the plane of orbit and  $\hat{e}_{\perp}$  is the unit vector of the other polarization, which perpendicular to the  $\hat{e}_{\parallel}$  and emission direction  $n$ .

$$\frac{d^2I}{d\omega d\Omega} = 2|A(R, \omega)|^2 = \frac{4e^2}{3\pi c^2} \left(\frac{\omega\rho}{c}\right)^2 \left(\frac{1}{\gamma^2} + \theta^2\right)^2 \times \left[ K_{2/3}^2(\xi) + \frac{\theta^2}{(1+\gamma^2) + \theta^2} K_{1/3}^2(\xi) \right], \quad (5.9)$$

where  $\theta$  is emission angle. The frequency component of E-field with the specific distance,  $R$ , to the detector can be calculated as

$$E(R, \omega) = \sqrt{\frac{4\pi}{c}} \frac{1}{R} A(R, \omega). \quad (5.10)$$

### 5.3.2 The Radiation form the Electron-positron Pairs

In air shower, electron and positron are generated in pair. The trajectories of electron and positron are mirrored. Due to the symmetric trajectories, the magnitude of  $A_{\perp}(\omega)$  from positron is same as the magnitude of electron, but opposite sign. Hence the contributions of  $A_{\perp}(\omega)$  from electron-positron pair cancel each other. The magnitudes of  $A_{\parallel}(\omega)$  from electron and positron are same, the contribution from  $A_{\parallel}(\omega)$  double to  $2A_{\parallel}(\omega)$ . In other words, the contribution of  $A_{\parallel}(\omega)$  is proportional to the number of particles. The result allows us to neglect the difference between electron and positron. The spectrum emitted by an individual particle can be written as

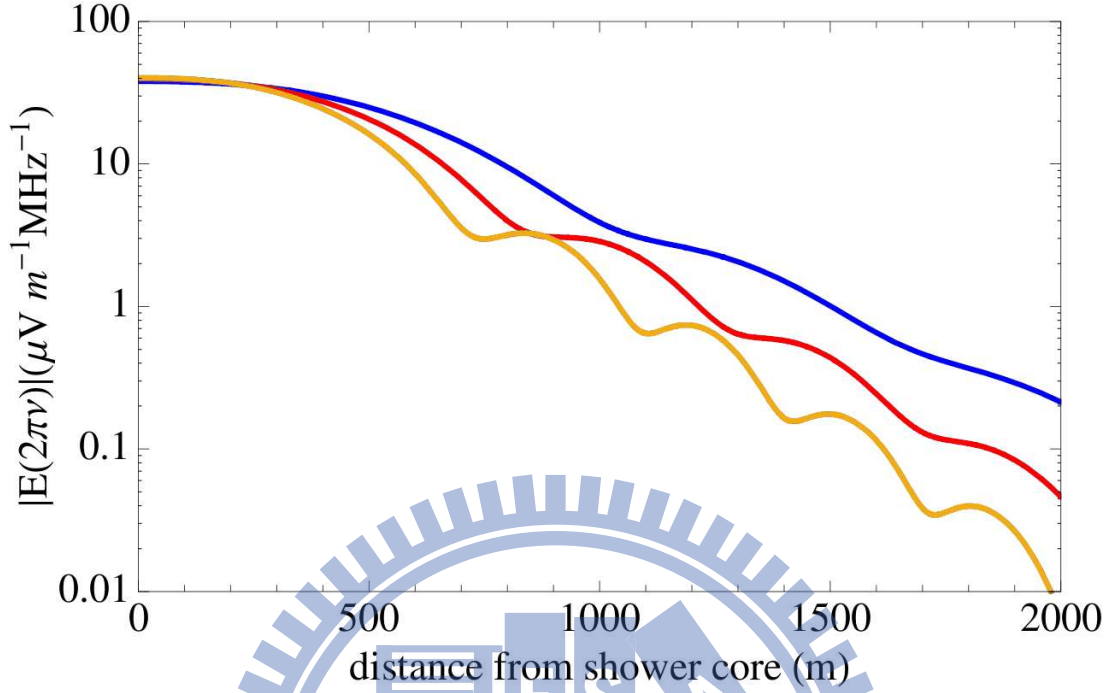


Figure 5.12: Off-set dependence of  $|E(R, 2\pi\nu)|$  of a  $10^{17}$  eV shower at the observation distance of 10 km. Curves in blue, red and orange represent signals in observing frequencies of 50 MHz, 75 MHz and 100 MHz respectively.

$$E(R, \omega) = \frac{1}{\sqrt{2\pi}} \frac{e\omega}{cR} e^{i(\omega\frac{R}{c} - \frac{\pi}{2})} (-\hat{e}_{||} A_{||}(\omega)). \quad (5.11)$$

Applying the lateral and Lorentz distribution from CORSIKA simulation. The observed signals in different frequency can be calculated from Eq. (5.11). Fig. 5.12 shows the strength of electric field at the observation distance of 10 km from  $10^{17}$  eV electron shower in different frequency. The strength decrease rapidly with the distance from shower core. The Figs. 5.14 and 5.15 show the pulses from pion and kaon shower. The signals of pion and kaon shower can not be distinguished with the same energy.

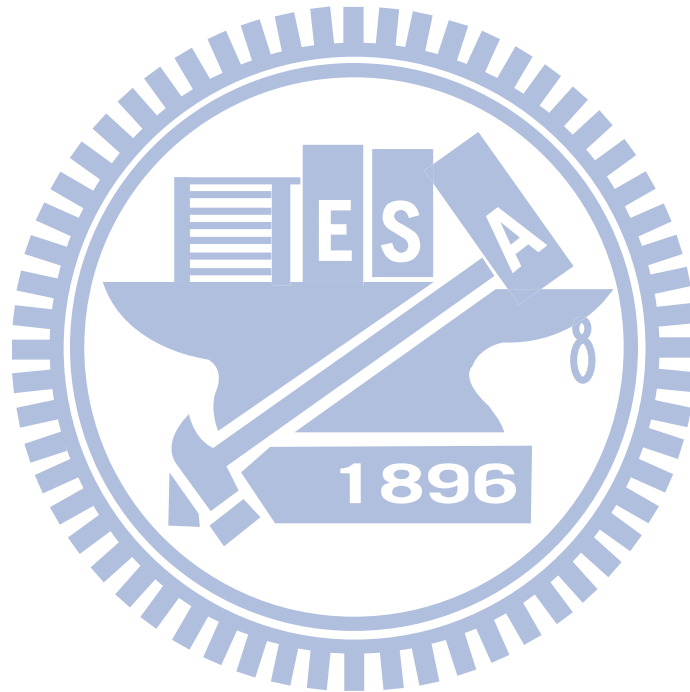
### 5.3.3 Pulse Reconstruction

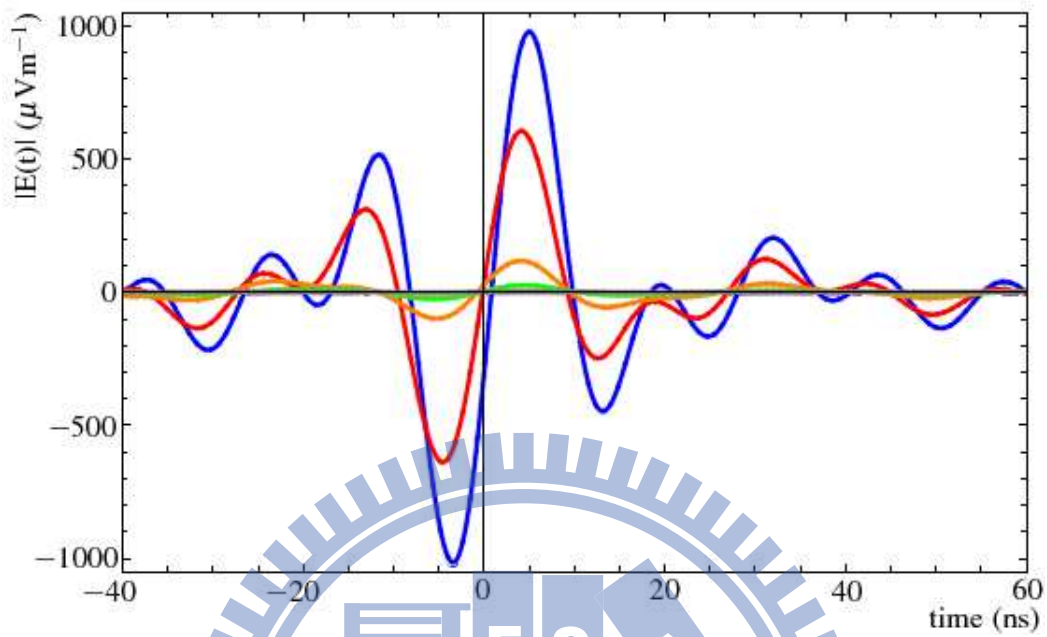
The time-dependence electric field  $E(R, t)$  can be reconstructed by an inverse Fourier-transform of the  $E(R, \omega)$ .



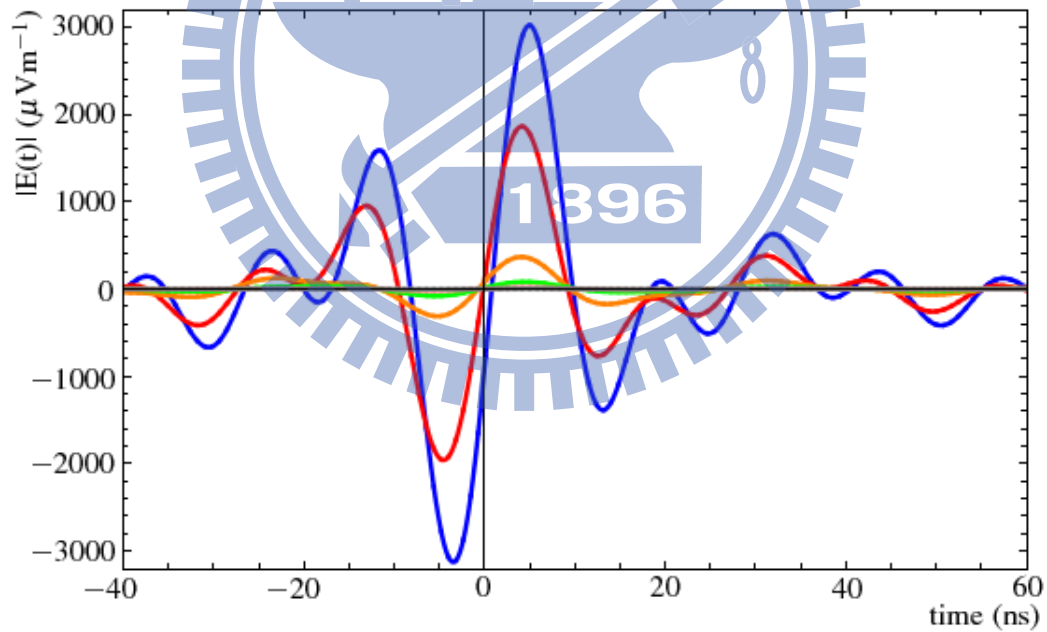
$$E(R,t) = \frac{1}{\sqrt{2\pi}} \int_{-\infty}^{\infty} b(\omega)E(R,\omega)e^{-i\omega t} d\omega, \quad (5.12)$$

where  $b(\omega)$  is the characteristic frequency of the detector. The reconstructed pulses from emission of  $10^{17}$  and  $10^{17.5}$  eV electron shower at the observation distance of 10 km, using an idealized rectangular filter spanning 30 – 80 MHz are shown in Fig. 5.13. Since the lateral and Lorentz factor distribution in this energy can be parameterized by energy. The strength of pulses are proportional to the energies of showers.





(a) Reconstructed pulses from emission of a  $10^{17.0}$  eV electron shower at the observation distance of 10 km



(b) Reconstructed pulses from emission of a  $10^{17.5}$  eV electron shower at the observation distance of 10 km

Figure 5.13: Reconstructed pulses from emission of  $10^{17}$  and  $10^{17.5}$  eV electron shower at the observation distance of 10 km, using an idealized rectangular filter spanning 30 – 80 MHz. The strength of signal is proportional to the energy of shower. The curves in blue, red, orange and green denote pulses measured at center, at lateral distances of 500 m 1000 m and 1500 m, respectively. The pink and gray curves are measured at lateral distances of 2000 m and 2500 m and close to the  $x$  axis, and the signals are too weak to be distinguished.

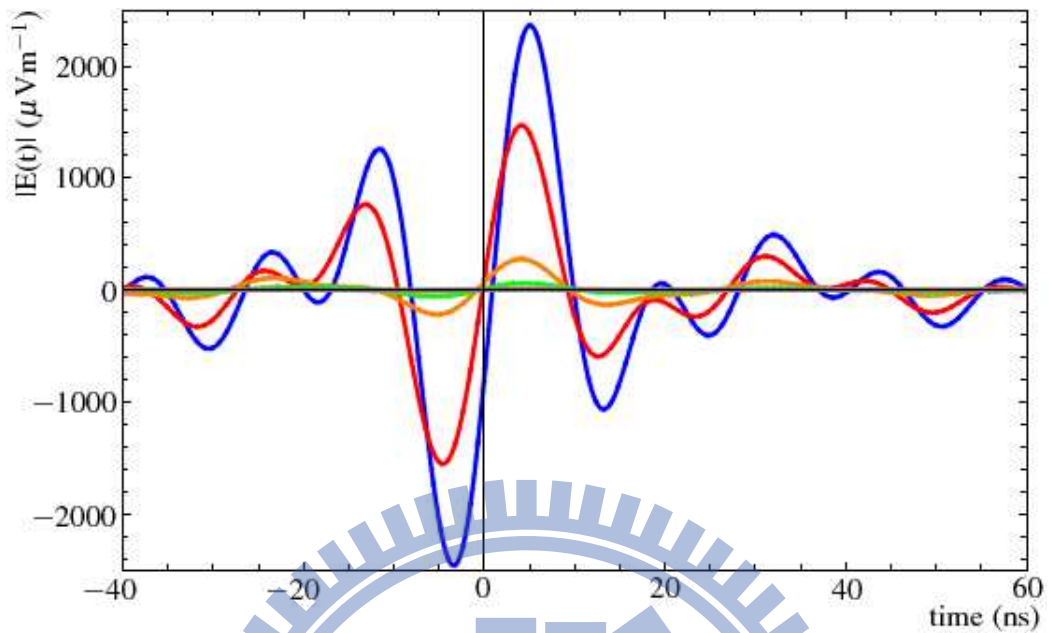


Figure 5.14: Reconstructed pulses from emission of a  $10^{17.5}$  eV pion shower at the observation distance of 10 km, using an idealized rectangular filter spanning 30 – 80 MHz. The curves in blue, red, orange and green denote pulses measured at center, at lateral distances of 500 m 1000 m and 1500 m, respectively. The pink and gray curves are measured at lateral distances of 2000 m and 2500 m and close to the  $x$  axis, and the signals are too weak to be distinguished.

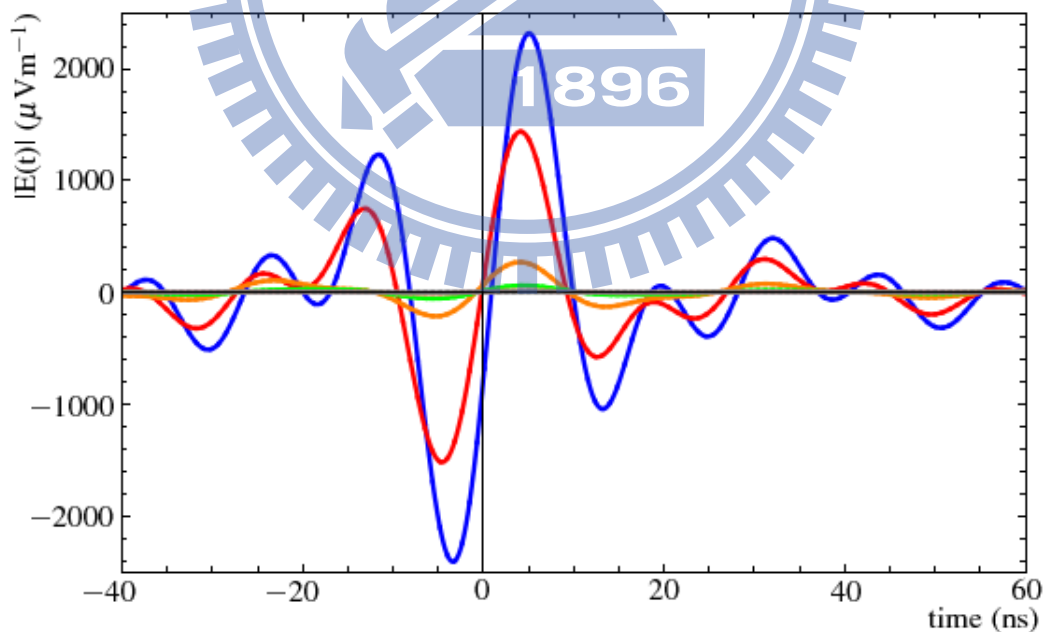


Figure 5.15: Reconstructed pulses from emission of a  $10^{17.5}$  eV kaon shower at the observation distance of 10 km, using an idealized rectangular filter spanning 30 – 80 MHz. The curves in blue, red, orange and green denote pulses measured at center, at lateral distances of 500 m 1000 m and 1500 m, respectively. The pink and gray curves are measured at lateral distances of 2000 m and 2500 m and close to the  $x$  axis, and the signals are too weak to be distinguished.

## Chapter 6

# Shower Experiment with electron beam

Shower development can be separated to orthogonal parts, longitudinal development along the shower axis and lateral development perpendicular to shower axis. Simulation must be consistent with both development. It is important to longitudinal and lateral profile simultaneously. Such studies, called FLASH-TW, are carried out with Taiwan's NSRRC 1.5 GeV electron beam [62]. Although the beam energy is only 1.5 GeV, the beam current is large enough to produce a total energy of the order 0.1 to 1 EeV. We perform the shower profile measurement by shooting the NSRRC 1.5 GeV electron beams on aluminum targets. The shower parameters of aluminum are comparable to those of alumina used in the FLASH experiment [63]. The radiation length of aluminum is  $24.01 \text{ g/cm}^2$  compared to  $27.94 \text{ g/cm}^2$  of  $\text{Al}_2\text{O}_3$  while the radiation length of aluminum is 52.55 MeV compared to 54 MeV of  $\text{Al}_2\text{O}_3$ . In this chapter, we apply two different detection methods to reconstruct the shower profiles. The first method applying a scintillator to convert the shower particles to photons and record photons by CCD camera. The other method detects the Cherenkov light, which emitted by relativistic particles passing through air. Based on the data recorded by CCD camera, the longitudinal and lateral profiles of shower can be reconstructed.

### 6.1 Instrument

The main instrument used in FLASH-TW is a platform of two chambers and a removable aluminum blocks system which contains 15 aluminum blocks. Each block can be moved in or out of the beam path. Therefore, it is possible to study shower longitudinal profile in 15 steps, with

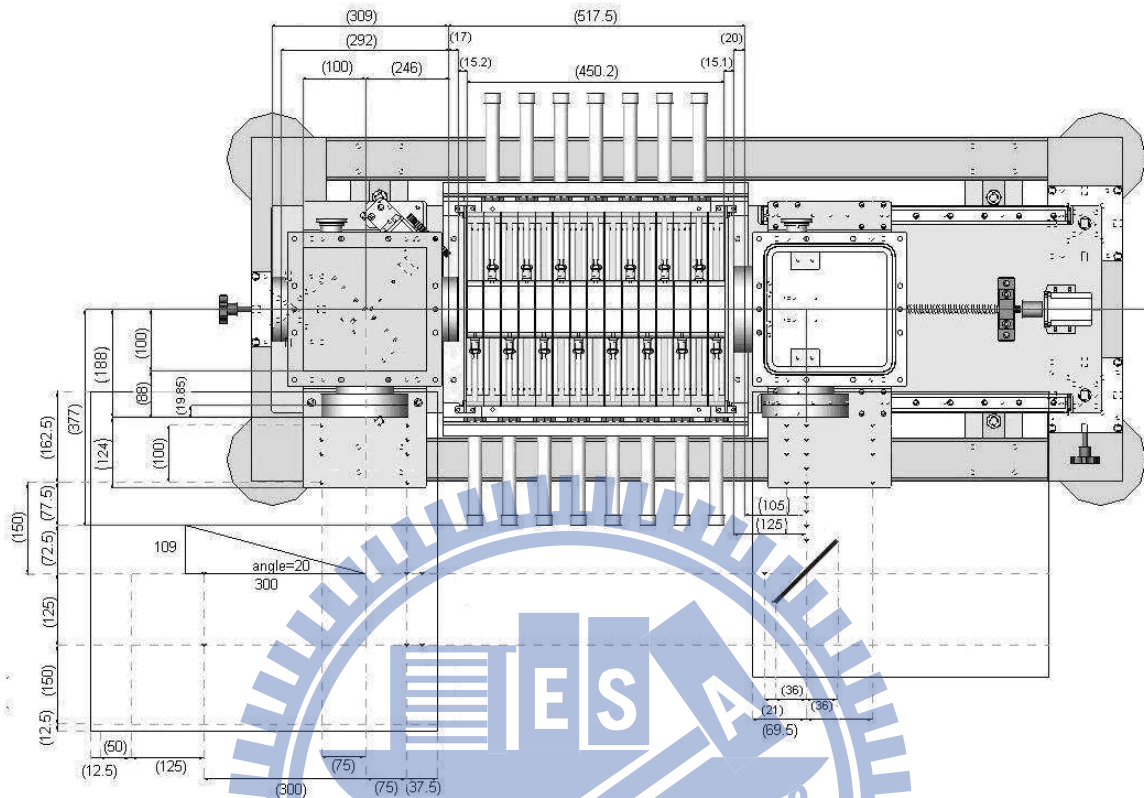


Figure 6.1: Top view of the experimental platform. The 1.5 GeV electron beams enter the chambers from the left hand side. The secondary charge particles are generated while incident electrons are passing through the aluminum targets. The secondary charge particles hit the scintillation screen placed in the second chamber and generate scintillation light, which is recorded by the CCD camera.

an increment of  $1/3$  radiation length ( $r.l.$ ) per step. Fig. 6.1 shows the top view of the experimental platform. Left chamber contains a 6-hole wheel which can accommodate several different materials or calibration light sources for the experiment. One can perform the spectrometer experiment by placing the scintillator in the wheel, to be hit by the electron beam, and measuring the light outside the chamber. The central part of the platform consists of 15 movable aluminum blocks. The size of each block is  $10\text{ cm} \times 10\text{ cm} \times 2.9\text{ cm}$ . Finally, the right chamber is for measuring the lateral profile. Electron beams enter into the left chamber and produce showers in the aluminum blocks. The resulting secondary charge particles travel through the right chamber and hit the scintillator screen. The light reflected from the scintillator is subsequently detected. A CCD camera takes the image to record the electron density.

## 6.2 The Measurement of Shower Lateral Profile with Scintillator

In this section, a scintillator (AF995r ;  $\text{Al}_2\text{O}_3 : \text{Cr}^{3+}$ ) is placed behind the targets, converting the secondary shower particles into light. The light from the central region of the shower is recorded by a CCD camera. The CCD system is successfully implemented in the FLASH thick target run as just mentioned.

The scintillator (AF995r ;  $\text{Al}_2\text{O}_3 : \text{Cr}^{3+}$ ) is widely used for monitoring the charged particle beam. It is a material with high damage threshold, and high photon yield. Ref. [56] shows a spectrum of fluorescence photons with only one decay time 3.4 ms listed. To accurately reconstruct the shower lateral profile from the scintillation light, we first measure the wavelength and decay time of the scintillator spectrum. Since the electron beam is injected from booster ring with a 10 Hz frequency, it is necessary to measure the decay time of the scintillation light in order to access the influence of scintillation light from a certain event to the signal of subsequent events. Fig. 6.2 shows a decay time measurement using a photo-diode and digital multi-meter. Photons produced by scintillator (AF995r ;  $\text{Al}_2\text{O}_3 : \text{Cr}^{3+}$ ) are detected by a photo-diode. Their signals show a rise in the first few ms, believed to be the electronic response time. It is then followed by several exponential decays. At least three distinct decay patterns are observed. The first one has a decay time of 3.4 ms, the second one has a decay time of 6.7 ms and the third one has a decay time longer than 15 minutes. Fig. 6.3 shows the fluorescence spectrum of the scintillator. The spectrum show two close peaks located at wavelengths 694.0 nm and 692.8 nm respectively.

The measurements of  $\text{Al}_2\text{O}_3 : \text{Cr}^{3+}$  fluorescence spectrum and the corresponding decay times are performed with a narrow band filter allowing radiations of the wavelength range ( $694.3 \pm 5$  nm). Such a band width is however still too large to isolate each peak in the spectrum and study its individual decay properties. A representative image taken by the CCD camera at 2.3 radiation length is shown in Fig. 6.4. The  $X$  and  $Y$  axes denote the pixel numbers of the camera and the  $Z$  axis denotes the CCD count. One can integrate the counts spread over the  $X - Y$  plane for each radiation length and obtain the shower longitudinal profile as shown in Fig. 6.5. The shower maximum is seen to occur in between 2.3 to 2.6 radiation lengths.

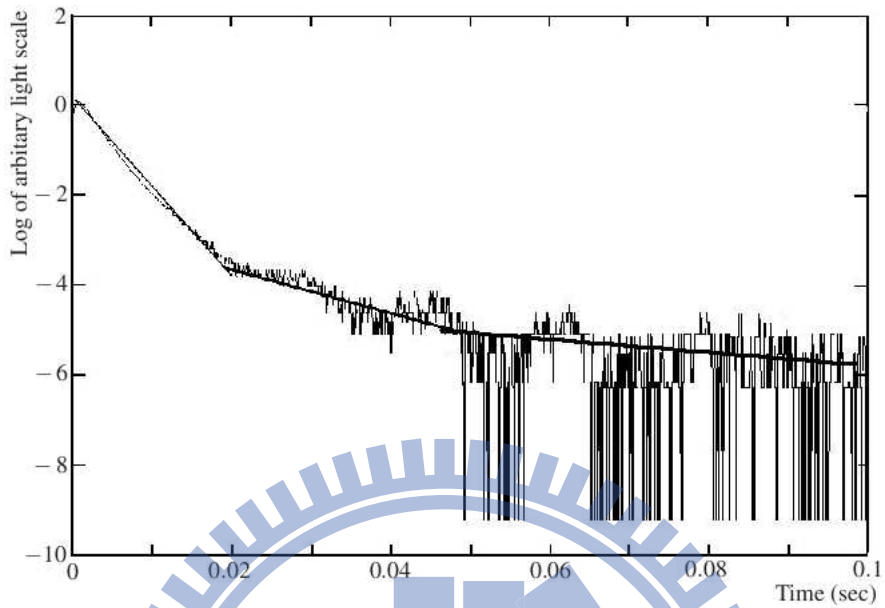


Figure 6.2: Results from the decay-time measurement. This decay-time of the scintillation light from scintillator is measured by photo-diode and digital multi-meter. The first decay pattern has a short decay time about 3.4 ms, the second one has a longer decay time about 6.7 ms and the third one has a decay time longer than 15 minutes.

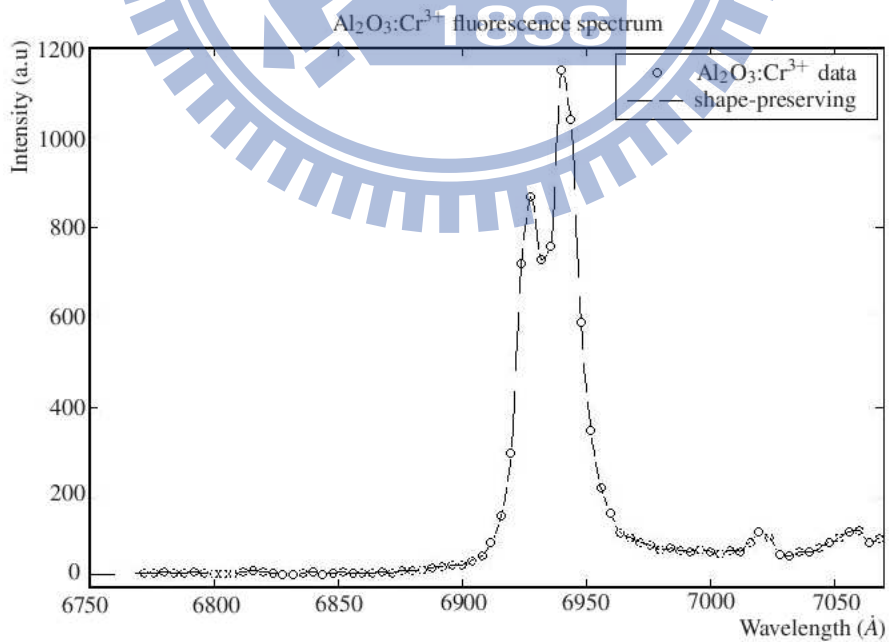


Figure 6.3: The fluorescence spectrum of AF995r scintillator ( $\text{Al}_2\text{O}_3:\text{Cr}^{3+}$ ). Two close peaks located at wavelengths 692.8 nm and 694.0 nm are clearly seen.

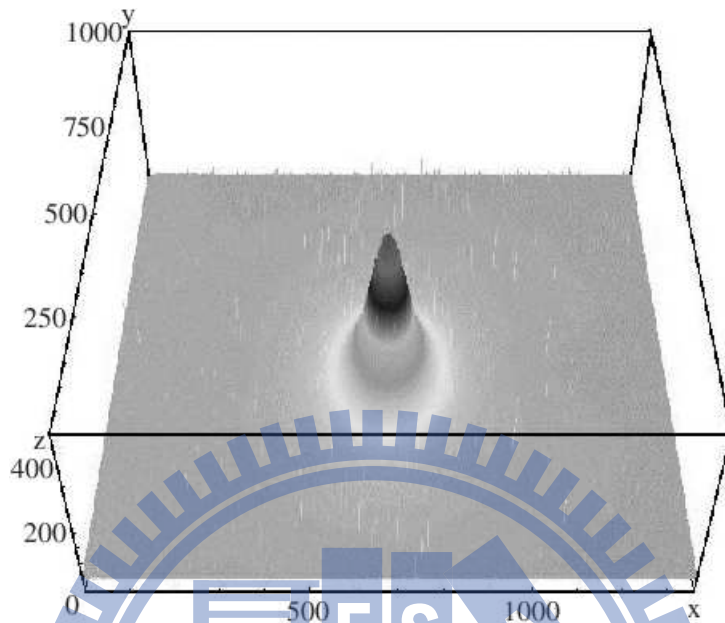


Figure 6.4: The shower image recorded by the CCD camera at 2.5 radiation length. The x and y axes labels the pixels number of CCD chip. The z axis is the count of photos record by CCD camera.

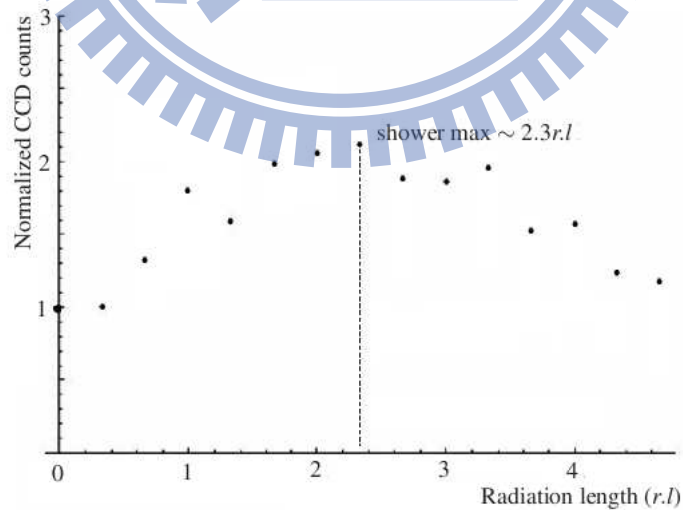


Figure 6.5: The shower longitudinal profile record by the CCD camera. The CCD camera integrates the fluorescence photons spread over the  $X - Y$  plane for each radiation length and obtain the shower longitudinal profile.



### 6.3 The Measurement of Cherenkov Radiations from Showers

The Cherenkov radiation is an important background to the fluorescence light measurement. The Cherenkov radiation from each individual charge particle is well known. Hence the uncertainty on the Cherenkov radiation in an air shower is due to the uncertainty in energy distributions of shower particles.

It is instructive to see from Fig. 6.6 that an electron with energy less than 100 MeV emits appreciable less numbers of Cherenkov photons than the saturated value.

For calculating Cherenkov radiation in air showers, the parameterization by Hillas [57] for electron energy distributions at a fixed shower age has been widely used. Such an energy distribution is obtained from air showers induced by a 100 GeV photon. However, a recent study using CORSIKA [43] and QGSJET01 [58] simulations gives a different parameterization for electron energy distributions and subsequently the resulting Cherenkov radiations [59]. The electron energy distributions in terms of the shower age are found to be universal, *i.e.*, independent of the type and energy of the primary particle. This new electron energy distribution could result into a Cherenkov radiation deviating from that given by Hillas' parameterization by as much as 20% depending on the viewing angle to the shower axis [60]. Since the accuracy of fluorescence measurement depends on a correct subtraction of Cherenkov contamination, it is important to directly measure such a contribution.

We are investigating the possibility of measuring Cherenkov radiation from air showers using the NSRRC 1.5 GeV electron beam. Geant4 [61] simulations of charge particle longitudinal profile and Cherenkov photon yield are presented in Fig. 6.8, where we have set the charge particle energy threshold at 1 MeV.

At the zero radiation length, the energy of each charge particle is 1.5 GeV. Since this energy is well beyond the 22 MeV threshold, the number of Cherenkov photons emitted by each charge particle already reaches the maximum value. We then choose to normalize two curves (longitudinal profile and Cherenkov photon yield at zero radiation length). The two curves begin to deviate for higher radiation lengths. At the shower maximum, *i.e.*, 2.3 radiation length, the Cherenkov photon yield drops to 60% of the maximum value. This is due to the increase of low energy charge particle which either can not produce Cherenkov photon or produces appreciable less number of

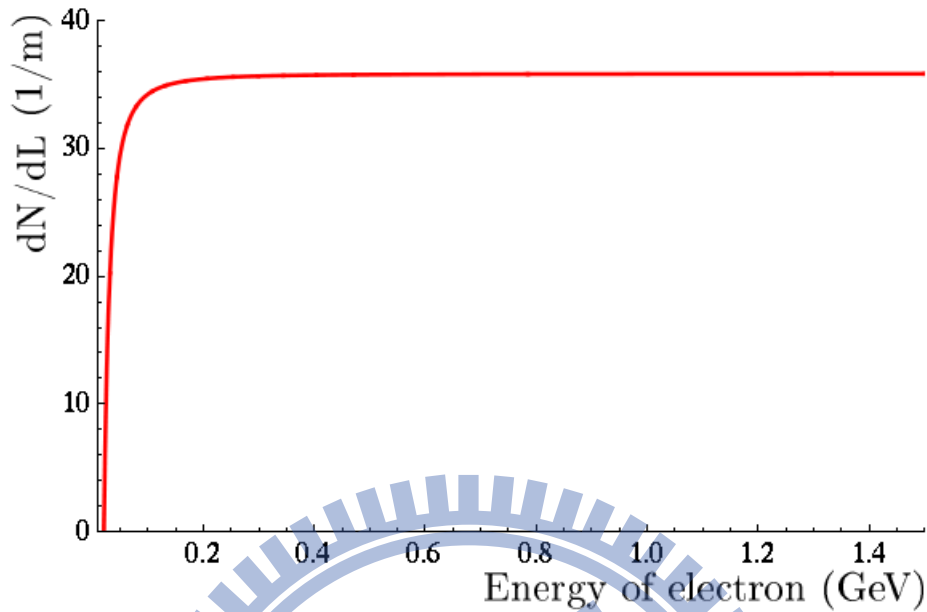


Figure 6.6: The number of photons emitted from an electron with in the wavelength between 380 nm to 780 nm. The threshold energy is about 21 MeV with refractive index of air is 1.00029. The photons numbers saturate close to 35 photons per meter above 100 MeV.

Cherenkov photons than the maximum value. It is clear that different electron energy distributions are reflected in the different Cherenkov photon yield.

In conclusion, we have outlined the laboratory astrophysics program in Taiwan. Besides the works in FLASH collaboration, we have explored the possibility of studying shower lateral and longitudinal profiles simultaneously using scintillator screen and CCD camera with NSRRC 1.5 GeV electron beam. We have found that it is necessary to isolate each spectrum peak of  $\text{Al}_2\text{O}_3:\text{Cr}$  scintillator screen so that the slowest-decay component of fluorescence spectrum can be identified. With a suitable filter, this slowest-decay component may be removed.

## 6.4 Geant4 Simulation

Geant4 is powerful simulation tools in several fields, such as high energy physics, medicine, space and radiation field. We using Geant4 to simulate the generation of secondary particles from 1.5 GeV electrons and the Cherenkov photon yield when the secondary charged particles through the air in this experiment. We are investigating the possibility of measuring Cherenkov radiation from air showers using the NSRRC 1.5 GeV electron beam. Geant4 simulations of charged particle

operating environment	operating system	Scientific Linux 4.2.1.6
	Geant4 version	4.8.0.p01
	libCLHEP version	1.9.2.2
simulation parameters	temperature of air	303 K
	refractive index of air	1.00029
	Atmospheric pressure	1013.25 kPa
	incident particle	1.5 GeV electrons
	radiator material	Aluminium

Table 6.1: The setting of Geant4 operating environment and simulation parameters.

longitudinal profile and Cherenkov photon yield are presented in Fig. 6.8, where we have set the charge particle energy threshold at 1 MeV. Table 6.1 lists the setting of Geant4 operating environment and simulation parameters. At the zero radiation length, the energy of each charge particle is 1.5 GeV. Since this energy is well beyond the 22 MeV threshold, the number of Cherenkov photons emitted by each charge particle already reaches the maximum value. We then choose to normalize two curves (longitudinal profile and Cherenkov photon yield) at zero radiation length. The two curves begin to deviate for higher radiation lengths. At the shower maximum, *i.e.*, 2.3 radiation length, the Cherenkov photon yield drops to 60% of the maximum value. This is due to the increase of low energy charge particle which either can not produce Cherenkov photon or produces appreciable less number of Cherenkov photons than the maximum value. It is clear that different electron energy distributions are reflected in the different Cherenkov photon yield.

We also compare the experimental data and simulation result in Fig. 6.8, where two curves are normalized by the sub area. Both of curves show the shower maximum approximate to 2.3 radiation length.

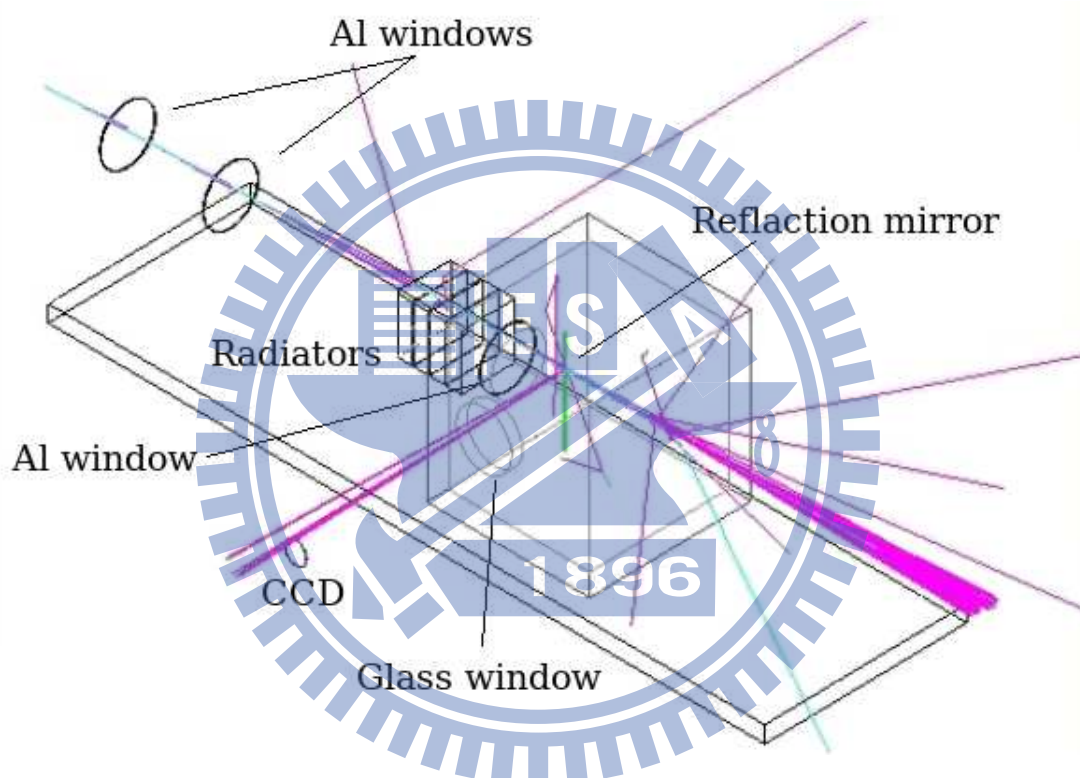


Figure 6.7: The platform structure setting of Geant4 simulation. The blue lines indicate the track of electrons, pink lines are emitted photons by charge. The incident electron beam hit the 2 mm thick aluminium window first, then lose the energy within aluminium radiators. The electrons emit the Cherenkov photons while electron pass the air, but the CCD record the photons only after electrons pass the third aluminium window.

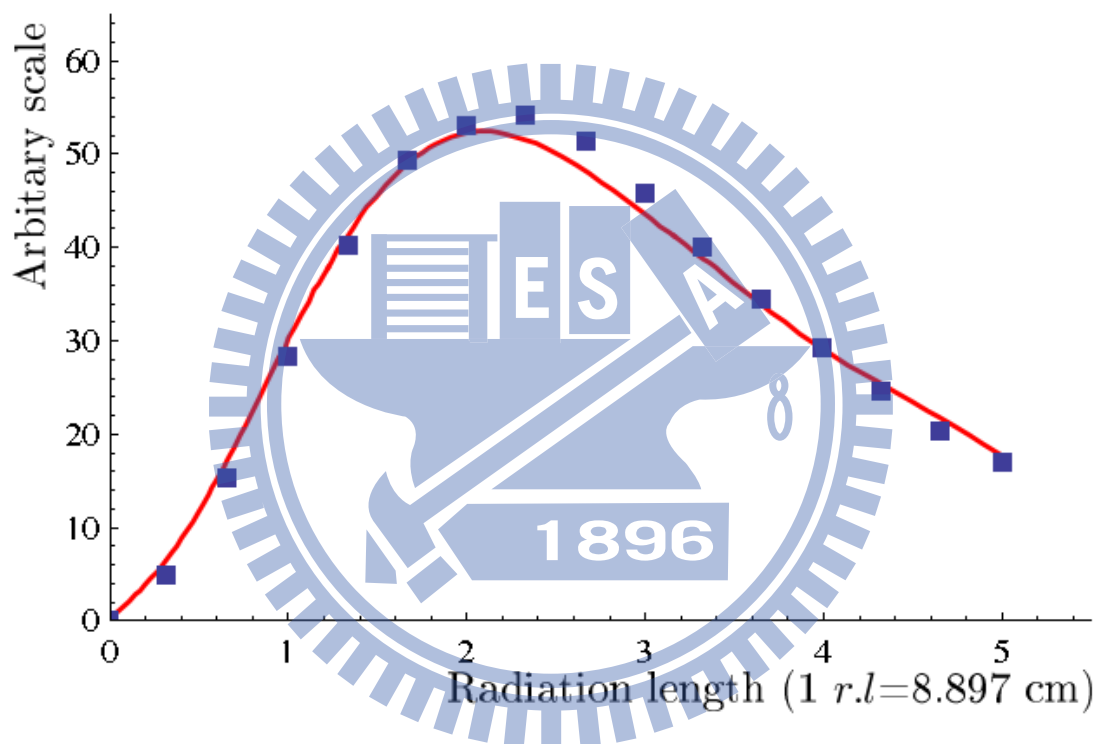


Figure 6.8: The longitudinal profiles of experimental data and Geant4 simulation result. The blue squares are experiment data, which record the Cherenkov photons by CCD. The red line is the result of Geant4 simulation. Both data and simulation result show the shower maximum are close to 2.3  $r.l.$ .

## Chapter 7

### Conclusions

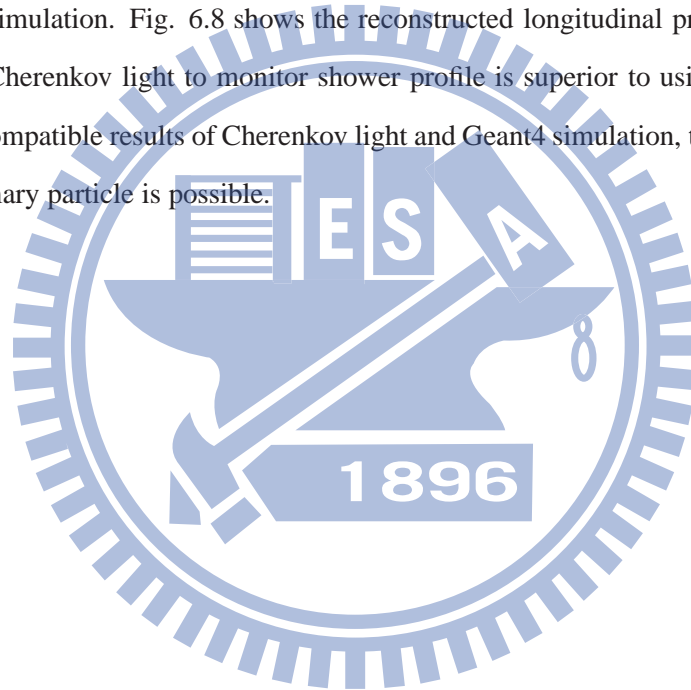
In Chapter 2, we reconstruct the possible flavor ratio at the astrophysical source by measuring the flavor ratio on the Earth. We choose parameter set 1 in Table 2.4 for analysis. The pion source can be separated from muon-damped source below 33.3 PeV at  $\Delta R^I/R^I = 4\%$  and  $\Delta S^I/S^I$  related to the former by the Poisson statistics, E.q. (2.17). The muon-damped source can be separated from pion source below 33.3 PeV at  $\Delta R^I/R^I = 11\%$  and  $\Delta S^I/S^I$  related to the former by the Poisson statistics. This result implies that the reconstruction of neutrino flavor ratios at the source require abundant number of events. If we consider higher energy neutrinos ( $E_\nu \geq 33.3$  PeV) in our analysis and choose parameters as Table 2.5, we find the new parameter  $R^{\text{II}}$  is more efficient than  $R^{\text{I}}$  to reconstruct the neutrino flavor ratio at the source, given the same event number. The  $\nu_\mu - \nu_\tau$  symmetry implies the  $S^{\text{II}}$  is close to 1. Hence  $S^{\text{II}}$  is not useful for improving the flavor measurement.

In Chapter 3, we compute the possibly observable flavor ratio on the Earth via the neutrino oscillation and neutrino decays. Only the type-III decay mechanism in the Table.3.1 can be totally separated from the oscillation mechanism. The other six decay mechanisms produce overlapped regions of neutrino flavor ratios.

In Chapter 4 and 5, we build a Monte-Carlo program to simulate neutrino interactions with the Earth. The program estimates the fluxes of muon and tau inside the detector sensitive region. We use CORSIKA to simulate the tau shower with different energies and calculate the electric field of synchrotron radiations. Fig. 5.13 shows the reconstructed pulse is proportional to shower energy.

Fig. 5.14 and Fig. 5.15 indicate that hadronic showers(pion and kaon shower) at the same energy produce the same pulse. Based on this result, we can estimate the energy of the original neutrino by the measured pulses of synchrotron radiations.

In Chapter 6, we design a laboratory experiment to measure the development of shower and compare the data with GEANT4 simulation. Since the decay time of scintillator is longer than the injected period of electron beam, the CCD measures the integrated signal of several bunches. Fig. 6.5 shows the reconstructed longitudinal profile by fluorescence light emitted from the scintillator. The result is not satisfactory. However, the result of Cherenkov light is compatible with the result of Geant4 simulation. Fig. 6.8 shows the reconstructed longitudinal profile by Cherenkov light. Using the Cherenkov light to monitor shower profile is superior to using the fluorescence light. Given the compatible results of Cherenkov light and Geant4 simulation, tracking the original energy of the primary particle is possible.



## Appendix A

# Differential cross section of lepton energy loss

### A.1 Pair production

$$\phi_e = [((2 + \rho^2)(1 + \beta) + \xi(3 + \rho^2)) \ln(1 + \frac{1}{\xi}) + \frac{1 - \rho^2 - \beta^2}{1 + \xi} - (3 + \rho^2)] L_e$$

$$\phi_l = [((1 + \rho^2)(1 + \frac{3}{2}\beta) - \frac{1}{\xi}(1 + 2\beta)(1 - \rho^2)) \ln(1 + \frac{1}{\xi}) + \frac{\xi(1 - \rho^2 - \beta^2)}{1 + \xi} + (1 + 2\beta)(1 - \rho^2)] L_l$$

$$L_e = \ln \frac{189Z^{-\frac{1}{3}} \sqrt{(1 + \xi)(1 + Y_e)} E_y (1 - \rho^2)}{E_y (1 - \rho^2) + 2m_e \sqrt{e} R Z^{-\frac{1}{3}} (1 + \xi)(1 + Y_e)} - \frac{1}{2} \ln [1 + (\frac{3m_e}{2m_l} Z^{-\frac{1}{3}})^2 (1 + \xi)(1 + Y_e)]$$

$$L_l = \ln \frac{378m_l Z^{-\frac{2}{3}} (1 - \rho^2)}{3m_e (E_y (1 - \rho^2) + 2m_e \sqrt{e} R Z^{-\frac{1}{3}} (1 + \xi)(1 + Y_e))}$$

$$Y_e = \frac{5 - \rho^2 + 4\beta(1 + \rho^2)}{2(1 + 3\beta) \ln(3 + \frac{1}{\xi}) - \rho^2 - 2\beta(2 - \rho^2)}$$



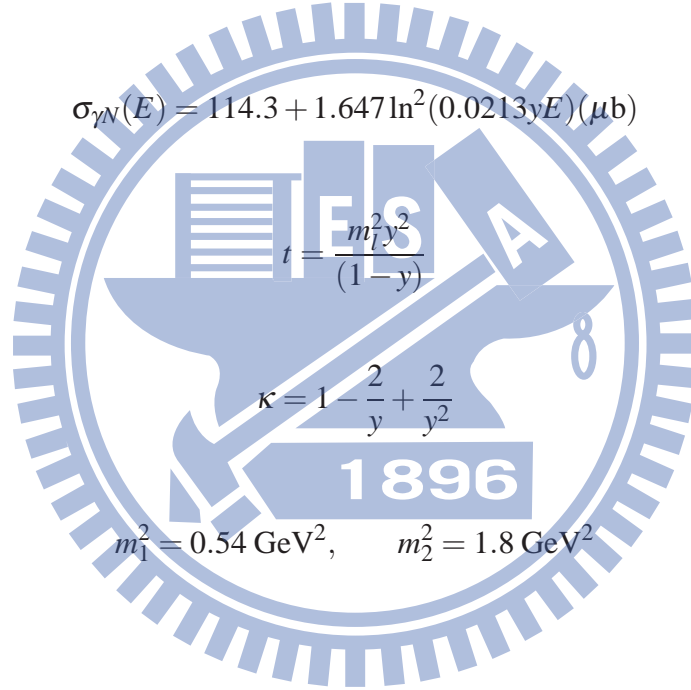
$$Y_l = \frac{4 + \rho^2 + 3\beta(1 + \rho^2)}{(1 + \rho^2)(\frac{3}{2} + 2\beta) \ln(3 + \xi) + 1 - \frac{3}{2}\rho^2}$$

$$\beta = \frac{y^2}{2(1-y)}, \quad \xi = \left(\frac{m_l y}{2m_e}\right)^2 \frac{(1-\rho^2)}{1-y}.$$

## A.2 Photonuclear

$$G(x) = \frac{3}{x^3} \left( \frac{x^2}{2} - 1 + e^{-x}(1+x) \right), \quad x = 0.00282A^{\frac{1}{3}} \sigma_{\gamma N}$$

$$\sigma_{\gamma N}(E) = 114.3 + 1.647 \ln^2(0.0213yE) (\mu\text{b})$$



## Appendix B

### Mont-Carlo method

SHINIE considers neutrino nucleon interaction , energy loss and decays of leptons in the Earth. In this section, we try to establish the link between interaction probability and differential cross section. The total cross section,  $\sigma$ , can be calculated by integrating the differential cross section:

$$\sigma = \int_{y_{min}}^{y_{max}} \frac{d\sigma}{dy} dy. \quad (B.1)$$

The total cross section can be normalized by divided itself. If we change the upper limit of integrating, the range of the formula should be

$$0 < \frac{\int_{y_{min}}^y \frac{d\sigma}{dy} dy}{\sigma} < 1, \quad (B.2)$$

with 0 for  $y = y_{min}$  and 1 for  $y = y_{max}$ . This range can map to the random number  $r \in [0, 1]$ .

Hence the relation between random number and differential cross section is

$$\int_0^r dr = \frac{\int_{y_{min}}^y \frac{d\sigma}{dy} dy}{\sigma}. \quad (B.3)$$

Combining the normalized condition of probabilities,  $\int dP = 1$ , to Eq. (B.3). The relationship between probability and differential cross section is

$$\int_{y_{min}}^y \frac{dP}{dy} dy = \frac{\int_{y_{min}}^y \frac{d\sigma}{dy} dy}{\sigma} = \int_0^r dr, \quad (B.4)$$

and leads to  $\frac{dp}{dy}dy = \frac{d\sigma}{\sigma dy}dy = dr$ . The expectation value of  $y$  defined by

$$\langle y \rangle = \int_{y_{min}}^{y_{max}} y \frac{dP}{dy} dy = \int_{y_{min}}^{y_{max}} \frac{y d\sigma}{\sigma dy} dy. \quad (B.5)$$

In Monte-Carlo method, any value of random number can map to a corresponding  $y_i$ . If we generate the value by  $N$  times. We get the average of  $y_i$  and express as

$$\langle y \rangle = \sum_{i=1}^N \frac{y_i}{N}. \quad (B.6)$$

Applying this result to Eq. (4.2), we have

$$\beta_i(E) = \frac{N}{A} \int_{y_{min}}^{y_{max}} y \frac{d\sigma^i(y, E)}{dy} dy = \frac{N}{A} \int_{y_{min}}^{y_{max}} \frac{\sigma^i y d\sigma^i(y, E)}{\sigma^i dy} dy = \frac{N\sigma^i}{A} \langle y \rangle. \quad (B.7)$$

and

$$-dE = \beta_i(E)EdX = \frac{N\sigma^i}{A}EdX \langle y \rangle \quad (B.8)$$

# Bibliography

- [1] A. Neronov, D. Semikoz, F. Aharonian and O. Kalashev, Phys. Rev. Lett. **89**, 051101 (2002) . [arXiv:astro-ph/0201410]; O. E. Kalashev, V. A. Kuzmin, D. V. Semikoz and G. Sigl, Phys. Rev. D **66**, 063004 (2002) . [arXiv:hep-ph/0205050].
- [2] M. Kachelrieß, S. Ostapchenko and R. Tomás, Phys. Rev. D **77**, 023007 (2008) .
- [3] J. P. Rachen and P. Mészáros, Phys. Rev. D **58**, 123005 (1998) .
- [4] K. Greisen, Phys. Rev. Lett. **16**, 758 (1966) .
- [5] G. T. Zatesepin and V. A. Kuzmin, JETP lett., **4**, 78 1966.
- [6] V. S. Berezinsky and G. T. Zatsepin, Phys. Lett. **28B**, 423 (1969) . R. Engel, D. Seckel and T. Stanev, Phys. Rev. D **64**, 093010 (2001) .
- [7] Z. Maki, M. Nakagawa and S. Sakata, Prog. Theor. Phys. **28**, 870 (1962) .
- [8] B. Pontecorvo, Zh. Eksp. Teor. Fiz. **53** 1717 (1967).
- [9] <http://icecube.wisc.edu/>
- [10] J. G. Learned and S. Pakvasa, Astropart. Phys. **3**, 267 (1995) .
- [11] <http://www.KM3NeT.org/>
- [12] J. F. Beacom *et al.*, Phys. Rev. D **68**, 093005 (2003) ; [Erratum-ibid. D **72**, 019901 (2005)].
- [13] P. D. Serpico and M. Kachelrieß, Phys. Rev. Lett. **94**, 211102 (2005) .
- [14] W. Winter, Phys. Rev. D **74**, 033015 (2006) .

- [15] K. C. Lai, Guey Lin Lin, and T. C. Liu, *Phys. Rev. D* **80**, 103005 (2009) .
- [16] E. Bugaev *et al.*, *Astropart. Phys.* **21**, 491-509 (2004) .
- [17] K. Blum, Y. Nir and E. Waxman, arXiv:0706.2070 [hep-ph].
- [18] J. F. Beacom, P. Crotty and E. W. Kolb, *Phys. Rev. D* **66**, 021302 (2002) .
- [19] H. Athar, G. Parente and E. Zas, *Phys. Rev. D* **62**, 093010 (2000) .
- [20] F. Halzen and D. Saltzberg, *Phys. Rev. Lett.* **81**, 4305 (1998) .
- [21] S. Choubey, V. Niro and W. Rodejohann, *Phys. Rev. D* **77**, 113006 (2008) .
- [22] O. Mena, I. Mocioiu and S. Razzaque, *Phys. Rev. D* **75**, 063003 (2007) .
- [23] M. Maltoni, T. Schwetz, M. Tortola and J. W. F. Valle, *New J. Phys.* **6**, 122 (2004) .
- [24] P. F. Harrison, D. H. Perkins and W. G. Scott, *Phys. Lett. B* **530**, 167 (2002); *Phys. Lett. B* **535**, 163 (2002); Z. Z. Xing, *Phys. Lett. B* **533**, 85 (2002); X. G. He and A. Zee, *Phys. Lett. B* **560**, 87 (2003); see also L. Wolfenstein, *Phys. Rev. D* **18**, 958 (1978); Y. Yamanaka, H. Sugawara and S. Pakvasa, *Phys. Rev. D* **25**, 1895 (1982) [Erratum-*ibid.* *D* **29**, 2135 (1984)].
- [25] A. B. Balantekin and G. M. Fuller *et al.*, *Phys. Lett. B* **471**, 195 (1999) . [arXiv:hep-ph/9908465].
- [26] P. F. Harrison and W. G. Scott, *Phys. Lett. B* **547**, 219 (2002) .
- [27] M. Maltoni and W. Winter, *JHEP.* **64**, 0807 (2008) .
- [28] J. G. Learned, and K. Mannheim, *Ann. Rev. Nucl. Part. Sci.*, **50**, 679, (2000).
- [29] J. J. Tseng *et al.*, *Phys. Rev. D* **68**, 063003 (2003) .
- [30] A. Neronov, D. Semikoz, F. Aharonian and O. Kalashev, *Phys. Rev. Lett.* **89**, 051101 (2002)
- [31] R. Engel, D. Seckel and T. Stanev, *Phys. Rev. D* **64**, 0093010 (2001) .

- [32] R. U. Abbasi *et al.*, Phys. Rev. Lett. **92**, 151101 (2004) .
- [33] G. W. Hou and M.A. Huang, Proc. of the 1st NCTS Workshop on Astroparticle Physics, Eds. H. Athar, G. -L. Lin and K. -W. Ng, World Scientific, Singapore, 105-116, (2002); astro-ph/0204145 .
- [34] M. A. Huang, Proc. of 20th International Conference on Neutrino Physics and Astrophysics ( $\nu$ -2002) at Munich, Nucl. Phys. B (Proc. Suppl.) 118, 516, (2003).
- [35] Z. Cao, M.A. Huang, P. Sokolsky, Y. Hu, J. Phys. G **31**, 571 (2005) .
- [36] M. A. Huang, J. J. Tseng, and G. L. Lin, Proc. of the 28th ICRC, Tsukuba, Japan, p.1427, (2003).
- [37] M. Z. Wang for NuTel collaboration, Proc. of the 28th ICRC, Tsukuba, Japan, p.1525, (2003).
- [38] P. Yeh *et al.*, Proc. of CosPA 2003, Modern Physics Lett. A.19, 1117-1124, (2004).
- [39] R. Gandhi *et al.*, Phys. Rev. D **58**, 093009 (1999) .
- [40] J. Pumplin, D. R. Stump, J. Huston, H. L. Lai, P. Nadolsky and W. K. Tung, JHEP 0207, 012 (2002).
- [41] G. Domokos and S. Kovesi-Domokos, hep-ph/9801362 and hep-ph/9805221.
- [42] D. Fargion, Astrophys. J. **570**, 909(2002).
- [43] D. Heck, J. Knapp, J. N. Capdevielle, G. Schatz and T. Thouw, FZKA Report 6019, Forschungszentrum Karlsruhe, (1998).
- [44] H. R. Allan, Prog. in Element. Part. and Cos. Ray Phys. **10**, 171(1971).
- [45] T. Huege and H. Falcke, Astron. Astrophys. **412**, 19 (2003).
- [46] K. Kamata, J. Nishimura, Suppl. Prog. Theo. Phys. **4**, 93 (1957).
- [47] K. Greissen, Phys. Rev. Lett. **16**, 748 (1966) .

- [48] J. D. Jackson, Classical Electrodynamics, 3rd edn, **673** (1998).
- [49] T. C. Liu *et al.*, Proc., 29th International Cosmic Ray Conf., Pune, India, Aug. 3-10, (2005).
- [50] J. Belz *et al.*, Astropart. Phys. **25**, 57 (2006) ; R. Abbasi *et al.*, Astropart. Phys. **29**, 77 (2008) .
- [51] G. R. Hwang and S. Kim, Phys. Rev. D **78**, 093008 (2008) .
- [52] D. Saltzberg, P. Gorham, D. Walz *et al.*, Phys. Rev. Lett., 86, 2802, (2001).
- [53] M. A. Huang, Proc. of the 21th International Conference on Neutrino Physics and Astrophysics (v-2004) at Paris, French, Nucl. Phys. B (Proc. Suppl.), 143, 546, (2005); astro-ph/0412642.
- [54] S. I. Dutta, M.H. Reno, I. Sarcevic and D. Seckel, Phys. Rev. D **63**, 094020 (2001) .
- [55] S. I. Dutta, Y. Huang, M.H. Reno, Phys. Rev. D **72**, 013005 (2005) .
- [56] K. J. McCarthy *et al.*, J. Appl. Phys. **92**, 6541 (2002) .
- [57] A. M. Hillas, J. Phys. G **8**, 1461 (1982) .
- [58] N. N. Kalmykov, S. S. Ostapchenko, A. I. Pavlov, Nucl. Phys. B (Proc. Suppl.) **52**, 17 (1997) .
- [59] F. Nerling *et al.*, Astropart. Phys. **24**, 321 (2006) .
- [60] F. Nerling *et al.*, astro-ph/0507251.
- [61] S. Agostinelli *et al.*, Nucl. Instr. and Meth. A **506**, 250 (2003) .
- [62] T. C. Liu *et al.*, Proc., 29th International Cosmic Ray Conf., Pune, India, Aug. 3-10, (2005).
- [63] J. Belz *et al.*, Astropart. Phys. **25**, 57 (2006) ; R. Abbasi *et al.*, Astropart. Phys. **29**, 77 (2008) .
- [64] E. Waxman and J. N. Bahcall, Phys. Rev. Lett. **78**, 2292 (1997) . [arXiv:astro-ph/9701231]; *ibid.*, Phys. Rev. D **59**, 023002 (1999) . [arXiv:hep-ph/9807282].

- [65] B. Rossi, High-Energy Particles, Prentice Hall Series, 1965.
- [66] R. M. Sternheimer *et al.*, At. Data Nucl. Data Tables 30, 261 (1984).
- [67] A. A. Petrukhin and V. V. Shestakov, Can. J. Phys. 46, S377 (1968).
- [68] R. P. Kokoulin and A. A. Petrukhin, Proc., 12th International Cosmic Ray Conf. Tasmania, Australia, Vol 6 (1971).
- [69] L. B. Bezrukov and E. V. Bugaev, Sov. J. Nucl. Phys. 33, 635 (1981).
- [70] J. L. Liu *et al.*, J. Phys. G **36**, 075201 (2009) .
- [71] C. H. Iong, “A monte-carlo study on earth-skimming tau neutrinos”, thesis (M.A.), National Chiao-Tung University (2004).
- [72] Y. L. Hung, “Simulation of shower arising from high energy neutrinos”, thesis (M.A.), National Chiao-Tung University (2006).

